LOCAL STRUCTURES OF THE AL–RE MARGINAL METALLIC GLASSES AND LIQUIDS: A MOLECULAR DYNAMICS STUDY

A THESIS SUBMITTED TO
THE GRADUATE SCHOOL OF NATURAL AND APPLIED SCIENCES
OF
MIDDLE EAST TECHNICAL UNIVERSITY

BY

DOĞUHAN SARITÜRK

IN PARTIAL FULFILLMENT OF THE REQUIREMENTS
FOR
THE DEGREE OF MASTER OF SCIENCE
IN
METALLURGICAL AND MATERIALS ENGINEERING

JULY 2022

Approval of the thesis:

LOCAL STRUCTURES OF THE AL – RE MARGINAL METALLIC GLASSES AND LIQUIDS: A MOLECULAR DYNAMICS STUDY

submitted by **DOĞUHAN SARITÜRK** in partial fulfillment of the requirements for the degree of **Master of Science in Metallurgical and Materials Engineering Department, Middle East Technical University** by,

Prof. Dr. Halil Kalıpçılar
Dean, Graduate School of **Natural and Applied Sciences** _____

Prof. Dr. C. Hakan Gür
Head of Department, **Metallurgical and Materials Engineering** _____

Prof. Dr. Y. Eren Kalay
Supervisor, **Metallurgical and Materials Engineering, METU** _____

Examining Committee Members:

Prof. Dr. Benat Koçkar
Mechanical Engineering, Hacettepe University _____

Prof. Dr. Y. Eren Kalay
Metallurgical and Materials Engineering, METU _____

Assoc. Prof. Dr. Caner Şimşir
Metallurgical and Materials Engineering, METU _____

Assoc. Prof. Dr. Sezer Özerinç
Mechanical Engineering, METU _____

Assist. Prof. Dr. Eda Aydoğan Güngör
Metallurgical and Materials Engineering, METU _____

Date: 07.07.2022

I hereby declare that all information in this document has been obtained and presented in accordance with academic rules and ethical conduct. I also declare that, as required by these rules and conduct, I have fully cited and referenced all material and results that are not original to this work.

Name, Surname: Doğuhan Sarıtürk

Signature :

ABSTRACT

LOCAL STRUCTURES OF THE AL – RE MARGINAL METALLIC GLASSES AND LIQUIDS: A MOLECULAR DYNAMICS STUDY

Sarıtürk, Doğuhan
M.S., Department of Metallurgical and Materials Engineering
Supervisor: Prof. Dr. Y. Eren Kalay

July 2022, 89 pages

Al-based metallic glasses (MGs) have outstanding structural and functional properties and are of great interest in the literature and industry. The formation of metallic glasses opens up extraordinary possibilities, and the structure and structure-property relationship at the atomic level must be thoroughly studied to tailor such properties. Al-Rare Earth (RE)-based alloys form an important class of marginal glass-forming alloys in which the presence of Al nanocrystals accompanies primary crystallization. Our previous studies on Al-based rare earth (Al–RE) metal alloys (RE: Sm, Tb) have shown that the phase selection hierarchy upon devitrification depends on the middle range order present in the devitrification state. In this study, the atomic structures of binary Al-Sm metal alloys were investigated using molecular dynamics (MD) simulations with Embedded Atom Method (EAM) potential to reveal the structural evolution in molten, supercooled, and quenched states considering short and medium range orders.

Keywords: Metallic glasses, aluminum alloys, molecular dynamics, short-range order, medium-range order

ÖZ

AL-NTE MARJİNAL METALİK CAMLARIN VE SIVILARIN LOKAL YAPILARI: MOLEKÜLER DİNAMİK ÇALIŞMASI

Sarıtürk, Doğuhan
Yüksek Lisans, Metalurji ve Malzeme Mühendisliği Bölümü
Tez Yöneticisi: Prof. Dr. Y. Eren Kalay

Temmuz 2022 , 89 sayfa

Al bazlı metalik camlar (MG'ler) olağanüstü yapısal ve işlevsel özelliklere sahiptir ve hem literatürde hem de endüstride büyük ilgi görmektedir. Metalik camların oluşumu olağanüstü olanaklara yol açar ve bu tür özellikleri uyarlamak için atomik düzeyde yapı ve yapı-özellik ilişkisi iyice incelenmelidir. Al-Nadir Toprak (RE) bazlı alaşımlar, Al nanokristallerin varlığının birincil kristalleşmeye eşlik ettiği marjinal cam oluşturan alaşımların önemli bir sınıfını oluşturur. Al bazlı nadir toprak (Al – RE) metal alaşımları (RE: Sm, Tb) üzerine daha önceki çalışmalarımız, devitrifikasyon üzerine faz seçim hiyerarşisinin, devitrifikasyon durumda mevcut olan orta erim düzenine bağlı olduğunu göstermiştir. Bu çalışmada, ikili Al-Sm metal alaşımlarının atomik yapıları, kısa ve orta erim düzenleri dikkate alınarak erimiş, aşırı soğutulmuş ve su verilmiş hallerdeki yapısal evrimi ortaya çıkarmak için Gömülü Atom Yöntemi (EAM) potansiyeli ile moleküler dinamik (MD) simülasyonları kullanılarak araştırılmıştır.

Anahtar Kelimeler: Metalik camlar, alüminyum alaşımları, moleküler dinamik, kısa erim düzeni, orta erim düzeni

To My Precious Family...

ACKNOWLEDGMENTS

First and foremost, I would like to express my sincere gratitude to my advisor, Prof. Dr. Y. Eren Kalay, for his guidance, support, and contributions throughout my study. Without his mentorship and invaluable assistance, this thesis would not have been possible.

I would like to thank Tolga Han Ulucan, who introduced me to the Metal Development Laboratory and was the architect of this study. The time we spent with him took this work much further, and I am sure our joint work will continue in the future. Can Okuyucu's contributions to this thesis, which made it possible for me to finish it as a result of our rigorous conversations and sleepless nights, cannot be described in words. His companionship will never be forgotten. I appreciate Emel Erdal for her contributions to the thesis process we spent at similar times. Our despair became the hope for each other to complete our work. I am so grateful to my current and former laboratory colleagues, Fatma Saadet Güven, Gökhan Polat, and Anıl Erdal, for providing me with the strength I needed to complete this study. Many thanks to undergraduate students of MDL Sabri Ufuk Arısan, Yunus Emre Doğan, and Zeynep Ege Uysal, whose support I greatly benefited from during our time together. I owe one to my dear friends Basri Çerçi, Çağlar Karaoğlu, Esra Kaderli, Hüseyin Engin Sever, Merve Nur Doğu, Mustafa Balcılar, Oğuz Gözcü, Özgün Umut Tukaç, Pelin Gündoğmuş, Seren Özer, Utkucan Kayacı, Yasemin Aşkar, and Yeşim Yalçın who made this challenging process bearable.

Endless thanks to my mother Aytülü, my father Kazım, and my brother Batuhan, who have always stood by me and supported me in all aspects of my life. I could not achieve any of my goals if I did not have such a wonderful family. Last but not least, I am eternally grateful to Helin Gümüş for always being there for me, for encouraging me to do my best, and for her understanding and patience. Thanks again, I couldn't have pulled this off without you.

This material is based upon work supported by the Air Force Office of Scientific Research under award number FA9550-20-1-0261. The numerical calculations reported in this study were partially performed at TUBITAK ULAKBIM, High Performance and Grid Computing Center (TRUBA resources).

Disclaimer

Any opinions, findings, and conclusions or recommendations expressed in this material are those of the author and do not necessarily reflect the views of the United States Air Force.

TABLE OF CONTENTS

LIST OF TABLES

LIST OF FIGURES

LIST OF ABBREVIATIONS

AIMD	*ab initio* Molecular Dynamics
APS	Advanced Photon Source
APT	Atom Probe Tomography
bcc	Body-Centered Cubic
BF-TEM	Bright-Field Transmission Electron Microscopy
BMG	Bulk Metallic Glass
BO	Born-Oppenheimer
BOD	Bond Angle Distribution
BOP	Bond Order Parameter
CN	Coordination Number
DFT	Density Functional Theory
DSC	Differential Scanning Calorimetry
EAM	Embedded Atom Method
EXAFS	Extended X-Ray Absoprtion Fine Structure
fcc	Face-Centered Cubic
FEM	Fluctuation Electron Microscopy
GFA	Glass-Forming Ability
GGA	Generalized Gradient Approximation
H-A	Honeycutt-Andersen
hcp	Hexagonal Close-Packed
HEXRD	High-Energy X-Ray Diffraction
HRTEM	High-Resolution Transmission Electron Microscopy
ICO	Icosahedron

JPL	Jet Propolsion Laboratory
L-J	Lennard-Jones
LAMMPS	Large-Scale Atomic/Molecular Massively Parallel Simulator
LDA	Local Density Approximation
LRO	Long-Range Order
MC	Monte Carlo
MD	Molecular Dynamics
MG	Metallic Glass
MRO	Medium-Range Order
MSD	Mean Square Displacement
MTDSC	Modulated-Temperature Differential Scanning Calorimetry
PDF	Pair Distribution Function
PPDF	Partial Pair Distribution Function
QMD	Quantum Molecular Dynamics
RE	Rare-Earth
RMC	Reverse Monte Carlo
ROI	Region-of-Interest
SAED	Selected Area Electron Diffraction
SRO	Short-Range Order
TM	Transition Metal
VFT	Vogel-Fulcher-Tammann
W-C	Warren-Cowley
XANES	X-Ray Absorption Edge Structure

CHAPTER 1

INTRODUCTION

Materials are conventionally categorized into three primary groups: metals, ceramics, and polymers. This category scheme is mainly based on the materials' atomic structure and bonding characteristics. Metallic materials are primarily composed of one or more metallic elements, sometimes accompanied by small amounts of nonmetallic elements. An alloy is a mixture of elements with at least one metal. Most metallic materials and their alloys have their atomic structures arranged in an orderly way over large atomic distances with periodicity and rotational and translational symmetry. Hence, long-range order (LRO) usually exists within metallic materials. The three-dimensional ordered structures observed in the atomistic scale in metallic materials form crystalline structures, and how the atoms situate themselves within crystalline materials results in the formation of crystal structures. There are three main types of crystal structures commonly seen in metallic materials: the face-centered cubic (*fcc*), the body-centered cubic (*bcc*), and the hexagonal close-packed (*hcp*). Metals and their alloys predominantly have metallic bonding in which the electrons within the materials do not bound to any specific atom and are free to wander around within the material. The unbound electrons of metallic materials, called valance electrons, form so-called a sea of electrons and are responsible for the non-directional bonding characteristics of the metals.

The atomic structures of some materials lack the long-range ordered structures found in crystalline materials. Those materials are called non-crystalline or amorphous. Although the long-range order in amorphous materials is absent, various short- to medium-range ordered structures might be present in the structures. Figure 1.1a shows a hypothetical atomic structure of a ternary alloy that possesses an ordered *fcc*

crystal structure, whereas Figure 1.1b is a disordered amorphous counterpart of the same alloy. Some polymeric materials, minerals, and inorganic glasses (e.g., SiO_2) exhibit non-crystalline atomic structures. Historically glasses are known to have random local structures. Thus, the term glassy has been used interchangeably with disordered and amorphous. In addition to the naturally occurring amorphous materials, amorphization can be achieved by several production methods. Continuously cooling from the liquid state, vapor deposition, and mechanical milling are just three options to utilize in obtaining disordered structures.

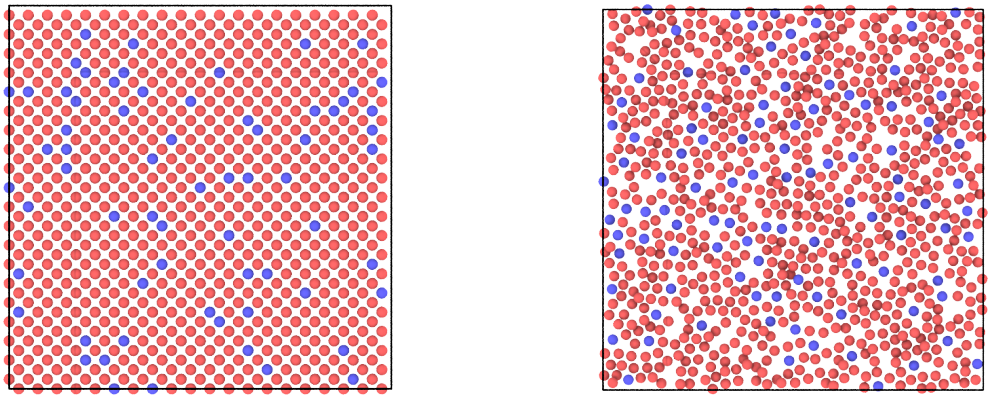

(a) (b)

Figure 1.1: A representative atomic structure of a hypothetical binary system in (a) an ordered *fcc* state, and (b) a disordered amorphous state.

1.1 Metallic Glasses

1.1.1 History of Metallic Glasses

The connection between the metals and amorphous structures was realized when Duwez et al. synthesized the first-ever metallic alloy appearing to be amorphous in September 1959 [1]. They used a modified splat quenching method called the *gun technique* and were able to obtain cooling rates as high as $10^6\,\mathrm{K\,s^{-1}}$. Gun technique was used to rapidly cool down an alloy with composition $Au_{75}Si_{25}$ from $\sim$1300 °C to room temperature, and the resulting $\sim 10\,\mu\mathrm{m}$ thick flake was characterized by using a Debye-Scherrer camera. The X-ray diffraction pattern they published, see Figure 1.2,

was absent from any crystalline peaks. However, the amorphous sample they obtained was quite unstable at room temperature and decomposed into non-equilibrium crystalline phases within 24 hours. No matter what, the pretty short paper by Duwez et al. pioneered the studies on metallic glasses (MG).

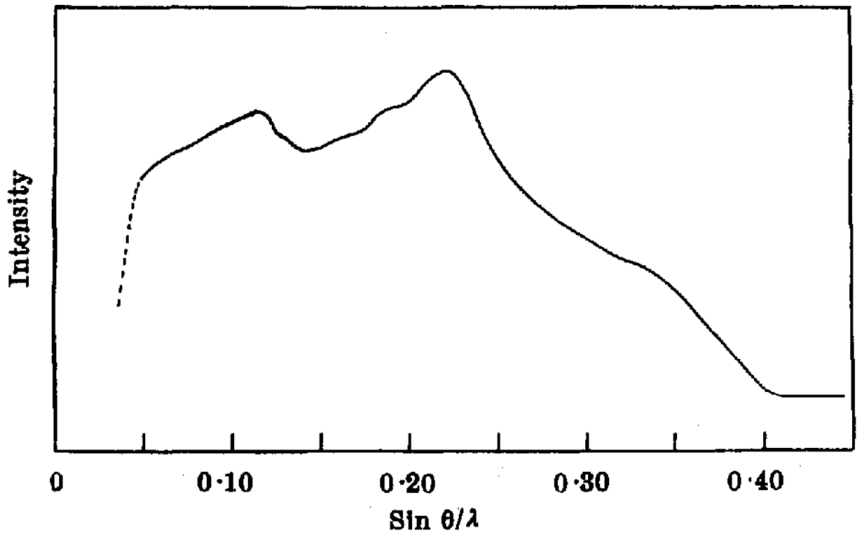

Figure 1.2: X-ray diffraction pattern of the first metallic glass, $\sim 10\,\mu\mathrm{m}$ $Au_{75}Si_{25}$ flake, with respect to $\sin\theta/\lambda$. Acquired via a Debye-Scherrer camera under Cu K radiation. Adapted from [1].

The instability and inability to carry out characterization studies on non-crystalline $Au_{75}Si_{25}$ alloy led Duwez et al. to synthesize binary Te$-$X (X = Ga, In, Ge) [2] alloys. The amorphous structure of the new alloys was stable up to $100\,^{\circ}\mathrm{C}$. The same group found a binary alloy showing greater stability three years later. Pd$-$Si alloys containing 15.5 to $23\,\mathrm{at.\%}$ Si [3] were stable at room temperature and did not exhibit any sign of crystallinity even after one month at $250\,^{\circ}\mathrm{C}$. A couple of years later, the Turnbull group found several ternary Pd$-$Si$-$X (X = Ag, Cu, Au) [4] alloys forming glasses at temperatures as low as $10^2\,^{\circ}\mathrm{C/s}$ with thicknesses more than $0.5\,\mathrm{mm}$ after an extensive survey of different compositions. The same group achieved thicknesses on the order of $1\,\mathrm{mm}$ after investigating various Pd$-$P$-$X (X = Ni, Co, Fe) [5] alloys. In 1967, Ruhl et al. showed that metallic glasses did not necessitate metalloid elements when they reported splat-quenched Nb$-$Ni, and Ta$-$Ni [6] alloys having amorphous structures.

A breakthrough was achieved in the late '60s when Chen and Turnbull were able to observe the glass-transition temperature of splat-quenched Au – Si and Au – Ge – Si alloys through thermal and rheological studies [7]. Observation of the glass-transition temperature indicated the presence of amorphous structures in these samples; thus, evidence of metallic glasses was provided. In the '70s, Chen et al. [8, 9] and Liebermann et al. [10] invented the *centrifugal spinning* method and successfully formed several glassy alloy ribbons. The invention of the centrifugal spinning method, also known as *melt spinning*, ultimately led to the extensive survey of compositions that form amorphous structures.

Kendall et al. from Jet Propulsion Laboratory (JPL) were able to obtain spherical Au – Pb – Sb [11] alloys with diameters up to $1.5\,\mathrm{mm}$ in 1982. The Inoue group further increased the critical thicknesses of the MGs up to $5\,\mathrm{mm}$ for the Al – La – Ni [12] system and around $9\,\mathrm{mm}$ for the Al – La – Cu [13] system. Melt-spun Mg – Ni – Y [14] and injection cast Mg – Cu – Y [15] alloys were found to have a fully amorphous structure by the Inoue group in 1991, with critical diameters up to $4\,\mathrm{mm}$ for the as-cast $Mg_{65}Cu_{25}Y_{10}$. They also observed that Mg – Cu – Y alloy retained its fully amorphous structure even after etching at room temperature for $Mg_{80}Cu_{10}Y_{10}$.

Furthermore, the Inoue group discovered the Zr – Al – X (X = Co, Ni, Cu) [16] system with significant glass-forming ability in 1991 with a broad supercooled liquid region between the glass transition temperature (T_g) and the onset temperature of crystallization (T_x) as high as $127\,\mathrm{K}$. The first commercial metallic glass was invented in 1992 as a part of a NASA-funded project to invent new aerospace materials. Peker et al. studied the pentary Zr – Ti – Cu – Ni – Be system and developed an alloy with critical thickness up to $10\,\mathrm{cm}$. $Zr_{41.2}Ti_{13.8}Cu_{12.5}Ni_{10.0}Be_{22.5}$ [17] alloy called Vitreloy 1 (*Vit 1*) exhibits critical cooling rates of the order of $10\,\mathrm{K\,s^{-1}}$ or less.

1.1.2 Glass Forming Ability

Almost all MG-forming alloys are attributed to varying glass-forming ability (GFA). The MGs that are more stable at room temperature and can be obtained with relatively slow cooling rates with larger sizes have better glass-forming abilities. The empirical rules for MG formation were first realized by Inoue et al. [18, 19], which were;

- multicomponent system incorporating more than three elements,
- atomic size mismatch above 12% between constituent elements, and
- negative heat of mixing between the components.

Cohen and Turnbull [20] were one of the first researchers to propose a semi-quantitative criterion for glass-forming tendency. Their proposal states that all liquids, including metallic and ionic, exhibit a greater glass-forming tendency with decreased reduced melting temperature, $\tau_m = kT_m/h_v$, where T_m is the equilibrium crystallization/melting temperature, and h_v is the heat of vaporization. Their statement points out that the alloy compositions close to a low melting eutectic point in the phase diagram are more susceptible to glass formation. The statement acted as a guide for searching for compositions that can be quenched into a glass. Turnbull also proposed a quantitative parameter called reduced glass temperature $T_{rg} = T_g/T_m$ [21]. According to Turnbull, liquids with a reduced glass temperature $\sim 1/2$ can be quenched to glassy form only at high cooling rates. However, a liquid with a reduced glass temperature as high as $\sim 2/3$ can be undercooled to obtain a glassy structure.

When a liquid is cooled below its melting point, the free energy difference between the liquid and the crystal acts as a driving force for crystal nucleation. In contrast, the formation of the liquid-crystal interface produces a positive interfacial energy that opposes nucleation. Tracking both the crystal nucleation driving force and the interfacial energy formed between the liquid-crystal interface can also be used to predict glass formation via the crystal nucleation rate, I_v [22].

The crystal nucleation rate per unit volume is defined as follows:

$$I_v = \frac{A_v}{\eta\left(T\right)} \exp\left(-\frac{\Delta G^*}{k_b T}\right) \tag{1.1}$$

where $\eta\left(T\right)$ is the temperature-dependent viscosity, k_B is the Boltzmann constant and A_v is a constant. ΔG^* is the activation energy for the formation of a nucleus and is defined as $\Delta G^* = 16\pi\sigma^3/3\left(\Delta G_{l-s}\right)^2$, where σ is the interfacial energy between the nuclei and the liquid. The driving force for the crystallization is defined as, $\Delta G_{l-s} = G_l - G_s$, where G_l and G_s are the Gibb's free energies of the liquid and the nuclei, respectively. The kinetic slowdown of a melt is often described by its viscosity. As seen in Equation (1.1), the viscosity is also an important parameter in predicting glass formation. The viscosity of melts generally obeys the following Arrhenius type of equation [23] with respect to temperature:

$$\eta = \eta_0 \exp\left(\frac{E}{RT}\right) \tag{1.2}$$

where E is the activation energy for the flow, R is the gas constant, and η_0 is a pre-exponential constant that corresponds to the viscosity at infinite temperature. However, the temperature dependence of the melts of MGs was found to be satisfactorily described by the modified Vogel–Fulcher–Tammann (VFT) relation of Angell [24]:

$$\eta = \eta_0 \exp\left[\frac{DT_0}{(T - T_0)}\right] \tag{1.3}$$

where T_0 is known as the VFT temperature, and D is the parameter that defines how well the equation obeys the Arrhenius law. The glass transition temperature is defined as the temperature at which the liquid has a viscosity of $10^{12}\,\mathrm{Pa\,s}$ [25]. Equations (1.2) and (1.3) can be fitted together to predict the glass transition temperature of a melt.

1.1.3 Metallic Glass Classifications

The first MG alloys were obtained as $\mu\mathrm{m}$ thick ribbons. In 1984, the Turnbull group formed the first centimeter-scale *bulk* MG by cooling the $Pd_{40}Ni_{40}P_{20}$ alloy of the same group in molten B_2O_3 fluxes [26] to suppress superficial crystallinity reported in earlier studies [27]. The term bulk metallic glass (BMG) defines MG alloys with thicknesses over $1\,\mathrm{cm}$ and critical cooling rates lower than around 10^2–$10^3\,\mathrm{K\,s^{-1}}$. Pd – Ni – P alloys of the Turnbull group were the first MGs on a centimeter-scale; hence, they are considered the first BMGs. The MGs proposed up to the late '80s were all consist of rather expensive elements like Pd, Pt, and Au [3, 28, 1]. The number of discovered MG compositions exponentially increased after the Inoue group came up with multicomponent MG systems mainly consisting of affordable, common metallic elements. Inoue group then classified the MGs that both they synthesized and reported in the literature into two categories: ferrous and nonferrous. They further divided the alloy compounds into five groups based on the types of the constituent elements [19]. The MGs are also frequently classified according to their base components, e.g., Zr- [29], Cu- [30], Fe- [31], Co- [32], and Al-based alloys are just a few examples.

As stated earlier, the BMGs require cooling rates $\sim 10^2$–$10^3\,\mathrm{K\,s^{-1}}$. On the other hand, the marginal metallic glass formers are a group of materials that require cooling rates of $\sim 10^5$–$10^6\,\mathrm{K\,s^{-1}}$ to vitrify fully. Among the marginal glass formers, Al-based alloys are particularly striking. First Al-rich MGs were Al – (Fe or Co) – B [33] and Al – Fe – (Si or Ge) [34]. They were highly brittle, though, and received little attention until a more ductile alloy surfaced [35]. Al – Ni – Si and Al – Ni – Ge systems with Al contents above $80\,\mathrm{at.\%}$ were the first alloys to exhibit good ductility [36]. An Al-based amorphous alloy with a tensile fracture strength value that exceeds $1000\,\mathrm{MPa}$ was produced in an Al – Y – Ni system in 1988. Al-rich $Al_{87}Y_8Ni_5$ alloy was found to exhibit tensile strengths that reached $1140\,\mathrm{MPa}$, which was about two times higher than the conventional Al-based crystalline alloys at that time [37]. He et al. reported Al-rich alloys with high GFA in 1992. Al – Ni – Fe – Gd system was found to require critical cooling rates comparable with some of the best glass formers in those days [38].

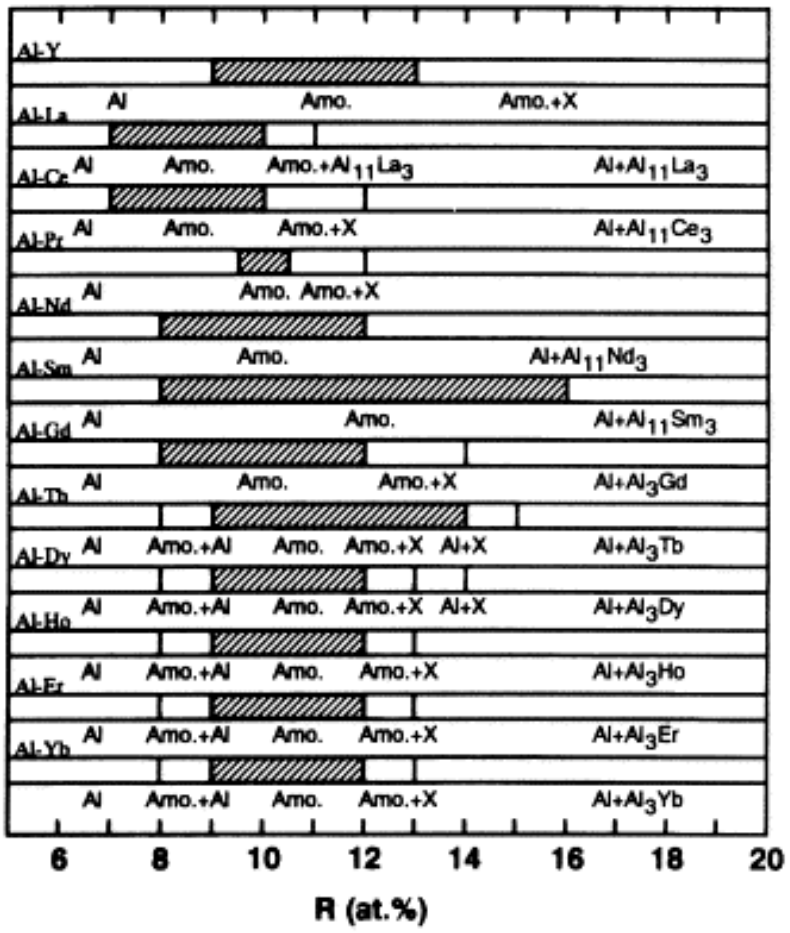

Figure 1.3: Composition ranges for the formation of an amorphous phase in melt-spun Al–RE (RE = Y, La, Ce, Pr, Nd, Sm, Gd, Tb, Dy, Ho, Er, or Yb) binary alloys. The symbols of Amo. and X represent amorphous and unidentified crystalline phases, respectively. Adopted from [39].

Remarkable mechanical properties of Al alloys with rare earths (RE) and transition metals (TM) have attracted attention [40, 41, 42]. Figure 1.3 shows the compositional dependence of the Al–RE (RE = Y, La, Ce, Pr, Nd, Sm, Gd, Tb, Dy, Ho, Er, or Yb) binary alloys for the formation of amorphous structure [39]. Among all 12 Al – RE systems Inoue has studied, the Al – Sm system has the widest glass-forming range of 8–16 at.%. The glass transition temperature generally appears as an endothermic peak in differential scanning calorimetry (DSC) traces. However, for some of the marginal glass-forming systems such as, Al – Y – Fe and Al – Sm, the endothermic glass transition temperature response coincides with the exothermic response from

the primary crystallization upon heating [43, 44]. Hence, conventional calorimetry analysis via DSC can not be used to identify glass formation for these alloys. Wu et al. have been able to observe the glass transition temperature of $Al_{92}Sm_8$ alloys by utilizing modulated-temperature differential scanning calorimetry (MTDSC) [45].

An important and interesting observation in several marginal glass-forming alloys is the formation of a very high nucleation density of nanocrystals. Upon devitrification, nanocrystal densities can be obtained on the order of 10^{21} to $10^{23}\,\mathrm{m}^{-3}$ [44] [46]. Additionally, contrary to most of the bulk metallic glasses and several empirical MG formation rules, marginal glass formers can form glasses far from the eutectic point [47].

1.2 Simulation Methods to Model Metallic Glasses

1.2.1 Reverse Monte Carlo Modeling

Reverse Monte Carlo (RMC) is a computational method for generating three-dimensional models of mainly disordered materials, such as liquids and glasses, consistent with one or more experimental data[48, 49, 50]. In that sense, RMC differs from other computational simulation methods because experimental data directly drive it. However, some additional empirical constraints can be incorporated in order to achieve a sounder model since a single experimental study will only give limited data to describe the whole structure.

An RMC simulation initiates with an input of the initial configuration of atoms. The configuration may be randomly generated, or the output of another simulation can be used as the starting configuration. Then, the parameter corresponding to the experimental data is calculated to be compared with it. The atomic coordinates of each atom are randomly displaced to increase the agreement with the experimental data. The agreement between the obtained model and the experimental data is monitored through the chi-squared test. The chi-squared test is defined as follows:

$$\chi^2 = \sum_j \left(y_j^{exp} - y_j^{calc}\right)/\sigma_j^2 \tag{1.4}$$

where the summation is over all data points and σ_j is the weighting factor also known

as the confidence interval. y_j^{exp} and y_j^{calc} are the experimental and calculated parameters, respectively.

An RMC run aims to minimize the value of χ^2 by means of successive changes in the configuration. The RMC depends on the Monte Carlo algorithm in which each subsequent change in configuration is tested to assess whether the change improves the agreement with the experimental data. If the assessment succeeds through the chi-squared test, the proposed change is accepted, and the algorithm advances to the change. To avoid getting stuck in a local minimum in the search for the global minimum, the RMC uses a probability algorithm to determine whether the proposed changes that decrease the agreement with experimental data are accepted or not. The probability algorithm used in the RMC simulations accepts the proposed change that decreases the agreement with the experimental data with the probability $\exp\left(-\Delta\chi^2/2\right)$ where $\Delta\chi^2$ is the amount of increase observed in χ^2 with the current proposed change with respect to the preceding one. This helps the model to converge towards the global minimum to obtain a more reliable structure.

The most frequently employed experimental data in RMC simulations are the total scattering data, including the total structure factor and total pair distribution function. The limitations in describing the structures for total scattering data lead to the integration of further experimental constraints into the RMC. Those additional constraints include experimental data like partial structure factors, partial pair distribution functions, extended X-ray absorption fine structure (EXAFS), X-ray absorption near edge structure (XANES), fluctuation electron microscopy (FEM), and geometrical like cutoffs, bond angles, coordination numbers, and neighbor specifications. However, RMC studies are often regarded as biased since there might be several atomistic structures that can successfully fit the experimental data. Some of the examples of readily available RMC software are as follows: RMC++ [51], RMCprofile [52], and fullrmc [53].

1.2.2 Molecular Dynamics

Steps to follow to experiment in a laboratory environment are roughly like the following: first, the sample to be studied should be prepared, then the sample should be paired to an instrument to measure one or many properties during the course of the experiment. Subsequently, the experiment should be conducted along with data collection via the measurement instrument. Finally, the obtained data are analyzed with the help of some statistical methods, and a conclusion is reached. The molecular dynamics (MD) method utilizes exactly the same process steps to simulate the physical movements of atoms or molecules under various conditions. Although studies with MD have gained momentum and applied extensively in the recent past as a result of developments in computational power, this method was actually put forward in the '50s [54, 55].

In essence, MD is a computational simulation method that tracks and stores the time evolution of a set of particles/atoms, and Newton's equation of motion governs the evolution of the system. The MD yields the positions and the velocities of each atom, called a *trajectory*, with respect to time. Those trajectories are then analyzed to extract the static and dynamic properties of the system being simulated based on classical statistical mechanics. In MD, the trajectories are obtained via solving the following famous Newton's equation of motion for each of the interacting particles:

$$\boldsymbol{F}_i = m_i \boldsymbol{a}_i = m_i \frac{d\boldsymbol{v}_i}{dt} = m_i \frac{d^2 \boldsymbol{r}_i}{dt^2} = \frac{d\boldsymbol{p}}{dt} \tag{1.5}$$

where m_i is the particle's mass, $\boldsymbol{a}_i$ is the acceleration vector, $\boldsymbol{v}_i$ is the velocity vector, $\boldsymbol{r}_i$ is the particle's position vector containing each coordinate, (x_i, y_i, z_i), and $\boldsymbol{p}$ is the particle's momentum. The force acting on each atom caused by all $N - 1$ other ones can be expressed as the negative gradient of a potential, U, with respect to the positions of the atoms.

$$
\begin{aligned}
\boldsymbol{F}_i &= -\nabla_i U\left(\boldsymbol{r}_1, \boldsymbol{r}_2, \ldots, \boldsymbol{r}_N\right) \\
&= -\nabla_i U\left(\boldsymbol{r}^N\right) \\
&= -\left(\frac{\partial U\left(\boldsymbol{r}^N\right)}{\partial x_i}\hat{x} + \frac{\partial U\left(\boldsymbol{r}^N\right)}{\partial y_i}\hat{y} + \frac{\partial U\left(\boldsymbol{r}^N\right)}{\partial z_i}\hat{z}\right)
\end{aligned}
\tag{1.6}
$$

Equation (1.6) shows that the gradient is taken on each coordinate; this makes the solution of Newton's equation of motion correspond to a set of $6N$ ordinary differential equations ($3N$ for positions and $3N$ for momenta) for a system of N atoms/particles. The origin of the potential needed to solve Equation (1.6) is purely quantum mechanical. However, simplified descriptions have been proposed due to the immense computational power required to quantum mechanically calculate the whole potential surface. The Lennard-Jones (L-J) potential [56, 57, 58], shown in Equation (1.7), is one of the simplest pair-potential to describe interatomic interactions. It represents the interactions between closed-shell atoms fairly well, simply by a sum of two-body interactions.

$$
U_{\mathrm{LJ}}\left(\boldsymbol{r}\right) = 4\varepsilon\left[\left(\frac{\sigma}{\boldsymbol{r}}\right)^{12} - \left(\frac{\sigma}{\boldsymbol{r}}\right)^{6}\right] \tag{1.7}
$$

where ε is the absolute value of the minimum of the potential, which corresponds to the strength of the interaction. σ is the distance at which the potential is zero, also described as the radius of the repulsive core. The vector $\boldsymbol{r}$ is the distance vector between a pair of particles, i.e., $\boldsymbol{r} = |r_j - r_i|$ for particles i and j. Figure 1.4 shows a comparison of an experimentally obtained interatomic potential with a Lennard-Jones fit. It is seen that the short-range interaction term $1/r^{12}$ can not provide a fully accurate description. Even though the Lennard-Jones potential does not cover any multi-body interactions beyond the two-body, it yields good results, especially between the rare-gas atoms. Developing interatomic potentials for more complex systems is rather complicated. Metals, for example, can not be satisfactorily described using pair potentials. With delocalized valence electrons occurring like an electron cloud, metals exhibit additional forces that simple pair potentials just can not depict. A simple addition to the pair potentials has been shown to adequately approximate the many-body aspects of metals. The embedded atom method (EAM) potentials [60, 61]

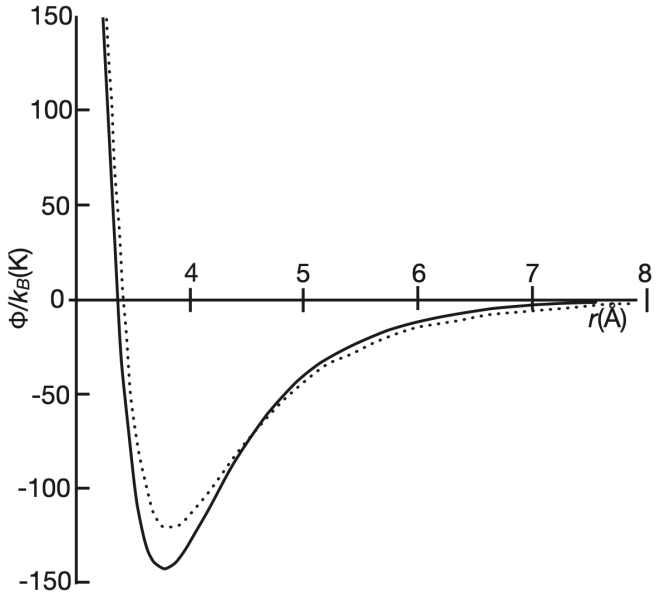

Figure 1.4: A comparison of an experimental Ar – Ar interatomic potential with a Lennard-Jones 12-6 potential. Solid line is the experimental Ar – Ar potential obtained via a molecular beam scattering experiment while dashed line is the best Lennard-Jones fit to that potential. Adapted from [59].

contain a term for embedding energy, F_i, as a functional of the local electron density, $\overline{\rho}_i$. The embedding energy term is nothing more than the energy required to embed atom cores into an electron cloud with a density of $\overline{\rho}_i$. The EAM potentials generally have a form as in Equation (1.8).

$$U_{\text{EAM}}\left(\boldsymbol{r}_{ij}\right) = \sum_{i=1}^{N} \sum_{j>i}^{N} \phi_{ij}\left(\boldsymbol{r}_{ij}\right) + \sum_{i} F_i\left(\overline{\rho}_i\right) \tag{1.8}$$

where $\phi_{ij}\left(\boldsymbol{r}_{ij}\right)$ is a two-body potential that depends only on the interatomic distance between the pair of particles, and $F_i\left(\overline{\rho}_i\right)$ is a functional of the local electron density, $\overline{\rho}_i$. Equation (1.9) shows that the local electron density is a pair function as a sum of electron density contributions of neighboring particles.

$$\overline{\rho}_i = \sum_{j \neq i} \rho_j\left(\boldsymbol{r}_{ij}\right) \tag{1.9}$$

Apart from the aforementioned Lennard-Jones and EAM potentials, there are many more interatomic potentials out there in the literature. Mie [62], Born-Mayer-Huggins [63, 64], and Buckingham [65] are some of the pair-potentials, whereas Stillinger-

Weber [66] and Tersoff [67] are 3-body. Also, ReaxFF [68] and REBO [69] potentials are used to correctly model bond breaking/forming for simulating reactions.

Solving $6N$ differential equations of Newton's equation of motion for N-atom systems via Equation (1.6) is the most computationally expensive part of an MD run. There are several commonly used algorithms to tackle this problem efficiently; a couple of them will be introduced in the following part. The first one, called the Verlet algorithm, was proposed in 1967 by Loup Verlet [70] and follows the Kinematic equations [71]. The algorithm can be derived by writing the Taylor expansions of both forward and backward positions in time up to the third-order terms as follows:

$$\begin{aligned} \boldsymbol{r}\left(t+\Delta t\right) &= \boldsymbol{r}\left(t\right) + \boldsymbol{v}\left(t\right)\Delta t + \frac{1}{2}\boldsymbol{a}\left(t\right)\Delta t^2 + \ldots \\ \boldsymbol{r}\left(t-\Delta t\right) &= \boldsymbol{r}\left(t\right) - \boldsymbol{v}\left(t\right)\Delta t + \frac{1}{2}\boldsymbol{a}\left(t\right)\Delta t^2 + \ldots \end{aligned} \tag{1.10}$$

and adding the above two equations concludes this simple yet effective algorithm, as seen in Equation (1.11).

$$\boldsymbol{r}\left(t+\Delta t\right) = 2\boldsymbol{r}\left(t\right) - \boldsymbol{r}\left(t-\Delta t\right) + \boldsymbol{a}\left(t\right)\Delta t^2 + \mathcal{O}(\Delta t^4) \tag{1.11}$$

Given a set of positions at the current time, t, and at the previous time, $t-\Delta t$, Equation (1.11) can be solved explicitly to obtain the positions at time $t+\Delta t$ with an associated error as low as $\mathcal{O}(\Delta t^4)$. One of the drawbacks of the above algorithm is the lack of velocity term, which is required to compute several physical properties of a system, most notably kinetic energy with $1/2mv^2$. Verlet algorithm solves this deficiency by subtracting the latter equation from the former in Equation (1.10) to approximate the velocity as follows:

$$\boldsymbol{r}\left(t+\Delta t\right) - \boldsymbol{r}\left(t-\Delta t\right) = 2\boldsymbol{v}\left(t\right)\Delta t + \mathcal{O}(\Delta t^2) \tag{1.12}$$

and solving for $\boldsymbol{v}\left(t\right)$:

$$\boldsymbol{v}\left(t\right) = \frac{\boldsymbol{r}\left(t+\Delta t\right) - \boldsymbol{r}\left(t-\Delta t\right)}{2\Delta t} + \mathcal{O}(\Delta t^2) \tag{1.13}$$

It should also be noted that in order to estimate the velocity term at the current timestep t with Equation (1.13), the positions at the following timestep $t+\Delta t$ are

necessary. The velocity term of the next time step $t + \Delta t$ can be estimated at the cost of accuracy, with a poor error of $\mathcal{O}(\Delta t)$ as follows:

$$\boldsymbol{v}\left(t + +\Delta t\right) = \frac{\boldsymbol{r}\left(t + \Delta t\right) - \boldsymbol{r}\left(t\right)}{\Delta t} + \mathcal{O}(\Delta t) \tag{1.14}$$

Although the Verlet algorithm is simple and effective in calculating the positions of particles with only one force calculation at each timestep, the requirement for the positions at a preceding timestep at the initialization makes this algorithm prone to error accumulation [72]. An improved algorithm that handles positions *and* velocities at time $t + \Delta t$ simultaneously, called the *Velocity-Verlet* algorithm, was introduced in 1982 [73, 74] and is currently one of the most widely used algorithms in the MD community to solve Newton's equation of motion. Several alternative algorithms that deal with the shortcomings of the previously mentioned algorithm also exist. Leap-frog [75], Beeman [76], and Predictor–corrector [77] are some of the examples, and the reader is referred to the corresponding references to acquire additional information on each one of them.

Statistical averaging should be done after a satisfactory equilibrium is attained to extract useful information from an MD run. See Figure 1.5 for an example MD run. Several thermodynamic properties can be observed during an MD run to keep track of the convergence to equilibrium. Figure 1.5 shows an example Lennard-Jones MD run with equilibration and production parts. In MD, this can be achieved by performing time averaging. For a hypothetical property A, the time averaging is as follows:

$$\langle A \rangle = \lim_{t \to \infty} \frac{1}{t} \int_{t_0}^{t_0 + t} A\left(\tau\right) d\tau \tag{1.15}$$

where t_0 denotes the time at which the equilibrium is reached, and $A\left(\tau\right)$ is the instantaneous value of the property A at time τ. The MD simulations are performed over a finite time interval, thus the limit in Equation (1.15) can not approach infinity. To yield a satisfactory average, the averaging should be done over a long time span, and a summation replaces the limit notation in Equation (1.15). The actual averaging thus can be done using the following equation:

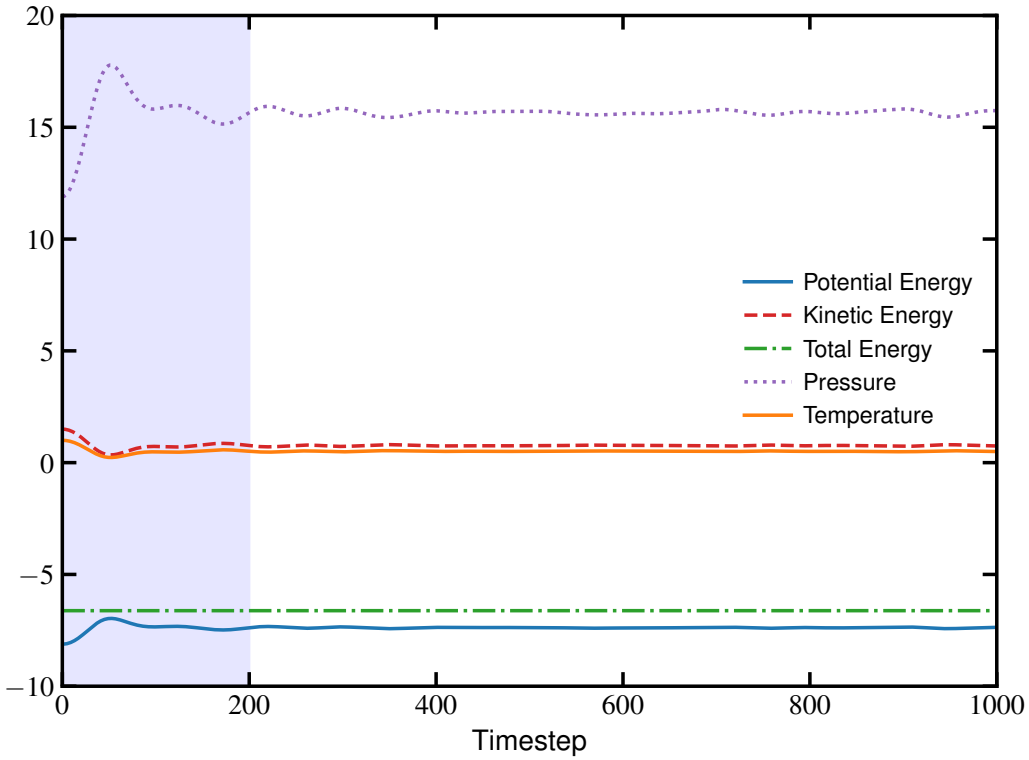

Figure 1.5: An example molecular dynamics run employing the Lennard-Jones 12-6 potential with reduced density of $\rho/\sigma^3 = 1.2$ and reduced temperature of $T/\epsilon k_B^{-1} = 1.0$. The highlighted first 200 timesteps show roughly the initial equilibration part.

$$\langle A \rangle \approx \frac{1}{t_f} \int_{t_0}^{t_0+t_f} A(t)dt = \frac{1}{t_f/\Delta t} \sum_{i=1}^{t_f/\Delta t} A_i \tag{1.16}$$

where t_f is the time at which the MD simulations conclude and A_i denotes the data point of the hypothetical property A at a given time. One should be aware of the systematic and statistical errors Equation (1.16) subject to and take great care to estimate the associated errors by performing block averages or using correlation functions. There are quite a number of open- or closed-source software that can be used for molecular dynamics calculations: CHARMM [78], DL_POLY [79], GROMACS [80], HOOMD [81], and LAMMPS [82, 83], just to name a few.

1.2.3 *ab initio* Methods

Classical MD studies require predefined interatomic potentials, or force fields, based on empirical data and/or rigorous electronic structure calculations. With elaborate interatomic potentials, the MD gives pretty realistic results. However, the development of satisfactory interatomic potentials is substantially time-consuming and tedious. Often referred to as *ab initio* molecular dynamics (AIMD) or quantum molecular dynamics (QMD), first-principle methods based on quantum mechanics eliminate the requirement of predetermined interatomic potentials yet comes with their own caveats. At its most basic definition, the AIMD method is used to compute forces acting on particles *on-the-fly* as the system evolves via Newton's equation of motion. Utilization of the AIMD is particularly favorable in the case of complex materials for which the requirements for the interatomic potential development are almost impossible to meet.

The rudimentary property to obtain during an AIMD simulation is the energy of each particle to determine the forces acting on each atom. Since an atom's nucleus is considerably heavier than the electrons bound to it, *Born-Oppenheimer* (BO) *approximation* states that the mathematical solutions regarding the nuclei and the electrons can be treated separately. The BO approximation is especially beneficial in MD simulations for which the ground state energy of the electrons of a given set of particles can be calculated for fixed positions of the atomic nuclei. In 1926 Erwin Schrödinger introduced an equation that looks relatively simple but has the potential to explain the entire universe. Named after the man himself, the Schrödinger equation sets the basis for quantum mechanics, as Newton's law is for classical mechanics, and it is defined as follows:

$$\hat{\mathcal{H}} \left|\Psi\right\rangle = E \left|\Psi\right\rangle \tag{1.17}$$

where $\hat{\mathcal{H}}$ is the Hamiltonian operator, E is the energy, and Ψ is the eigenstates of the Hamiltonian, also known as the wavefunctions. The description in Equation (1.17) mainly depends on the system being described. A more suitable description of the Schrödinger equation for the case of multiple nuclei interacting with multiple electrons is given in Equation (1.18).

$$\left[-\frac{\hbar^2}{2m}\sum_{i=1}^{N}\nabla_i^2+\sum_{i=1}^{N}V\left(\boldsymbol{r}_i\right)+\sum_{i=1}^{N}\sum_{j<i}U\left(\boldsymbol{r}_i,\boldsymbol{r}_j\right)\right]\Psi=E\Psi \tag{1.18}$$

where $\hbar$ is the reduced Planck constant, and m is the mass of a single electron. In Equation (1.18), the first term in brackets denotes the kinetic energy of N electrons, the second term is the attractive potential energies of N electrons due to the nuclei, and the last term is the repulsive potential energies of N electrons between each other. The E on the right-hand side of the Equation (1.18) is the ground-state energy of the particle associated with the electronic wavefunction Ψ, where Ψ is a function of all of the spatial coordinates of each of the N electrons, i.e., $\Psi=\Psi\left(\boldsymbol{r}_1,\boldsymbol{r}_2,\ldots,\boldsymbol{r}_N\right)$. The many-body problem in the determination of the wavefunction Ψ can be simplified using *Hartree products* where the many-particle wavefunctions approximated to be equal to the product of the wavefunctions of the individual particles. An alternative way to map the many-body problem of the Schrödinger equation onto a single-body problem is to use the electron density, which is defined as follows:

$$n\left(\boldsymbol{r}\right)=2\sum_{i}\Psi_i^*\left(\boldsymbol{r}\right)\Psi_i\left(\boldsymbol{r}\right) \tag{1.19}$$

where the asterisk above the first wavefunction indicates a complex conjugate, and the summation is over all the single-electron wavefunctions where the coefficient 2 is due to the *Pauli exclusion principle*. The $n\left(\boldsymbol{r}\right)$ is the density of electrons at position $\boldsymbol{r}$, and the wavefunction Ψ is a unique functional of $n\left(\boldsymbol{r}\right)$, i.e., the electron density $n\left(\boldsymbol{r}\right)$ can be used to calculate the corresponding wavefunction Ψ.

The first theorem of Hohenberg and Kohn states that *the ground state energy of the Schrödinger's equation is a unique functional of the electron density*, which can be interpreted as $E\left[n\left(\boldsymbol{r}\right)\right]$. The second theorem of Hohenberg and Kohn defines the electron density corresponding to the exact solution of the Schrödinger's equation as the one that minimizes the total energy of the proposed functional. These two groundbreaking theorems reduced the many-body problem of N electrons with $3N$ spatial coordinates to just three spatial coordinates and laid the foundation of the now-famous *Density Functional Theory* (DFT).

The functional described by Hohenberg and Kohn can be written in terms of the single-electron wavefunctions, $\Psi_i(\boldsymbol{r})$, as seen in Equation (1.20).

$$\begin{aligned} E[\{\Psi_i\}] = & -\frac{\hbar^2}{m}\sum_i \int \Psi_i^* \nabla^2 \Psi_i d^3r \\ & + \int V(\boldsymbol{r})\, n(\boldsymbol{r})\, d^3r \\ & + \frac{e^2}{2}\iint \frac{n(\boldsymbol{r})\, n(\boldsymbol{r}')}{|\boldsymbol{r}-\boldsymbol{r}'|} d^3r d^3r' \\ & + E_{\text{ion}} \\ & + E_{\text{XC}}[\{\Psi_i\}] \end{aligned} \tag{1.20}$$

where the first four terms denote the electron kinetic energies, the Coulomb interactions between the electrons and the nuclei, among pairs of electrons, and between pairs of nuclei, respectively. The last term, $E_{\text{XC}}[\{\Psi_i\}]$, is known as the exchange-correlation functional, and it includes all other interactions that are not specified in the first four terms. The energy functional proposed by Hohenberg and Kohn is exceptionally powerful, yet it does not provide a way to compute a system's ground state electron density. Kohn and Sham suggested a solution to this drawback by decomposing a system of N interacting electrons into that of N non-interacting one-electrons that generates the same electron density as a system of interacting electrons. The resulting equations, known as the Kohn-Sham equations, have the following form:

$$\left[-\frac{\hbar^2}{2m}\nabla^2 + V(\boldsymbol{r}) + V_H(\boldsymbol{r}) + V_{XC}(\boldsymbol{r})\right]\Psi_i(\boldsymbol{r}) = \varepsilon_i \Psi_i(\boldsymbol{r}) \tag{1.21}$$

where V_H is known as Hartree potential, and V_{XC} is defined as exchange-correlation potential, which is the derivative of the exchange-correlation energy, E_{XC}. There are several approximate formulations for the yet-unknown exchange-correlation functional. Local density approximation (LDA) and generalized gradient approximation (GGA) are just two of them, and their explanation is beyond the scope of the present study.

The solution of the Kohn-Sham equations is self-consistent with an initial guess of electron density, $n(\boldsymbol{r})$. The procedure to solve the Kohn-Sham equations is as follows: The one-electron wavefunctions of the Kohn-Sham equations should first be found using a trial electron density. Then, using Equation (1.19), the electron density defined by the one-electron wavefunctions must be calculated. Afterward, the initial trial electron density should be compared with the one found via Equation (1.19). If the two electron densities match, the ground state electron density is found, and it can be used to compute the system's total energy. If they differ, the electron density used to calculate the one-electron wavefunctions should be modified, and the whole process starts all over again. The connection between the *ab initio* electronic structure calculations defined earlier and MD is pioneered by Car and Parrinello. Their efficient algorithm unifies the evolution of nuclei with the electronic ground state search. Due to the fact that the AIMD requires the ground state energy to be calculated at every and each MD timestep, only small systems involving only ~ 1000 atoms can be simulated with reasonable computation times. Anything more would require rather long computation times. Also, force calculations via DFT are considerably more expensive than that of classical MD. The time-scale achievable by AIMD thus is in the order of $\sim$ps, and in such a short time span, the development of any significant order cannot be expected. Some of the proprietary and open-source software to conduct *ab initio* electronic structure calculations are as follows: ABINIT [84, 85], CASTEP [86], CP2k [87], SIESTA [88], Quantum Espresso [89, 90], and VASP [91, 92, 93].

CHAPTER 2

STRUCTURAL ANALYSIS OF METALLIC GLASSES

2.1 Pair Distribution Function

The Pair Distribution Function, $g(r)$, characterizes the spatial distribution of particles around any given one. It is one of the metallic glasses' most crucial static parameters that depend on the entire system. It represents the probability of finding an atom at a given distance away. For spatially homogeneous systems, it is defined as:

$$g(\boldsymbol{r}) = \frac{V}{N^2} \left\langle \sum_{i=1}^{N} \sum_{i \neq j}^{N} \delta \left(\boldsymbol{r} - \boldsymbol{r}_{ij}(t) \right) \right\rangle \tag{2.1}$$

where V and N are the volume of the system and the number of atoms in the system, respectively. $\boldsymbol{r}_{ij}(t)$ is the time-dependent interatomic distance between the particles i and j. The dirac delta function, δ, in Equation (2.1) is used for counting the number of atoms located at a distance, r, away from the central atom. Its value is zero, except the term $\boldsymbol{r} - \boldsymbol{r}_{ij}(t)$ is zero. As seen in Figure 2.1, g(r) can be obtained in a two-dimensional analogue by counting the number of atoms residing in a shell with a predetermined thickness of dr at a distance r away.

In some cases, it is useful to calculate the pair distribution function (PDF) for certain types of particles. These distribution functions, called partial pair distribution (PPDF) functions, serve to study the spatial arrangement of particles of certain types. The element-specific pair distribution function in Equation (2.2) is mainly used to analyze how particular types of atoms are distributed within the structure with respect to each other. There are $M(M+1)/2$ partial pair distribution functions that exist in a multicomponent atomic system consisting of M distinguishable components.

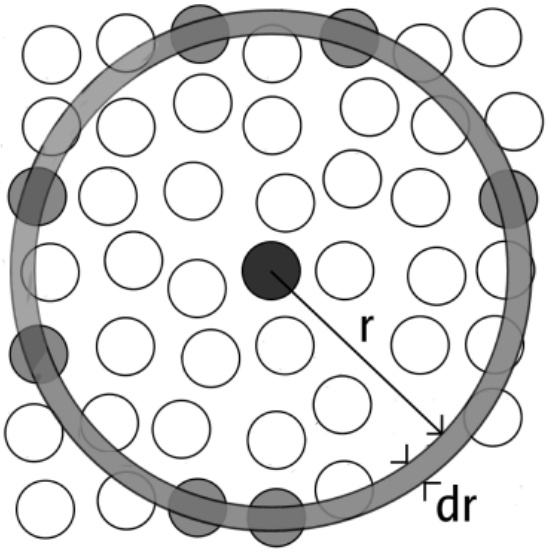

Figure 2.1: A representative two dimensional structure showing the binning procedure to calculate pair distribution function. r is the distance between the dark colored center particle and the shaded shell with a thickness dr. The number of particles coincides with the shaded shell corresponds to the respectively $g(r)$ at distance r. Adopted from [94].

$$g_{ij}(\boldsymbol{r}) = \frac{N}{4\pi r^2 \rho N_i N_j} \left\langle \sum_{i=1}^{N_i} \sum_{j=1}^{N_j} \delta\left(\boldsymbol{r} - \boldsymbol{r}_{ij}(t)\right) \right\rangle \tag{2.2}$$

The relationship between the partial pair distribution functions and the total pair distribution function is relatively straightforward. The total pair distribution function comprises all possible partial pair distribution functions. In fact, the basic double summation in Equation (2.3), over the components α and β for a hypothetical binary alloy, gives the total pair distribution function of the alloy.

$$g(r) = \sum_{\alpha} \sum_{\beta} g_{\alpha\beta}(r) \tag{2.3}$$

The pair distribution function is a histogram of all particle-particle distances in a material. Hence, below a certain distance, the value of the pair distribution function is zero. The value below which the $g(r)$ becomes zero is the closest distance a pair of particles can approach each other. The probability of finding a particle becomes independent of each other as the separation between the particles increases so that $\lim_{r\to\infty} g(r) = 1$ and the plots of $g(r)$ asymptotes to $g(r) = 1$. It is mathematically shown in Equation (2.4) for a two-particle system.

$$\begin{aligned} g(\boldsymbol{r} \to \infty) &= \frac{1}{\rho^2} \left\langle \sum_{i=1}^{N} \delta\left(\boldsymbol{r}^{'} - \boldsymbol{r}_i(t)\right) \right\rangle \left\langle \sum_{j\neq i}^{N} \delta\left(\boldsymbol{r}^{''} - \boldsymbol{r}_j(t)\right) \right\rangle \\ &= \frac{N(N-1)}{\rho^2} \frac{1}{V^2} = 1 - \frac{1}{N} \\ &\simeq 1 \end{aligned} \tag{2.4}$$

where ρ is the density of the system and vectors $\boldsymbol{r}^{'}$ and $\boldsymbol{r}^{''}$ correspond to the positions of two different particles. The position of the peaks gives information about the average distances and angles between the atoms, whereas the full width at half maximums of the peaks indicates the level of disorder. For crystalline solid materials, $g(r)$ consists of well-defined peaks at neighbor distances along with the broadening of the peaks that may arise due to thermal fluctuations of atoms or any disorder that might be present in the system, as seen in Figure 2.2a. One can differentiate the crystal structure the material consists of just by examining the $g(r)$. For example, an *fcc* structure will have definite peaks located at $a(\sqrt{1}, \sqrt{2}, \sqrt{3}, \sqrt{5}, \ldots)$ where a is the lattice parameter of the model structure. For liquid and amorphous materials, the $g(r)$ is rather featureless, see Figure 2.2b. Contrary to crystalline solids, amorphous and liquid materials exhibit broader peaks containing invaluable information about short-range order (SRO) and medium-range order (MRO). This is due to the somewhat disordered structures that those materials consist of. The first main peak of $g(r)$ features information about the SRO the system may have, whereas any subsequent features up to 1–$2\,\mathrm{nm}$ are due to MRO.

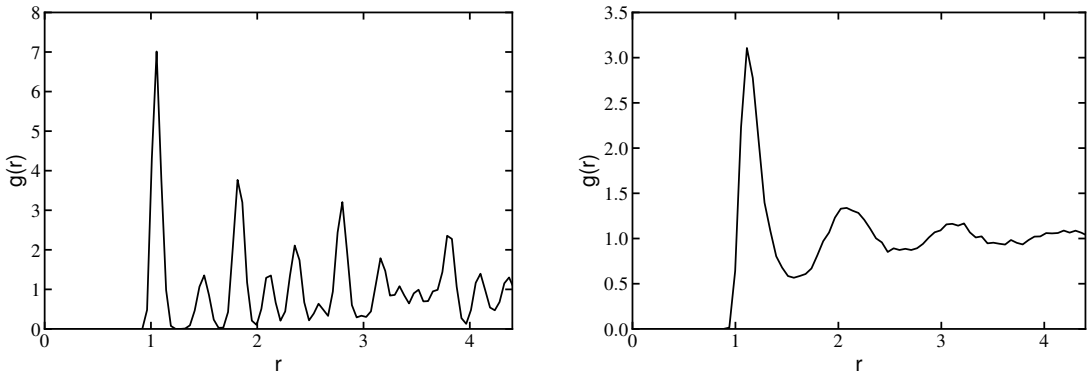

(a) (b)

Figure 2.2: Representative pair distribution functions for a Lennard-Jones 12-6 (a) *fcc* solid with reduced density of $\rho/\sigma^3 = 1.2$ and reduced temperature of $T/\epsilon k_B^{-1} = 1.0$, and (b) for a liquid with reduced density of $\rho/\sigma^3 = 0.8$ and reduced temperature of $T/\epsilon k_B^{-1} = 1.0$.

2.2 Structure Factor

The structure factor, $S(Q)$, is a static property of a system that is directly proportional to the measured intensity in X-ray or Neutron diffraction experiments in terms of the magnitude of the wavevector, Q. It can experimentally be obtained via total scattering experiments, mainly using high-intensity short-wavelength synchrotron radiation. It is primarily utilized in the research of disordered materials and is defined as follows

$$S(Q) = \frac{1}{N} \left\langle |\sum_{i=1}^{N} e^{iQ\boldsymbol{r}_i(t)}|^2 \right\rangle \tag{2.5}$$

The structure factor is the reciprocal-space equivalent of the pair distribution function. An interesting relationship exists between the structure factor and the pair distribution function: The Fourier transform of the pair distribution function yields the structure factor. This relationship between the structure factor and the pair distribution function allows the researchers to use the easily-obtainable structure factors to acquire structural information about a sample on an atomistic basis through the inverse Fourier transform.

The conversion between the structure factor and the pair distribution function can be done using Equation (2.6).

$$S(Q) = 1 + 4\pi n \int r^2 \left[g(r) - 1\right] \frac{\sin Qr}{Qr} dr \tag{2.6}$$

Similar to the discussion on partial pair distribution functions in Section 2.1, explicitly identifying the structure factor around a particular chemical species is often desirable. The conversion scheme given in Equation (2.7) is known as the *Faber-Ziman partials* [95] and can be used to convert the partial pair distribution functions to the partial structure factors.

$$S_{ij}(Q) = 1 + 4\pi n \int r^2 \left[g_{ij}(r) - 1\right] \frac{\sin Qr}{Qr} dr \tag{2.7}$$

An example structure factor can be seen in Figure 2.3 for $Al_{90}Sm_{10}$ alloy, where high-energy transmission synchrotron X-ray diffraction (HEXRD) studies were conducted at the Advanced Photon Source (APS) at Argonne National Laboratory [96].

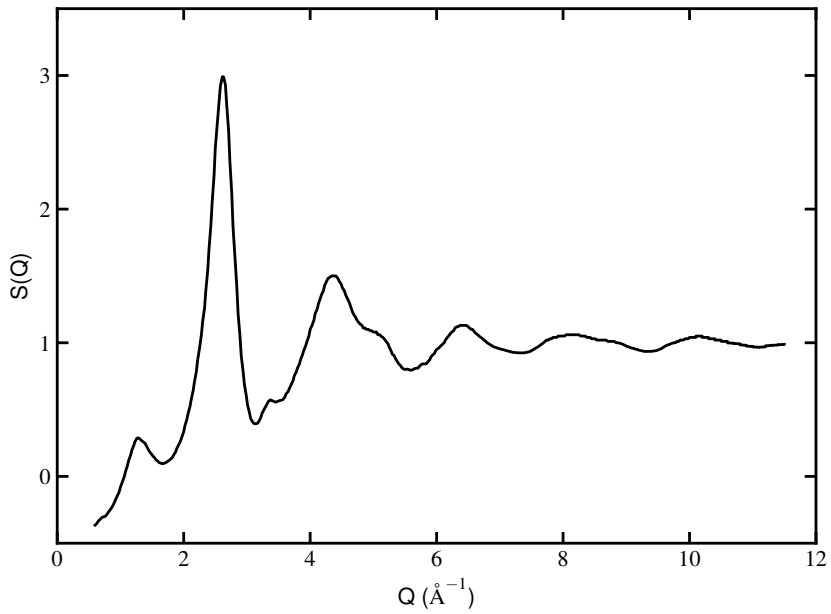

Figure 2.3: An example of total structure factor $S(Q)$ of as quenched $Al_{90}Sm_{10}$ at room temperature. Adopted from [96].

Each partial structure factor obtained with Equation (2.7) is exactly identical to $S(Q)$ that would be acquired if the entire sample was made up of only that partial. Those partials form the basis for *Faber-Ziman formalism*, where the total structure factor is basically the weighted sum of all possible partials, see Equation (2.8).

$$\begin{aligned} S(Q) &= \sum_i \sum_j \frac{c_i c_j f_i f_j}{\left(\sum_i c_i f_i\right)^2} S_{ij}(Q) \\ &= \omega_{ii} S_{ii}(Q) + \omega_{ij} S_{ij}(Q) + \omega_{jj} S_{jj}(Q) \end{aligned} \tag{2.8}$$

where the subscripts i and j refer to components of a binary system, respectively. The weight factors ω_{ij} are determined by the compositions of the two components, c_1 and c_2, and the Q-dependent atomic scattering factors $f_1(Q)$ and $f_2(Q)$ through Equation (2.9).

$$\begin{aligned} \omega_{ii} &= \frac{c_i^2 f_i^2(Q)}{\left[c_i f_i(Q) + c_j f_j(Q)\right]^2} \\ \omega_{ij} &= \frac{2 c_i c_j f_i(Q) f_j(Q)}{\left[c_i f_i(Q) + c_j f_j(Q)\right]^2} \\ \omega_{jj} &= \frac{c_j^2 f_j^2(Q)}{\left[c_i f_i(Q) + c_j f_j(Q)\right]^2} \end{aligned} \tag{2.9}$$

Figure 2.4 shows the rather interesting feature of marginal glass former alloys, pre-peak at lower Q space. Figure 2.4a displays the diffraction pattern of a well-known BMG system, Cu – Zr, that lacks the pre-peak.

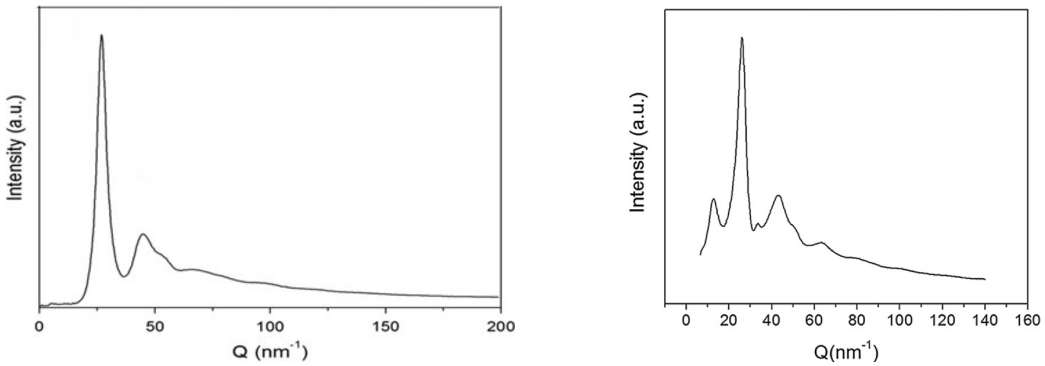

(a) (b)

Figure 2.4: HEXRD diffraction pattern of (a) the as-quenched $Cu_{50}Zr_{50}$ ribbon [97], and (b) the $Al_{90}Sm_{10}$ ribbon [98].

2.3 Coordination Number

On the atomistic scale, the coordination number is defined as the number of nearest neighbors a single atom has. The coordination number is mostly constant and well-defined for crystalline materials and depends only on the type of crystal a material consists of. Closed-packed structures like *fcc* and *hcp* materials have a coordination number of 12, whereas *bcc* materials have 8. Having a relatively low atomic packing factor, a simple cubic structure has a coordination value of only 6.

Contrary to crystal structures, the determination of coordination number is rather trivial for amorphous materials that lack the long-range order. There are several commonly used methods governing the determination of coordination number values for non-crystalline materials. The most straightforward one is to use the area under the first main peak of the PDF curve. The result of Equation (2.10) is considered the average number of the nearest neighbor of the system, hence the coordination number, by setting the r_1 and r_2 to minimums before and after the first main peak of a PDF curve, respectively.

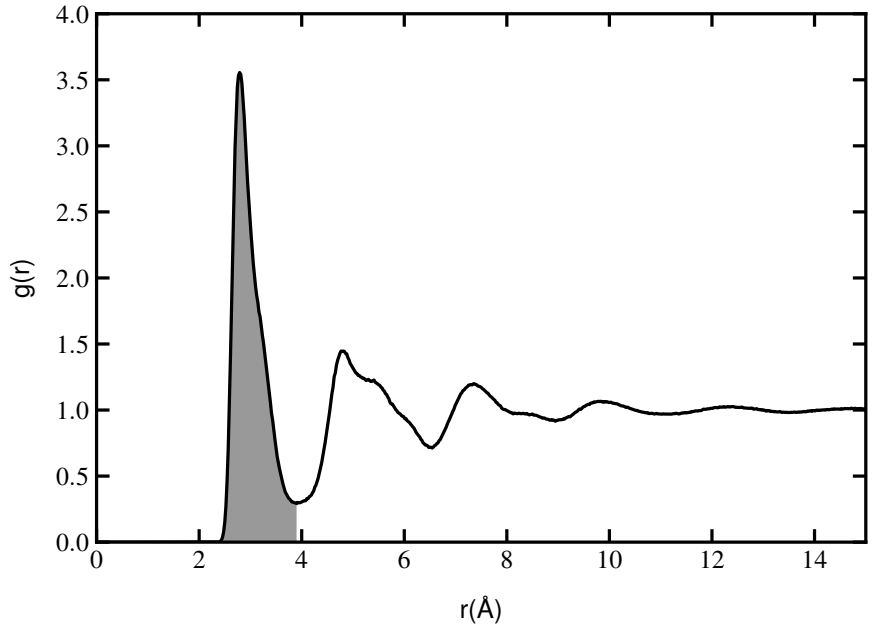

Figure 2.5: A representative pair distribution function of a glassy sample obtained with an MD simulation. The shaded area under the first main peak corresponds to the average number of nearest neighbors of the sample.

$$N_{\text{coor}} = \rho \int_{r_1}^{r_2} g(r) 4\pi r^2 dr \tag{2.10}$$

Figure 2.5 shows a representative $g(r)$ curve where the area under the first main peak is shaded to indicate the integral of the first main peak.

Other methods to determine the coordination number of a system include the distance cutoff [99] and Voronoi Tesselation methods. To utilize distance cutoff method, a tolerance distance must be defined. A rule of thumb to define the tolerance distance is to use the distance at which the first main peak of the pair distribution function minimizes. After defining the tolerance distance, the atoms that lie within that distance are regarded as the nearest neighbors of an atom. Hence, the coordination number of an atom can easily be obtained by calculating the distances between each and every atom within the system. Figure 2.6 shows a two dimensional representation of distance cutoff method. Voronoi Tesselation method will be covered in the following section.

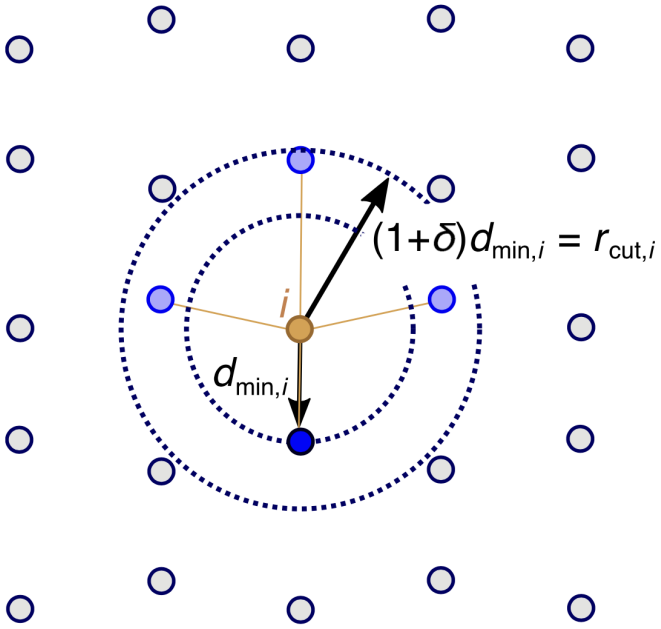

Figure 2.6: The distance cutoff method for determining nearest neighbors. $d_{min,i}$ is the site-specific cutoff distance, δ is the neighbor-finding distance tolerance. All atoms lie within $r_{cut,i} = (1 + \delta)d_{min,i}$ considered as neighbors of the central atom i. Adopted from [99].

2.4 Voronoi Tessellation Analysis

Due to the fact that the MGs lack the long-range order of crystalline structures, their structural analysis is challenging to achieve using the conventional structural identification methods. Voronoi tessellation [100] concept is a fairly simple but convenient method to discover possible structural features that MGs may still exhibit to some degree.

The planar ordinary Voronoi tessellation divides the Euclidean plane into a set of regions, given a set of at least two non-coincident points. To achieve that, every point in the Euclidean plane is assigned to its nearest member in the point set. Regions that are assigned to only a single member form the Voronoi cells. Those regions are collectively exhaustive to the whole Euclidean plane. The points of the Euclidean plane that are assigned to two members contour the boundaries of those regions and are called Voronoi edges. The points at which more than two Voronoi edges meet or, in other words, the points assigned to three members are called Voronoi vertex, see Figure 2.7. An alternative definition for the construction of Voronoi cells also exists in terms of half planes. In this definition, the regions bounded by the Voronoi edges are obtained by constructing bisecting planes between all neighboring members. The points at which bisecting planes intersect are the Voronoi vertex.

The planar ordinary Voronoi tessellation in two dimensions can easily be extended to three dimensions. In the three-dimensional case, the boundaries between the Voronoi regions are called Voronoi facets, and the boundaries of those facets are also called Voronoi edges. The intersection points of Voronoi facets are also known as Voronoi vertices. Constructing Voronoi cells centered on each member will give a polyhedron around each member. After determining every Voronoi cell within the Euclidean space, the topological characteristics of each polyhedron are used to differentiate between them. One of the most frequently used methods to distinguish different types of Voronoi cells is to use the number of faces each cell has. In this strategy, each cell with f number of faces is given an index listing the number of faces $n_3, n_4, n_5, \ldots, n_j$ having $3, 4, 5, \ldots, j$ edges, where $\sum_{k=i}^{j} n_k = f$ [101].

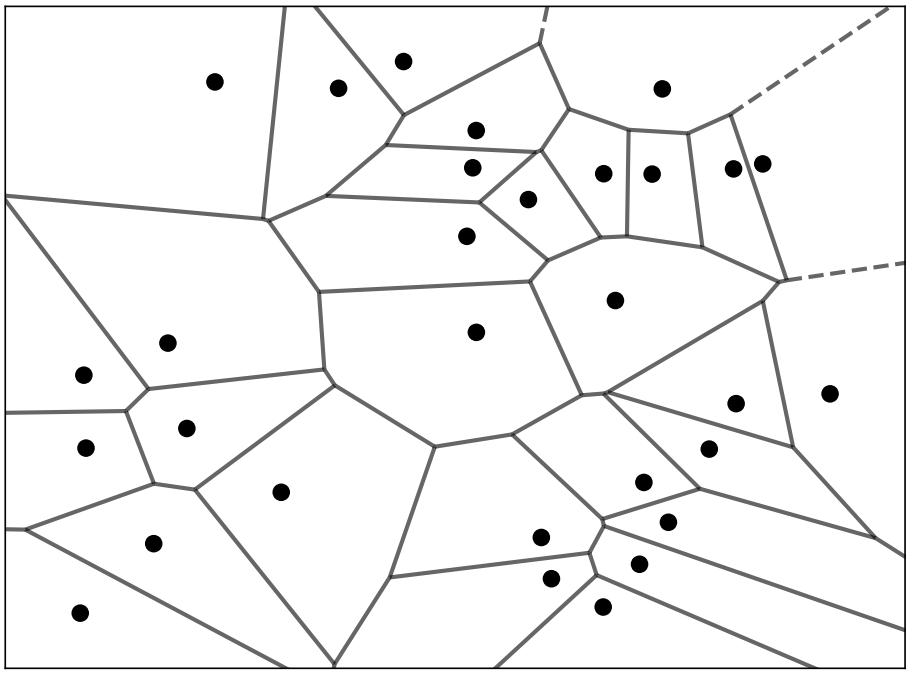

Figure 2.7: A representative two dimensional analogue of the planar ordinary Voronoi tessellation where filled dots denote the cell centers, and the solid lines are the Voronoi edges.

The points in mind are considered identical in size in ordinary Voronoi tessellation. However, this is not the case for most applications, including determining local structure characteristics of metallic glasses constituting more than one component. Using ordinary Voronoi tessellation, the boundary of several Voronoi polyhedrons may lie inside the points. This will lead to miscalculations of both polyhedral indexes as well as several auxiliary properties that can be deduced from Voronoi tessellation analysis, including the polyhedral volume and the number of faces each polyhedron has, see Figure 2.8. The radical plane technique proposed by Fischer and Koch [102] solves this problem of misjudgment by positioning the dividing planes between the members to the locus of points where the tangent lengths of the two members are equal. Park and Shibutani [103] have shown that using the ordinary Voronoi tessellation technique may result in more than 60% difference in some properties of binary and ternary MGs compared to radical Voronoi tessellation. Thus, the utilization of radical Voronoi tessellation dramatically improves the effectiveness of the Voronoi technique, especially for alloys with more than one component.

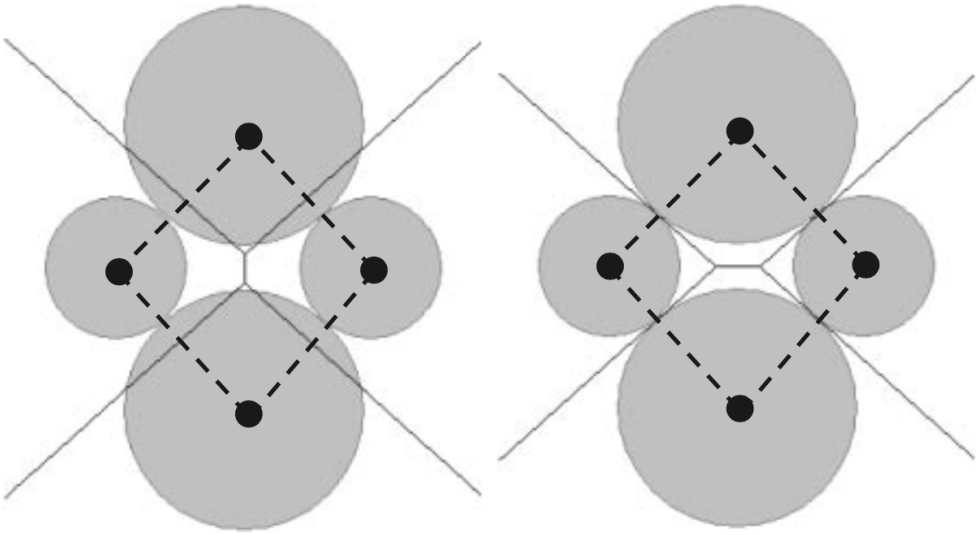

(a) (b)

Figure 2.8: Two dimensional representation of (a) planar ordinary Voronoi tessellation and (b) the radical plane Voronoi tessellation. The number of faces, the Voronoi cell index and the positions of Voronoi edges are falsely calculated in the planar ordinary Voronoi tessellation [103].

The Voronoi polyhedrons are mainly classified according to their Voronoi indices. Although there are many approaches in the literature for categorizing Voronoi indices, the scheme in Table 2.1 will be used throughout this study. The scheme consists of only those frequently observed within MGs: perfect-icosahedron, distorted-icosahedron, crystal-like and mixed cells.

Since each Voronoi facet must have one and only one neighboring member related to the member being considered, the number of Voronoi facets an atom has will be equal to that atom's coordination number (CN). This is a quite simple and parameter-less way to determine the CN of an atom under the condition that the Voronoi structure is determined. Therefore, the summation $\sum_i n_i$ gives a specific atom's CN.

Table 2.1: The classification of Voronoi index, where $x = 1, 2, 3, 4, 5, 6$ [104].

Type Name	**Voronoi Indices**
Perfect-Icosahedron	$\langle 0, 0, 12, 0 \rangle$
Distorted-Icosahedron	$\langle 0, 1, 10, x \rangle$ $\langle 0, 0, 10, x \rangle$ $\langle 0, 2, 8, x \rangle$
Crystal-like	$\langle 0, 4, 4, x \rangle$ $\langle 0, 5, 2, x \rangle$
Mixed	$\langle 0, 3, 6, x \rangle$

Figure 2.9 shows schematics of solute-centered perfect-Icosahedron and several distorted-icosahedron cells for a binary system. Figure 2.9a is the perfect-icosahedron, whereas the rest of Figure 2.9 are the distorted-icosahedra. Those Voronoi cells are the most abundant in MG alloys.

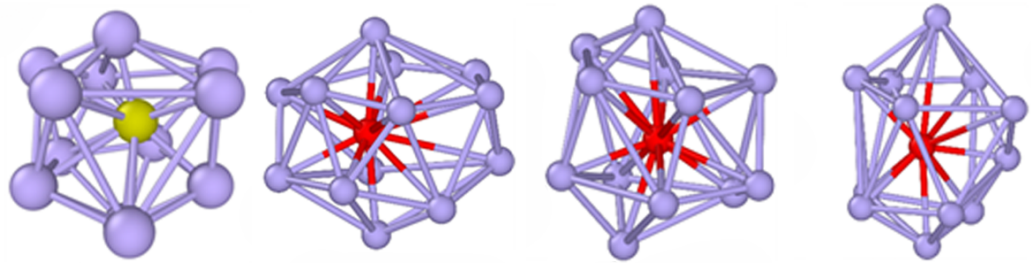

(a) $\langle 0, 0, 12, 0 \rangle$ (b) $\langle 0, 1, 10, 2 \rangle$ (c) $\langle 0, 0, 10, 2 \rangle$ (d) $\langle 0, 2, 8, 2 \rangle$

Figure 2.9: Several schematic Voronoi cells. Perfect-Icosahedron (a) $\langle 0, 0, 12, 0 \rangle$, and distorted-Icosahedron (b) $\langle 0, 1, 10, 2 \rangle$, (c) $\langle 0, 0, 10, 2 \rangle$, (d) $\langle 0, 2, 8, 2 \rangle$. Adopted from [105].

2.5 Honeycutt-Andersen Analysis

One of the most widely used multi-body correlation analysis methods is the Honeycutt-Andersen (H-A) method [106]. It characterizes the local chemistry of a system through the nominal composition and nearest neighbors of each atom. This method is especially beneficial for amorphous materials and liquids since the short-ranged local structures of those materials affect the overall properties the most.

In the H-A method, a parameter containing four integers, *ijkl*, is employed to define the chemical SRO of an atomic pair. The first index of the H-A parameter designates whether the pair is bonded or not. It will be 1 if the pair is bonded and 2 otherwise. The second and third indices indicate the number of nearest neighbors commonly shared by the pair and the bonds among those shared neighbors. The first three indices of the H-A parameter do not contain any information about the geometrical features of a pair. An additional index along with those three, l, was employed to distinguish non-identical pairs when their nearest neighbor and bond counts are the same.

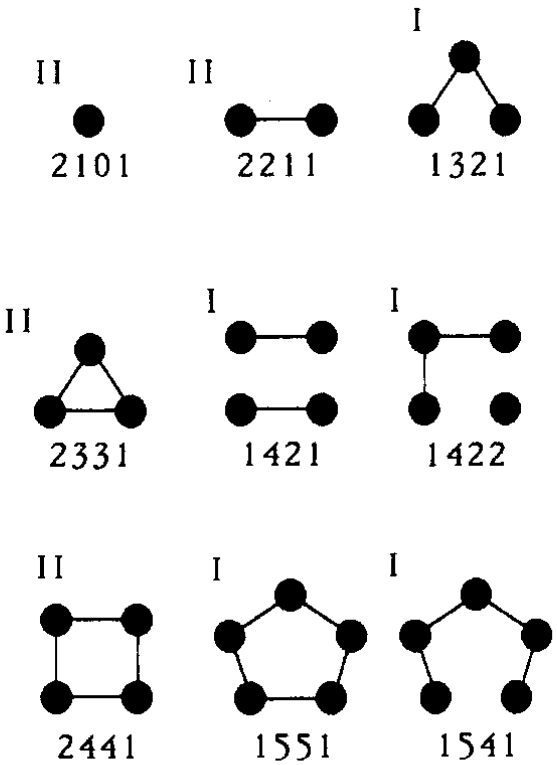

Figure 2.10: Common Honeycutt-Andersen diagrams. Adopted from [106].

Table 2.2: The classification of Honeycutt-Andersen index, where $x = 1, 2, 3, 4, 5, 6$. Along with the crystalline phases (*bcc*, *fcc*, and *hcp*) perfect- and distorted-icosahedron types are explicitly defined.

Type Name	**H-A Indices**
Perfect-Icosahedron	1551
Distorted-Icosahedron	1431
	1541
Body-Centered Cubic (*bcc*)	1441
	1661
Face-Centered Cubic (*fcc*)	1421
Hexagonal Close-Packed (*hcp*)	1422

In Figure 2.10, diagrams are distinguished as type I if the atoms in the pair of interest are directly connected and type II otherwise [106]. Possible types of pairs of atoms for the H-A index are given in Figure 2.10. Several H-A indexes were given in Table 2.2, where 1551 represents perfect-ICO, while 1431 and 1541 represent distorted icosahedra. The *fcc* and *hcp* structures have the H-A indices of 1421 and 1422, respectively, and indices 1661 and 1441 represent *bcc* structures.

2.6 Warren-Cowley Parameter

The local chemical inhomogeneities can be analyzed through *Warren-Cowley* (W-C) [107, 108] parameter. It quantifies the short-range deviations from the chemical composition of the system and gives insights into the degree of chemical SRO. It is defined as:

$$\alpha_{\mathrm{AB}} = 1 - \frac{Z_{\mathrm{AB}}}{x_{\mathrm{B}} Z_{\mathrm{A}}} \tag{2.11}$$

where Z_{AB} is the number of neighboring type B atoms around type A atom, Z_A is the total coordination number of type A atom, and x_B is the nominal composition of type B. When measured around type B atoms, the Warren-Cowley parameter ranges between $\frac{x_B-1}{x_B}$ ($\frac{x_A-1}{x_A}$, when measured around type A atoms) and 1. A value of 0 suggests a random distribution, whereas a positive and negative value corresponds to a tendency for like and dislike pairs in the coordination shell, respectively.

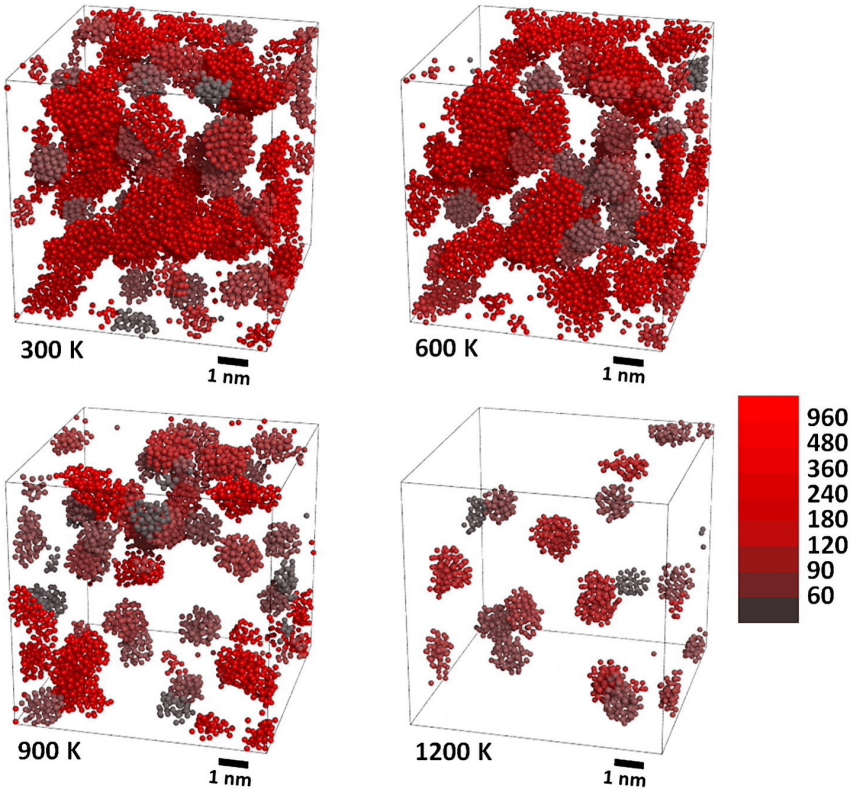

Figure 2.11: Spatial distribution and sizes of pure aluminum clusters of $Al_{90}Tb_{10}$ at 300 K, 600 K, 900 K, and 1200 K. Adopted from [109].

The tendency for clustering or local order can be decided based on the Warren-Cowley parameter value. Using the Warren-Cowley parameter analysis, Ovun et al. [109] have shown that the degree of Al – Al ordering and the number of pure Al clusters with a Warren-Cowley parameter value of 1 have increased drastically below the glass transition temperature of Al – Tb metallic glasses, indicating the formation of pure Al regions within the alloy, see Figure 2.11.

2.7 Bond Angle Distribution

Bond Angle Distribution (BAD) can analyze the spatial arrangements of bonded atoms within a system. First, each of the bonds between the neighboring triplets must be defined for every atom in the system o determine the distribution. Then, using the length of those bonds, the bond angle formed between the selected center atom and its two neighbors can be calculated using Equation (2.12).

$$\theta_{ijk} = \cos^{-1}\left(\frac{r_{ij}^2 + r_{ik}^2 - r_{jk}^2}{2r_{ij}r_{ik}}\right) \tag{2.12}$$

where r_{ij} and r_{ik} are the lengths of bonds between the center atom, i, and the two neighboring atoms, j and k, respectively. r_{jk} is the distance between the atoms j and k. After obtaining the bond angles between every single triplet within the system, the probability distribution of bonds with respect to angles can be obtained using Equation (2.13).

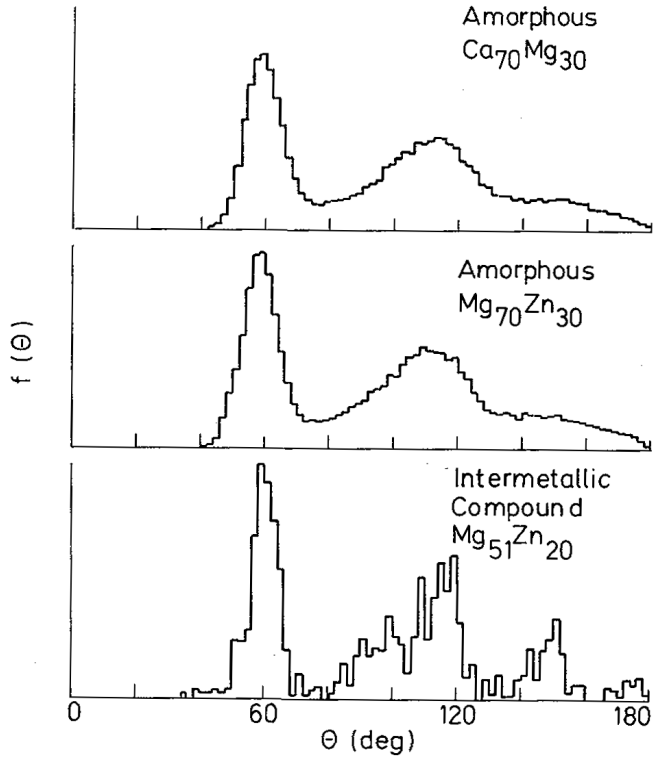

Figure 2.12: Total bond angle distribution functions for amorphous $Ca_{70}Mg_{30}$, amorphous $Mg_{70}Zn_{30}$, and Intermetallic $Mg_{51}Zn_{20}$. Adopted from [110].

$$g(\theta) = \frac{1}{\sum_{i=1}^{N} N_i (N_i - 1)} \sum_{i=1}^{N} \sum_{j=1}^{N_i} \sum_{k=j+1}^{N_i} \delta(\theta - \theta_{ijk}) \tag{2.13}$$

where N_i is the number of nearest neighbors atom i has and θ_{ijk} defined earlier in Equation (2.12). Depending on the material's structure, bond angle distribution plots of crystalline materials will have one or many prominent peaks located at characteristic bond angles. A representative total bong angle distribution function is given in Figure 2.12 for $Ca_{70}Mg_{30}$, $Mg_{70}Zn_{30}$, and $Mg_{51}Zn_{20}$ systems.

2.8 Bond Order Parameter

Differentiating the atoms belonging to the liquid and the possible solid structures is of major interest in both crystallization and amorphization studies. Local structure determination methods, e.g., Bond Angle Distribution, fall short in identifying atoms belonging to liquid-like and solid-like structures. To overcome this difficulty, Steinhardt et al. [111, 112] proposed an efficient algorithm based on spherical harmonics. This algorithm first calculates the complex vector $q_{lm}(i)$ averaged on the number of nearest neighbors of particle i, $N_b(i)$, via Equation (2.14).

$$q_{lm}(i) = \frac{1}{N_b(i)} \sum_{j=1}^{N_b(i)} Y_{lm}(\boldsymbol{r}_{ij}) \tag{2.14}$$

where l is a free integer parameter, $Y_{lm}(\boldsymbol{r}_{ij})$ are the spherical harmonics that depend on the vector $\boldsymbol{r}_{ij}$ between particles i and j. Then, the structural correlation between the particles i and j can be measured using the set of complex vectors q_{6m} and Equation (2.15).

$$S_{ij} = \sum_{m=-6}^{6} q_{6m}(i) q_{6m}^{*}(j) \tag{2.15}$$

The resulting parameter S_{ij} is then used to define two particles i and j as connected or not. Typically, an S_{ij} value greater than 0.5 indicates that two particles are connected. The number of connections a particle has is then used to identify the particle as liquid-like or solid-like. A useful rule of thumb in this analysis is that particles having a number of connections above 6 or 8 are considered solid-like, and particles having fewer connections are considered liquid-like. Bond order parameters (BOP), or Steinhardt order parameters, can be used to further characterize the solid-like particles by grouping them depending on their crystal structures. Depending on the constant l in Equation (2.16), particles can be identified as belonging to a specific structure.

$$q_l(i) = \sqrt{\frac{4\pi}{2l+1} \sum_{m=-l}^{l} |q_{lm}(i)|^2} \tag{2.16}$$

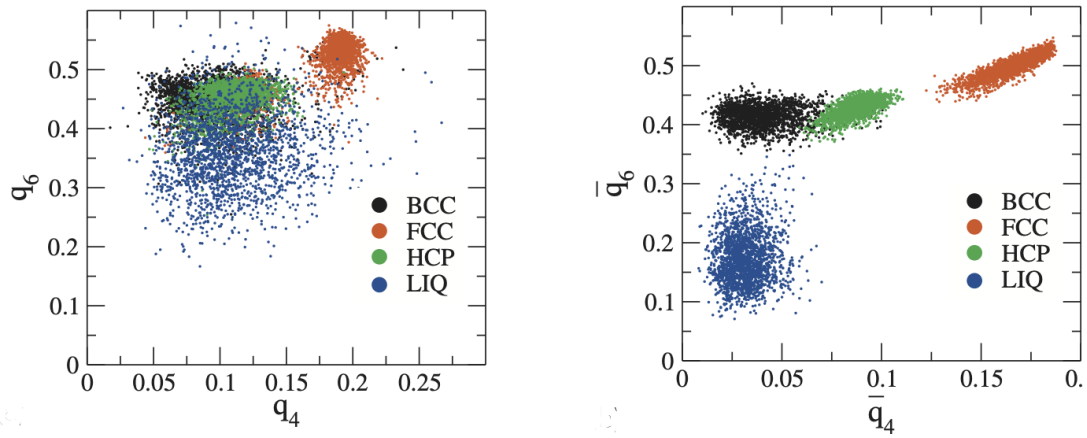

(a) (b)

Figure 2.13: Comparison between the (a) q_6 and q_4 planes and (b) $\overline{q}_6$ and $\overline{q}_4$ for a Lennard- Jones system in liquid and three different crystalline phases. Adopted from [113].

Lechner et al. have shown that averaging complex bond order parameters over the particle itself and its first neighbor shell substantially enhances the accuracy of distinguishing different types of crystal structures. They proposed averaging the local bond order parameters via Equation (2.17)

$$\overline{q}_l(i) = \sqrt{\frac{4\pi}{2l+1} \sum_{m=-l}^{l} |\overline{q}_{lm}(i)|^2} \tag{2.17}$$

where;

$$\overline{q}_{lm}(i) = \frac{1}{\tilde{N}_b(i)} \sum_{k=1}^{\tilde{N}_b(i)} q_{lm}(k) \tag{2.18}$$

The modification Lechner et al. proposed on bond order parameters greatly improves the accuracy of the method to differentiate different crystal structures. Their modification takes the second nearest neighbors into account for the calculations. They demonstrated the effectiveness of the modification by simulating two systems of particles, one with utilizing a Gaussian core potential and the other one with Lennard-Jones. Figure 2.13a shows the unmodified bond order parameter analysis results whereas, Figure 2.13b shows the averaged/modified bond order parameter analysis. The pronounced distinction between various crystal structures and liquid structure is evident.

CHAPTER 3

LOCAL STRUCTURE OF THE Al-Sm MARGINAL METALLIC GLASSES AND LIQUIDS

3.1 Introduction

After the discovery of the first amorphous metallic glass (MG) ($Au_{75}Si_{25}$) by Duwez et al. in 1960 [1], there has been an increasing interest in this new family of materials mainly due to their remarkable properties such as high mechanical strength and hardness, significant elastic limits, better thermal stabilities, improved soft magnetic properties, high corrosion and wear resistance [114, 115, 116, 117, 118, 19, 119, 120, 121, 22, 122]. This interest resulted in a wide range of engineering applications, from magnets with high energy products and implants to sporting goods and electronic devices [22]. The attractive properties and the wide range of application areas of MGs stem from the fact that the MGs have unusual non-crystalline random atomic configurations even at room temperature. Glasses are obtained by quenching their high-temperature melts. Since metallic materials are known to crystallize upon cooling down below their melting temperature quickly, (T_m) or liquidus temperature (T_l), to retain the amorphous structure of the liquid metal at room temperature, very high cooling rates are required to suppress the crystallization behavior. High cooling rates up to $10^5 - 10^6\ \mathrm{K\,s^{-1}}$ were used by Duwez et al. to obtain the first MG [1]. However, by stabilizing the metallic liquid in the temperature range between the T_l and the glass-forming (T_g) temperatures by altering the composition and carefully selecting the constituting elements, MGs can be obtained at room temperature using relatively slow cooling rates [123].

Al-based MGs are lightweight and exhibit high specific strength. Because these properties are essential for structural applications, their research has been much of interest recently. The first examples of Al-based MGs were noticed in $Al-(Fe,Co,Ni)-B$ systems in the early '80s [33]. However, it was not until the late '80s that the first relatively ductile Al-based MGs surfaced [35, 124]. Al-Rare Earth (RE) alloys show both good ductility with very high strength values comparable to those of steel, the research on various Al-based RE-containing MGs was presented to the literature [125, 126, 127, 128, 98, 96, 109, 129]. Even though Inoue's criteria for MG formation [18, 19] requires at least three elements, several binary $Al-RE$ systems were observed to have glass-forming abilities (GFA). Also, for most of the glass-forming alloys, the go-to composition range for best GFA is near-eutectic; however, Al-based systems can form glasses in off-eutectic compositions. Therefore, the structures of Al-based MGs are of significant interest for further investigations, and several Al-based systems studied by Inoue et al. in which $Al-Sm$ have the widest composition range (from 8 to 16 at. % Sm) for the glass formation [39]. The technical data for elements Al and Sm can be seen in Table 3.1. The properties of MGs mentioned strongly depend on the system's structure and evolution during the formation process. Thus, the resulting properties of MGs are susceptible to the production route that can alter the local structures [130, 131]. X-Ray and neutron diffraction are widely used to investigate the structures of MGs. The resulting structure factors of Al-based MGs have a unique feature observed at lower reciprocal space called *pre-peak* that should correspond to specific medium-range correlations in real space. The origin of the *pre-peak* is attributed to the well-separated solutes forming a sublattice and to the topological ordering of RE atoms [132].

$Al-RE$ marginal glass-forming systems have been studied in Kalay's research group for quite some time. Much emphasis has been given to $Al-Tb$, and $Al-Sm$ systems, and the following summarizes the significant achievements. The Bright-field (BF-TEM) images and selected area electron diffraction (SAED) patterns confirm the fully amorphous nature of the matrix of melt-spun as-quenched $Al_{90}Tb_{10}$ ribbons, as shown in Figure 3.1.

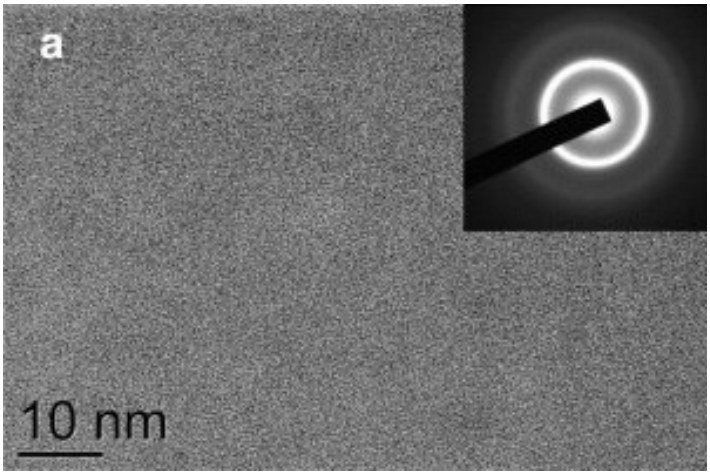

Figure 3.1: BF-TEM image of melt-spun as-quenched $Al_{90}Tb_{10}$ alloy. Inset shows the SAED pattern of the matrix. Adopted from [125].

Further, isochronal differential scanning calorimetry (DSC) experiments have shown that the first devitrification event is the nanocrystallization of the *fcc*-Al phase [125]. As explained in Section 1.1.3, the expected abundance of a glass transition signal is also evident in the DSC curve, see Figure 3.2. Additionally, the inspection of the devitrification products has been made through TEM studies coupled with XRD. The samples were prepared by interrupting the $220\,^{\circ}\mathrm{C}$ isothermal DSC experiments at the points shown in Figure 3.2 (b) and (c) [125].

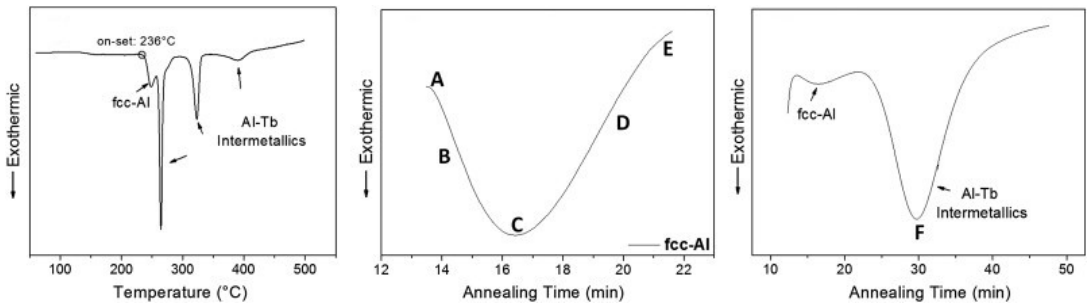

Figure 3.2: (a) Isochronal DSC curve at $40\,^{\circ}\mathrm{C}/\,\mathrm{min}$ heating rate. Isothermal DSC curves indicate (b) the *fcc*-Al crystallization and (c) the overall first and second exothermic events. The interception points for TEM and XRD are marked as A, B, C, D, E, and F. Adopted from [125].

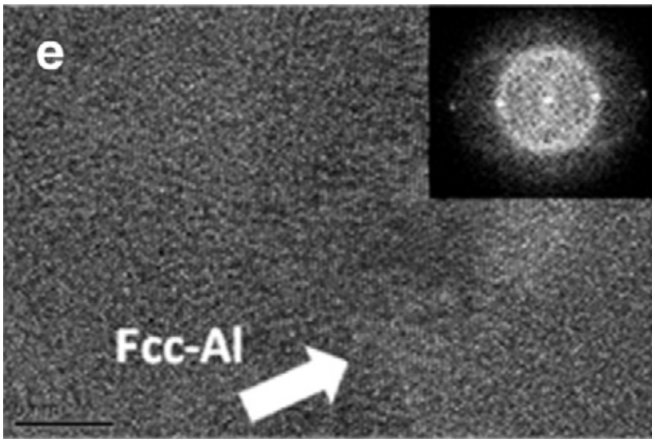

Figure 3.3: HRTEM image of melt-spun $Al_{90}Tb_{10}$ sample obtained by interrupting the annealing experiment at $220\,^{\circ}\mathrm{C}$ just after the initial crystallization event. Inset shows the corresponding FFT pattern. Adopted from [125].

High-Resolution Transmission Electron Microscopy (HRTEM) analysis revealed the formation of an anomalously high number of *fcc*-Al nanocrystals in the order of 10^{21} per cubic meter, see Figure 3.3. A possible structural inhomogeneity in the system is believed to cause highly populated nanocrystals to form [125]. The evolution of the local atomic configuration of $Al_{91}Tb_9$ was investigated using Voronoi tessellation and Warren-Cowley parameters by using an interatomic potential developed, as shown in Figure 3.4, using the Inverse Monte Carlo method [109].

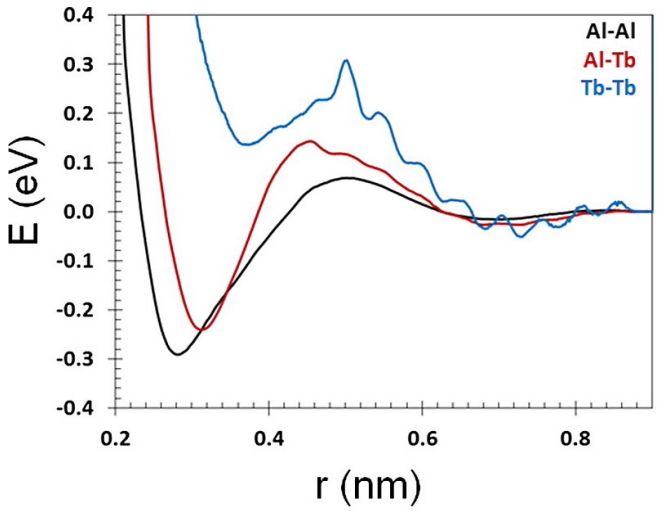

Figure 3.4: The interatomic pair potential developed using the Inverse Monte Carlo algorithm for the $Al_{91}Tb_9$ system. Adopted from [109].

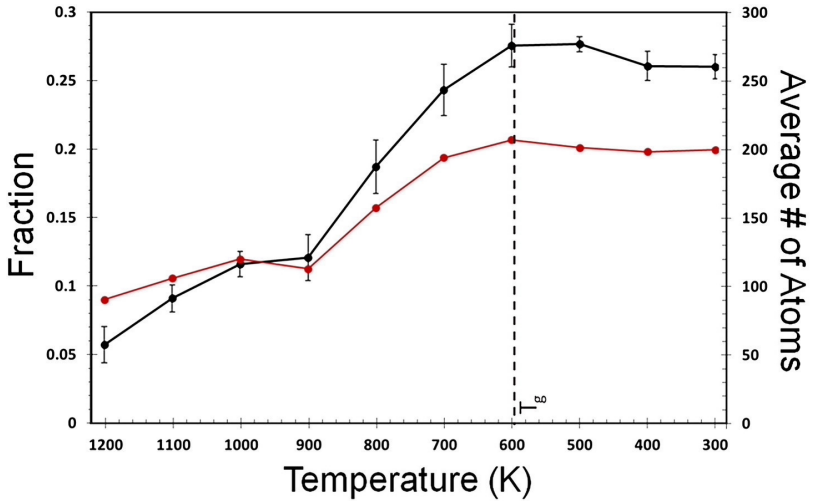

Figure 3.5: The fraction of aluminum atoms belonging to pure aluminum clusters (solid black curve) and the average number of atoms each cluster has (red curve). Adopted from [109].

The system was studied from liquid to glassy state, and the population of Al-centered icosahedral-like clusters increased during cooling. It is believed that they are the ones that inhibit crystallization during vitrification. Warren-Cowley studies have shown the presence of highly pure isolated Al regions beyond the first shell, see Figure 3.5. Kalay's group also found that the network of RE-centered clusters and pure Al atoms in the system has medium-range order (MRO), resulting in the pre-peak in X-ray studies. This study shows that the molten liquid is not as homogeneous as expected and has Al-rich and Al-depleted regions [130]. The role of amorphous precursors in phase selection was investigated using $Al_{90}Tb_{10}$ alloys produced by melt-spinning and magnetron sputtering. The study detected that thin-films and melt-spun ribbons having the same composition have entirely different devitrification paths, even having the same total structure factors as seen in Figure 3.6 [130]. *In-situ* XRD experiments have shown that while *fcc*-Al is the initial crystallization product for both samples, the second crystallization products, and their morphologies and densities are entirely different. The ribbon crystallizes into a metastable hexagonal phase before transforming into a similar cubic phase seen on a thin-film sample, see Figure 3.7 [130].

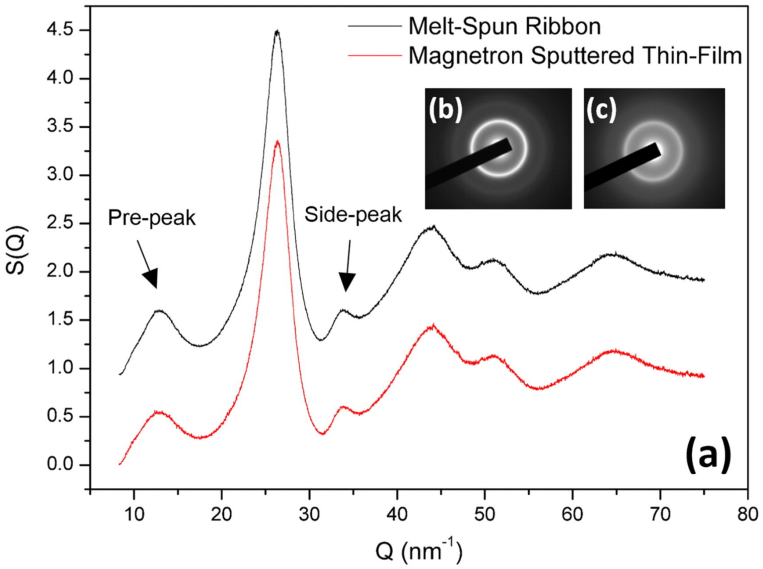

Figure 3.6: (a) X-ray structure factors (S(Q)) of melt-spun ribbon and magnetron sputtered thin-film samples of $Al_{90}Tb_{10}$ at room temperature. Corresponding SAED patterns were given as insets (b) and (c) for ribbon and thin-film samples, respectively. Adopted from [130].

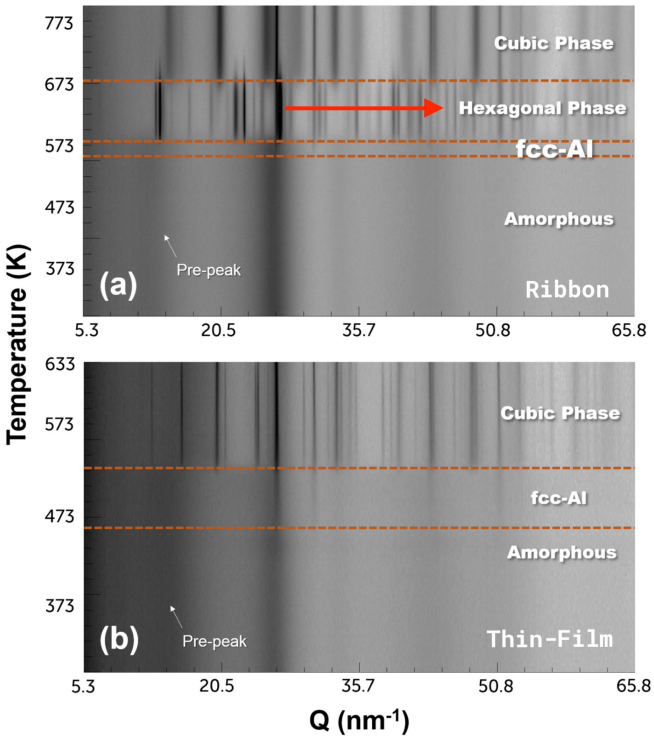

Figure 3.7: *In-situ* X-ray diffraction results represented as 2D area plots for (a) melt-spun ribbon, and (b) magnetron-sputtered thin-film $Al_{90}Tb_{10}$. Adopted from [130].

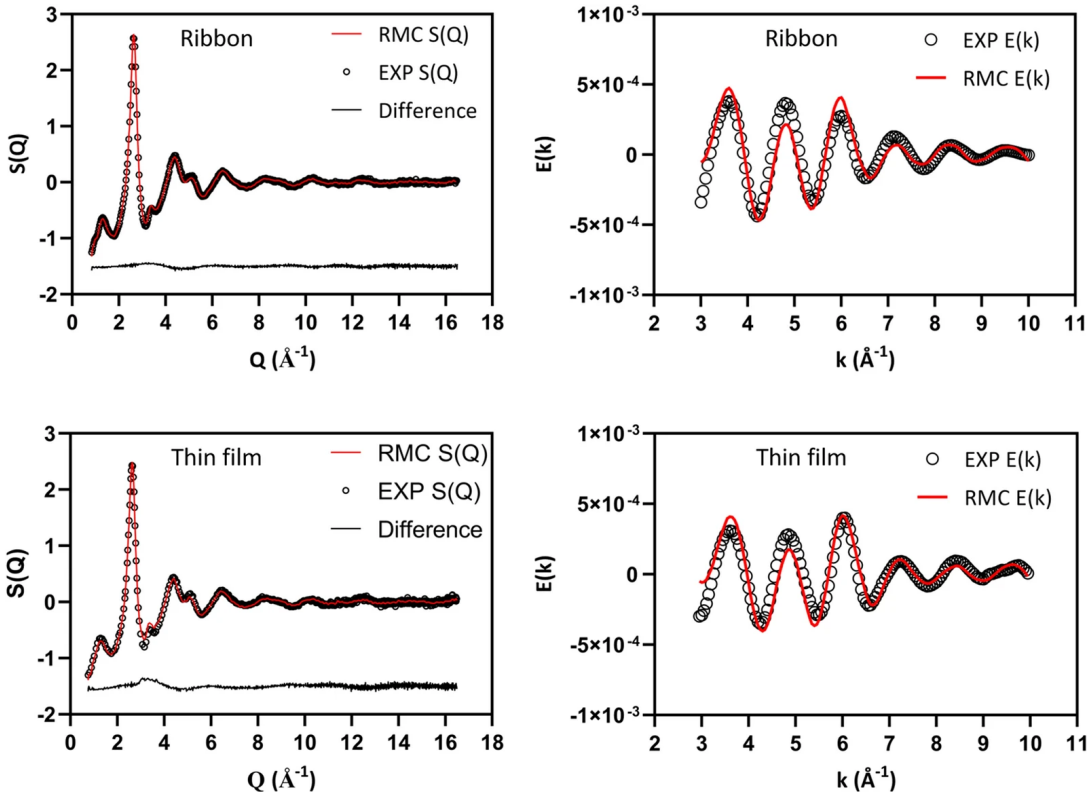

Figure 3.8: (a) Total X-ray structure factor experimental and RMC fit for ribbon, (b) EXAFS data and RMC fit for ribbon, (c) total X-ray structure factor experimental and RMC fit for thin-film, and (d) EXAFS data and RMC fit for thin film. Adopted from [131].

The pre-peak observed in the *in-situ* XRD patterns of the ribbon sample was also absent for the thin film. The metastable hexagonal structure of the ribbon is believed to have originated from the Al-depleted regions of the molten structure. Next, HEXRD and XAFS-constrained Reverse Monte Carlo studies were conducted on Al−Tb ribbon and thin films to resolve the different devitrifications paths experienced on samples having the same compositions yet other precursors. The fitting results for RMC are shown in Figure 3.8. The results have shown in Figure 3.9 that the ribbon sample forms larger Al-centered *fcc*-like and ICO-like clusters, and a higher number is connected as network clusters. They concluded as the differences in the amounts of *fcc*-like and ICO-like clusters are the main reasons for different devitrification paths & nanocrystal morphologies.

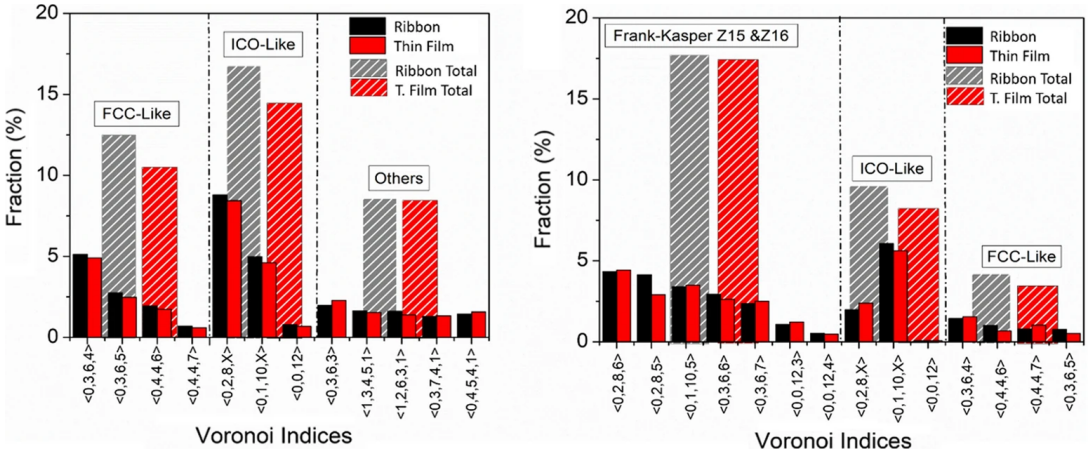

Figure 3.9: The most populated Voronoi cells of ribbon and thin-film $Al_{90}Tb_{10}$ are categorized under the structures they resemble for (e) Al centered and (f) Tb centered atoms. Adopted from [131].

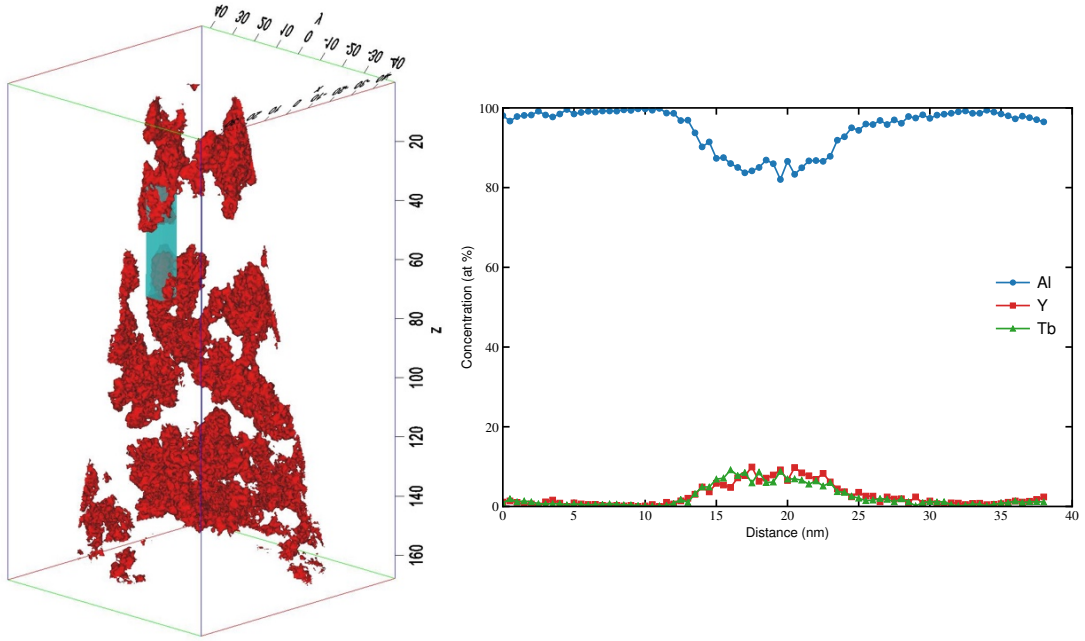

Figure 3.10: One-dimensional concentration profile of the selected region-of-interest (ROI) in $95\,\%$ Al isosurface of $Al_{90}Y_5Tb_5$ system. Adopted from [133].

The effects of short-range chemical order in ternary marginal glass-forming systems on the crystallization pathway have been investigated, as well. The DSC studies showed that $Al_{90}Sm_5Tb_5$ alloy lacks the exothermic reaction that exclusively belongs to *fcc*-Al formation. Contrary to the $Al_{90}Y_5Tb_5$ system, *fcc*-Al nanocrystals form simultaneously with one or more intermetallic phases. Further atom probe tomography (APT) studies revealed that the nanocrystals were almost pure Al while the regions in between have Al concentrations as low as $80\,\%$, as shown in Figure 3.10. This study has shown that RE element addition alters the kinetics and the devitrification behavior of Al-RE systems [133].

One of the most promising ways of studying MGs' local structures is through computer simulations. Especially molecular dynamics (MD) method allows researchers to investigate the structural evolution of a system thoroughly. In this study, MD simulations are employed to analyze the local structure of an Al – RE system. The structural evolution during rapid cooling is inspected using pair distribution function (PDF), structure factor, bond angle distribution, Voronoi, and Honeycutt-Andersen analyses.

Table 3.1: Atomic and physical properties of elements Al and Sm.

	Aluminum (Al)	**Samarium (Sm)**
Atomic Number	13	62
Atomic Weight [136]	26.982	150.36
Electron Configuration	[Ne] $3s^2 3p^1$	[Xe] $6s^2 4f^6$
Electronegativity	1.61	1.17
Valence	3	3

3.2 Methods and Models

MD simulations are performed using Large-scale Atomic/Molecular Massively Parallel Simulator (*LAMMPS*) [82, 134, 83] code by employing a semi-empirical potential in the Finnis-Sinclair form for the force and energy calculations. [135] In the development of this potential lattice, parameters and formation energies of Al-rich crystalline compounds with Sm contents around 10% and the structure of liquid $Al_{90}Sm_{10}$ have been included. The resulting potential is shown to satisfactorily reproduce both a glassy structure upon rapid cooling and a liquid structure at high temperatures in agreement with *ab-initio* MD simulations [135].

An $Al_{90}Sm_{10}$ system consisting of 32,000 atoms is used in MD simulations. The initial structure is arranged on a face-centered cubic (fcc) lattice with $20 \times 20 \times 20$ unit cells. All simulations are conducted under the constant number of atoms, pressure, and temperature (NPT) ensemble where the temperature and pressure are controlled via Nosé–Hoover thermostat and barostat, respectively [137, 138]. The Velocity-Verlet is used as the time integrator for the equations of motion. The mean pressure was nominally maintained at $0\,\mathrm{GPa}$. A constant timestep of $1.0\,\mathrm{fs}$ is used throughout the study. The liquid sample is initially held at $2300\,\mathrm{K}$ for $200\,\mathrm{ps}$ to melt and subsequently equilibrate the liquid structure before rapid cooling. This temperature is significantly above the liquid-glass transition temperature of the alloy determined during the potential development [135]. Then, the liquid is continuously cooled down to $300\,\mathrm{K}$ with a constant cooling rate of $10^{10}\,\mathrm{K\,s^{-1}}$, during which representative structures were obtained at each $200\,\mathrm{K}$ intervals. To eliminate the effect of atomic thermal

motions, the structural and chemical orders in the samples are averaged over $200\,\mathrm{ps}$, which is sufficient to obtain the convergent results for the structural and physical properties studied in this paper.

At every $200\,\mathrm{K}$ interval, PDFs and structure factors were obtained. The structure factors, S(Q), of all samples are obtained by implementing the *Faber-Ziman* formalism [95] seen below as Equation (3.1):

$$S(Q) = \omega_{\mathrm{Al-Al}} S_{\mathrm{Al-Al}}(Q) + \omega_{\mathrm{Al-Sm}} S_{\mathrm{Al-Sm}}(Q) + \omega_{\mathrm{Sm-Sm}} S_{\mathrm{Sm-Sm}}(Q) \tag{3.1}$$

The weight factors ($\omega_{\mathrm{Al-Al}}$, $\omega_{\mathrm{Al-Sm}}$, and $\omega_{\mathrm{Sm-Sm}}$) are determined by the composition of the two species (c_{Al} and c_{Sm}) and the Q-dependent atomic scattering factors ($f_{\mathrm{Al}}(Q)$ and $f_{\mathrm{Sm}}(Q)$) via Equation (3.2) [139].

$$\begin{aligned}
\omega_{\mathrm{AlAl}} &= \frac{c_{\mathrm{Al}}^2 f_{\mathrm{Al}}^2(Q)}{\left[c_{\mathrm{Al}} f_{\mathrm{Al}}(Q) + c_{\mathrm{Sm}} f_{\mathrm{Sm}}(Q)\right]^2} \\
\omega_{\mathrm{AlSm}} &= \frac{2 c_{\mathrm{Al}} c_{\mathrm{Sm}} f_{\mathrm{Al}}(Q) f_{\mathrm{Sm}}(Q)}{\left[c_{\mathrm{Al}} f_{\mathrm{Al}}(Q) + c_{\mathrm{Sm}} f_{\mathrm{Sm}}(Q)\right]^2} \\
\omega_{\mathrm{SmSm}} &= \frac{c_{\mathrm{Sm}}^2 f_{\mathrm{Sm}}^2(Q)}{\left[c_{\mathrm{Al}} f_{\mathrm{Al}}(Q) + c_{\mathrm{Sm}} f_{\mathrm{Sm}}(Q)\right]^2}
\end{aligned} \tag{3.2}$$

The partial structure factors, $S_{ij}(Q)$, in Equation (3.1) are obtained by taking the Fourier transform of the corresponding partial-PDFs, $g_{ij}(r)$, as seen in Equation (3.3).

$$S_{ij}(Q) = 1 + 4\pi\rho \int_0^\infty \left[g_{ij}(r) - 1\right] \frac{\sin(Qr)}{r} r dr \tag{3.3}$$

where ρ is the number density of the relevant atom species in the sample. Local structural arrangements in the system are analyzed using the Voronoi tessellation technique. *Voro++* [140] with periodic boundary conditions is utilized to construct radical Voronoi polyhedrons around each atom, where the size of each atom is also taken into consideration, as suggested by Park and Shibutani [103]. *Honeycutt-Andersen* (H-A) [106] analysis is used to analyze the local structures further. The nearest neighbor lists of each atom for H-A analysis are obtained via *Voro++*.

3.3 Results and Discussions

3.3.1 Glass Transition Temperature

In order to determine the glass-transition temperature T_{g} of the $Al_{90}Sm_{10}$ alloy, the created liquid alloy cooled down to $300\,\mathrm{K}$ with a cooling rate of $10^{10}\,\mathrm{K\,s^{-1}}$. The change in the energy during quenching is shown in Figure 3.11. In this figure, the shape of the curve is typical for systems that undergo a glass transition. At low temperatures, the value $E - 3k_bT$ is largely temperature-independent since atomic motions at these temperatures resemble simple harmonic vibration for which the energy term can be written as $E = E_0 + 3k_bT$ where E_0 is the energy at $0\,\mathrm{K}$. At high temperatures, on the other hand, $E - 3k_bT$ strongly depends on temperature. The glass transition temperature divides these two regions. By using this method, T_{g} was obtained as $693\,\mathrm{K}$ from Figure 3.11.

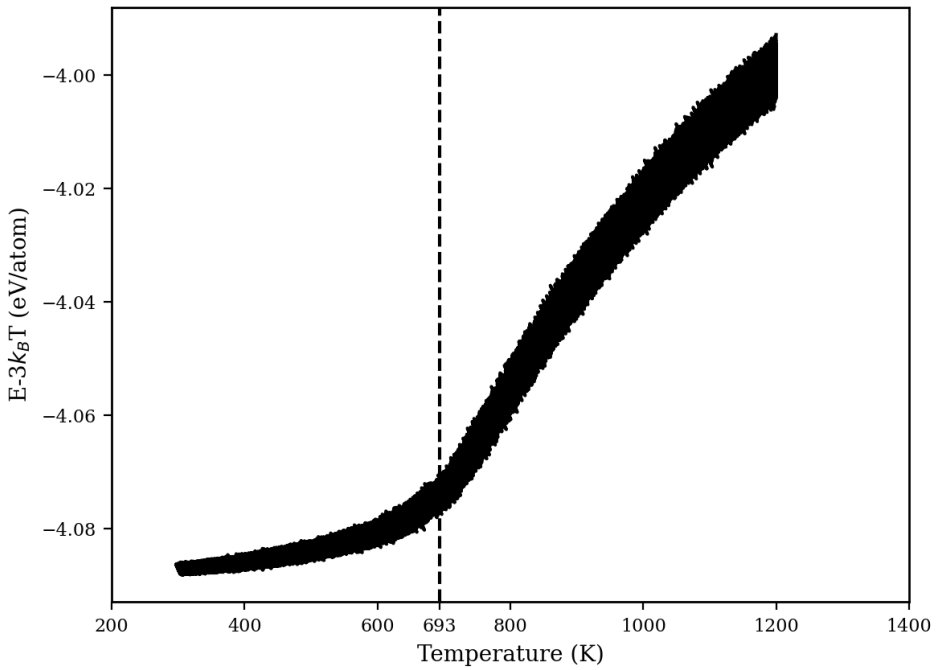

Figure 3.11: Change in energy during cooling the $Al_{90}Sm_{10}$ liquid model from $2300\,\mathrm{K}$ to $300\,\mathrm{K}$ where the cooling rate is $10^{10}\,\mathrm{K\,s^{-1}}$. Only the data between $1200\,\mathrm{K}$ to $300\,\mathrm{K}$ is shown here for clarity.

3.3.2 Mean Squared Displacement Analysis

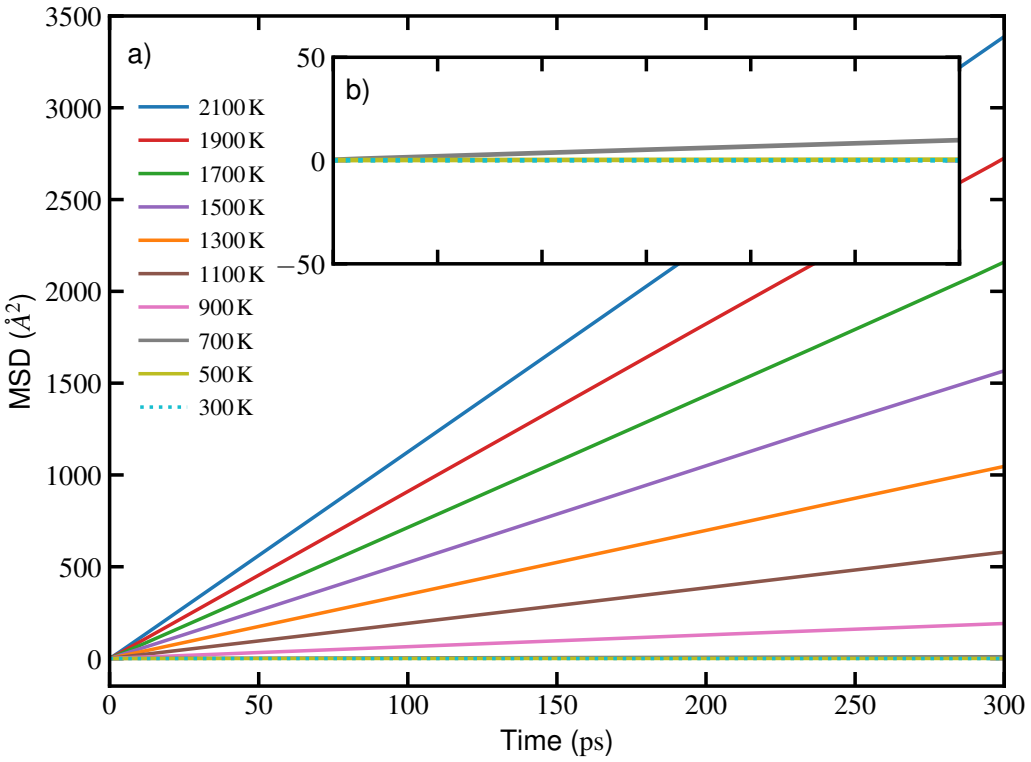

Figure 3.12: Mean square displacement (MSD) for $Al_{90}Sm_{10}$ system (a) from 2100 K to 300 K at 200 K intervals. (b) The inset shows a zoom for MSDs at temperatures 700 K to 300 K at 200 K intervals.

The total mean squared displacements (MSD) of $Al_{90}Sm_{10}$ with the cooling rate as a function of time for a cooling rate of $10^{10}\,\mathrm{K\,s^{-1}}$ are also calculated for 300 ps and represented in Figure 3.12. The inset in Figure 3.12 shows the enlarged part for temperatures 700 K, 500 K, and 300 K. The linear relation between the mean squared displacements and time in Figure 3.12 implies that the structures obtained at that temperatures are successfully equilibrated and suitable for further structural analyses.

3.3.3 Pair Distribution Function

The PDF is one of the essential techniques for analyzing the structures of amorphous solids and liquids. The PDF is defined as

$$g(\boldsymbol{r}) = \frac{1}{N \cdot \rho} \langle \sum_{i}^{N} \sum_{j \neq i}^{N} \delta \left[\boldsymbol{r} - \boldsymbol{r}_{ij} \right] \rangle \tag{3.4}$$

where N is the total number of atoms in the system, ρ is the number density, and $\boldsymbol{r}_{ij}$ is the vector between atoms i and j [141]. Figure 3.13 (a-d) shows the total and partial-PDFs for Al – Al, Al – Sm, and Sm – Sm as a function of temperature between $2100\,\mathrm{K}$ and $300\,\mathrm{K}$, respectively. Each curve has been vertically shifted to increase clarity. An PDF with a sharp first peak followed by broad peaks decreasingly fluctuating around the bulk density is a well-known way to distinguish liquid structures.

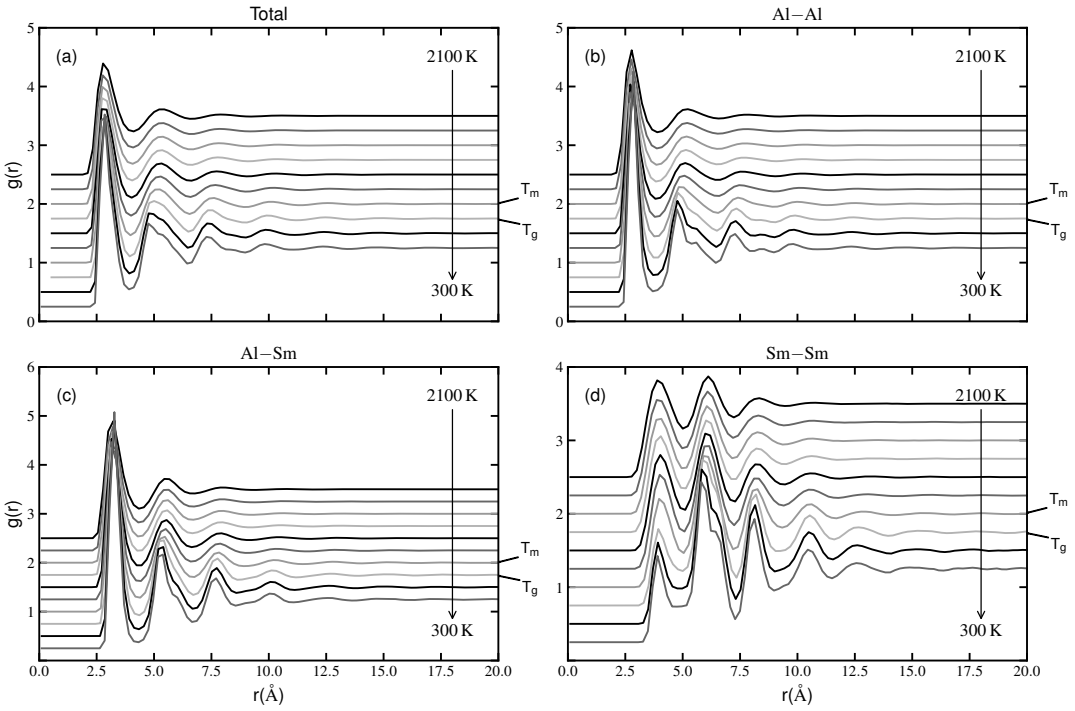

Figure 3.13: (a)-(d) The evolution of the total and partial-PDFs of Al – Al, Al – Sm and Sm – Sm from $2100\,\mathrm{K}$ to $300\,\mathrm{K}$ at $200\,\mathrm{K}$ intervals, respectively. T_m and T_g annotations show the temperatures at which melting and glass transition temperatures are located, respectively.

The top-most curve of Figure 3.13 (a), which corresponds to $2100\,\mathrm{K}$, confirms that the system is in a liquid state at $2100\,\mathrm{K}$. Peak sharpening in PDFs is attributed to structural ordering. The first PDF peak in Figure 3.13 (a) becomes more prominent as the temperature drops along with a decrease in minimum immediately after. This observation indicates an increase in SRO. Similar findings can also be observed in Figure 3.13 (b-d). PDF peaks beyond the first one correspond to configurations further than nearest neighbors and constitute MRO. The presence of second peak splitting as temperature decreases below T_g is a characteristic feature of metallic glasses [142, 143]. Figure 3.13 (a) shows that second peak splitting is evident below T_g. That observation demonstrates an enhancement in MRO and has been subsequently reported in various MG alloy systems. The origin of the second peak splitting on the total PDF is mainly attributed to the high solute-solute correlations and linked to the increase in icosahedral order [144] since increased icosahedral order increases geometric frustration [145]. The second and most intense peak of the Sm-Sm partial-PDF in Figure 3.13 (d) coincides with the shoulder seen in the second peak of the total PDF in Figure 3.13 (a). Our observation shows that the second peak splitting seen in total PDF is due to enhanced Sm−Sm interactions.

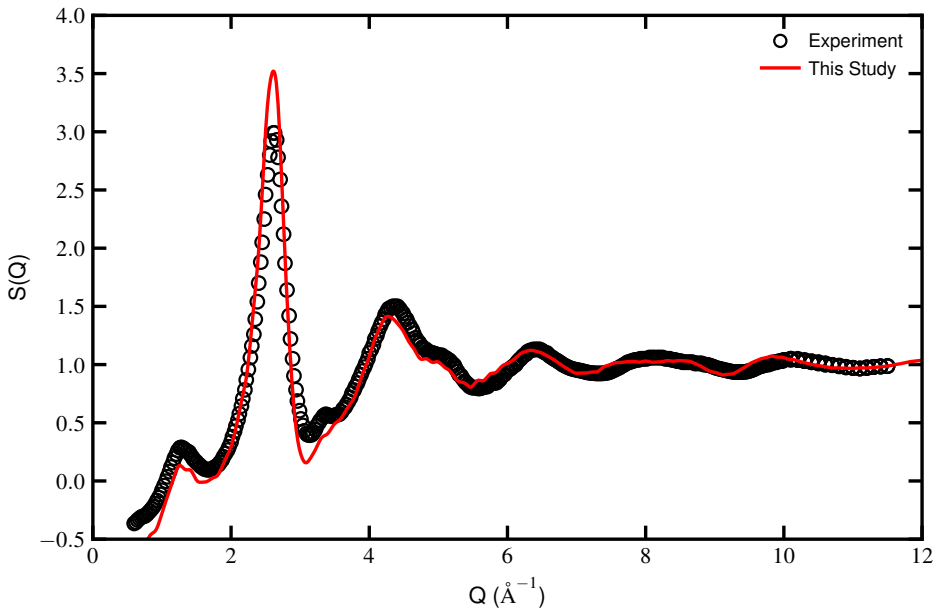

Figure 3.14: The total structure factor of the $Al_{90}Sm_{10}$ model and experimental measurements at room temperature. The experimental data are taken from Ref. [96].

3.3.4 Structure Factor

Figure 3.14 shows the total structure factor of the glass $Al_{90}Sm_{10}$ model at $300\,\mathrm{K}$ calculated with Equation (3.1). via *Faber-Ziman formalism* by using the partial-PDFs. The experimental total structure factor at $300\,\mathrm{K}$ is taken from Ref. [96]. The simulated total structure factor agrees well with the experimental one; even the characteristic pre-peak at $Q \approx 1.3\,\mathrm{\AA}^{-1}$ and side-peak at $Q \approx 3.3\,\mathrm{\AA}^{-1}$ are correctly simulated. This observation also implies that the glassy model created in this study is comparable to the one produced experimentally. Further structural analysis of the developed model is representative of the experimental samples. Due to several magnitudes of difference between the cooling rates of experiments ($\sim 10^5$–$10^6\,\mathrm{K\,s^{-1}}$) [96] and this study ($10^{10}\,\mathrm{K\,s^{-1}}$), the main amorphous peak $Q \approx 2.6\,\mathrm{\AA}^{-1}$ is significantly higher than the experimentally obtained one. The pre-peak seen at $Q \approx 1.3\,\mathrm{\AA}^{-1}$ in Figure 3.14 is commonly attributed to the MRO present in the structure [146, 147], and reported in various other alloy systems [148, 149, 150]. The evolution of the total structure factor with respect to temperature from $2100\,\mathrm{K}$ to $300\,\mathrm{K}$ can be seen in Figure 3.15. During the development of the semi-empirical potential used in this study [135], the liquid-glass transition temperature of the alloy was found as $914\,\mathrm{K}$, and the glass transition temperature was determined as $693\,\mathrm{K}$. Those values were used in any subsequent analysis in this study. Inspecting Figure 3.15, it is seen that the splitting of the second peak was observed below the glass transition temperature (T_g), as expected. However, the pre-peak at the low-Q region at $Q \approx 1.3\,\mathrm{\AA}^{-1}$ seems to persist even above the melting point (T_m) in liquid. That observation implies that the corresponding MRO is also present in the liquid. The liquid's persistent MRO supports the hypothesis that the mechanism that hinders the crystallization of Al-based metallic glasses is due to the MRO, which is inherited from the liquid structure. It is evident that the liquid is not as homogeneously structured as is commonly thought.

3.3.5 Voronoi Tessellation Analysis

Voronoi tessellation is used to classify polyhedral order and analyze the short-range order (SRO) with respect to temperature. Voronoi tessellation analysis is one of the most widely used techniques to study the local structures in metallic glass research.

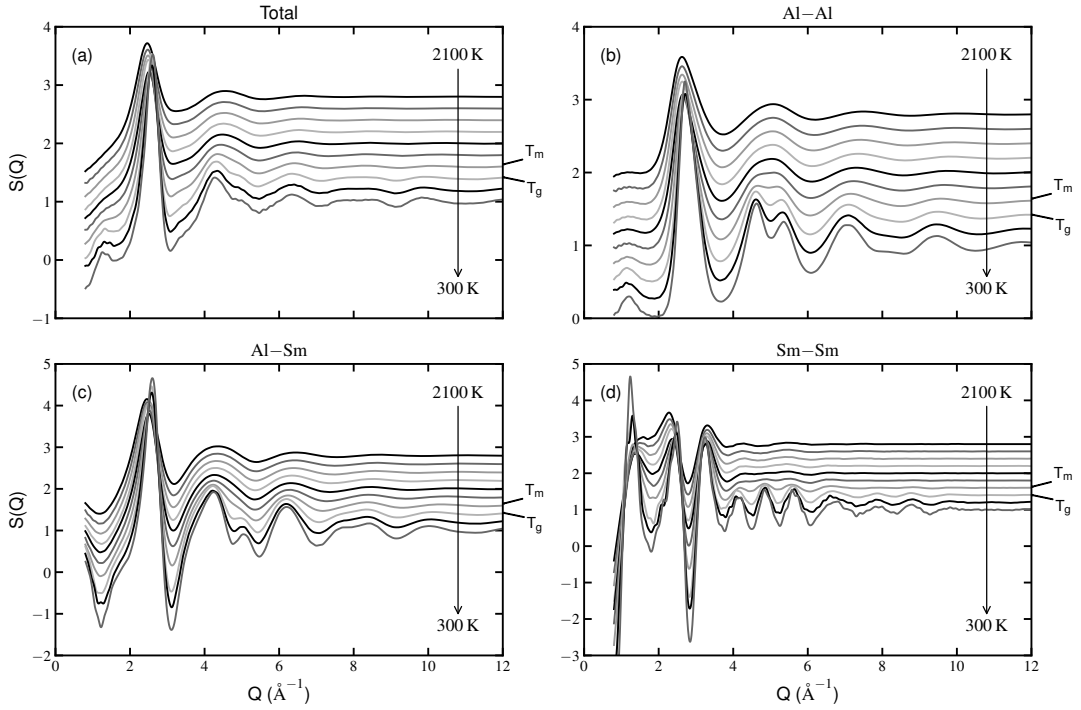

Figure 3.15: The evolution of the total and partial structure factors from $2100\,\mathrm{K}$ to $300\,\mathrm{K}$ at $200\,\mathrm{K}$ intervals for the $Al_{90}Sm_{10}$ model quenched with a cooling rate of $10^{10}\,\mathrm{K\,s^{-1}}$. T_m and T_g annotations show the temperatures at which melting and glass transition temperatures are located, respectively.

In direct or ordinary Voronoi tessellation analysis, a Voronoi cell is attributed to each atom to divide 3-dimensional space by constructing bisecting planes between all neighboring atoms. For the Radical Voronoi Tessellation method used in this study, planes are placed between atoms in proportion to their atomic size [103]. Each Voronoi cell is labeled and classified with an index in the form of $\langle n_3, n_4, n_5, n_6 \rangle$, where n_i is the number of i-edged faces each Voronoi cell has [100]. Since only one atom can be located on each face by definition, the summation $\sum_i n_i$ gives a specific atom's coordination number (CN). Within this classification, $\langle 0, 0, 12, 0 \rangle$ corresponds to perfect-icosahedral structure, whereas Voronoi cells with indices $\langle 0, 1, 10, x \rangle$, $\langle 0, 2, 8, x \rangle$ defined as distorted icosahedra, cells dominated by 4- and 6-edged faces, e.g., $\langle 0, 4, 4, x \rangle$, $\langle 0, 5, 2, x \rangle$, are considered to have crystal-like structures, and cells with 3 quadrangle faces and at least 6 pentagon faces (e.g., $\langle 0, 3, 6, x \rangle$) known as mixed cells, where $x = 1, 2, 3, 4, 5, 6$ [104].

3.3.5.1 Voronoi Index Analysis

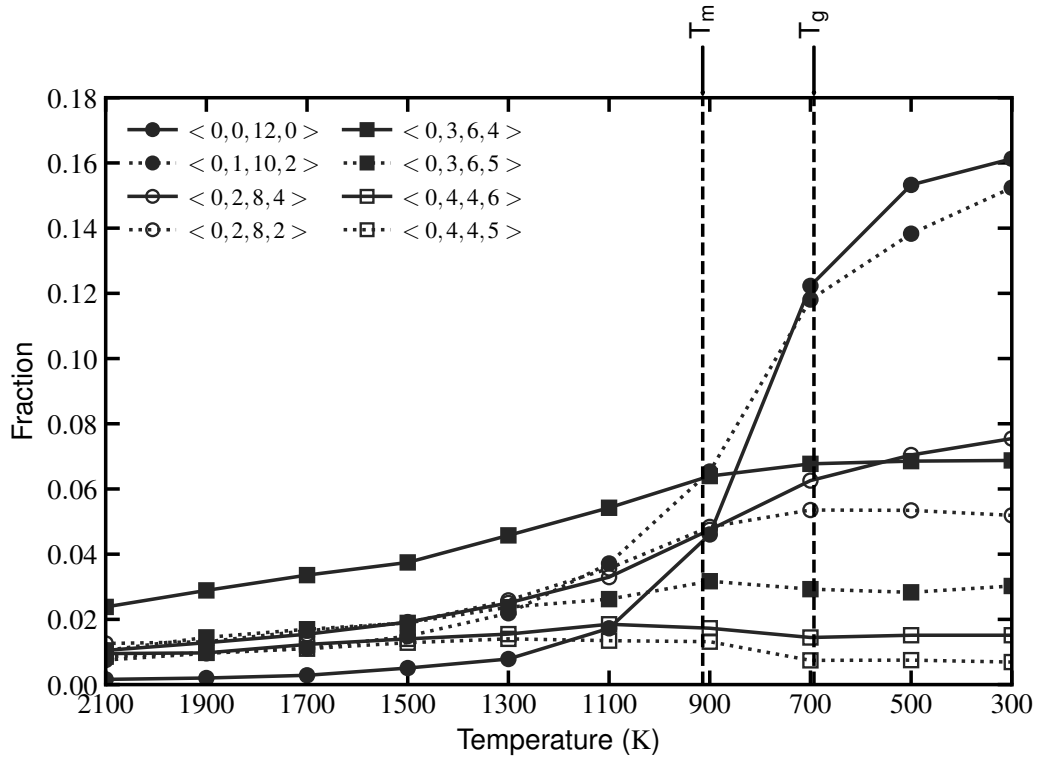

Figure 3.16: The fraction of the eight most populous Al-centered Voronoi indices as a function of temperature for the $Al_{90}Sm_{10}$ model quenched with a cooling rate of $10^{10}\,\mathrm{K\,s^{-1}}$. T_m and T_g annotations show the temperatures at which melting and glass transition temperatures are located, respectively.

The local symmetry in the $Al_{90}Sm_{10}$ alloy is further analyzed using Voronoi tessellation analysis with respect to the center atom of each cell. The temperature dependence of the eight most common Al-centered Voronoi indices is shown in Figure 3.16. It is seen that the fraction of Voronoi indices for the perfect icosahedron $\langle 0, 0, 12, 0\rangle$ and ICO-like $\langle 0, 1, 10, 2\rangle$ cells shows a significant increase at the undercooled region between T_m and T_g. These cells make up the majority of the structure at room temperature. Bokas et al. [151], and Zhang et al. [105] have reported a similar trend in the fraction of ICO-like cells in the undercooled region for the Al−Sm alloys. Their results, however, have not mentioned the fact that those cells were predominantly Al-centered. The fraction of distorted icosahedra cells with indices $\langle 0, 2, 8, 4\rangle$ and

$\langle 0, 2, 8, 2\rangle$ show an exponential increase as the temperature decreases to T_g and their growth slows down. They show the most significant rise ahead of T_g. The mixed type cells with indices $\langle 0, 3, 6, 4\rangle$ and $\langle 0, 3, 6, 5\rangle$ show a stable linear increase in their fractions until T_g, albeit relatively slow compared to icosahedra and distorted icosahedra cells. They stay relatively stable afterward. The remaining Voronoi cells, $\langle 0, 4, 4, 5\rangle$ and $\langle 0, 4, 4, 6\rangle$, are grouped into crystal-like structures, and their fractions remain stable below 2% throughout the cooling process. Earlier, Mishra et al. [152] also saw a significantly low fraction of crystal-like cells at $0\,\mathrm{GPa}$. Our previous HEXRD and EXAFS constrained RMC [131] and Monte Carlo (MC) [109] studies have showed that ICO-like Voronoi cells also dominate the similar Al−Tb configuration at room temperature.

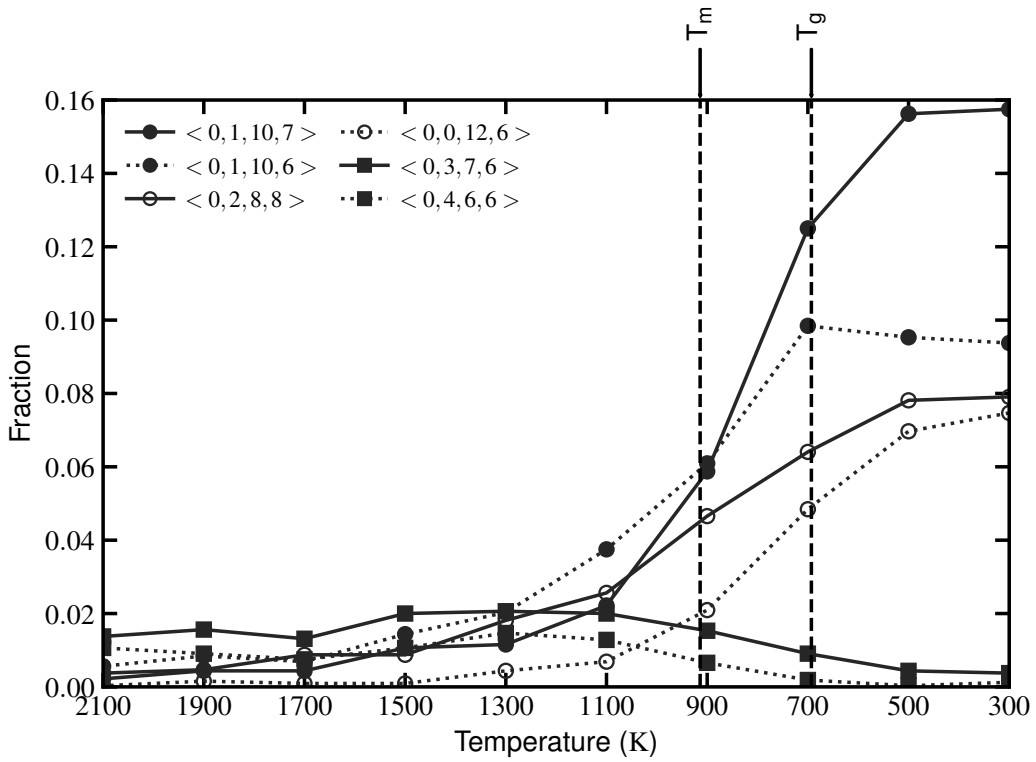

Figure 3.17: The fraction of the six most populous Sm-centered Voronoi indices as a function of temperature for the $Al_{90}Sm_{10}$ model quenched with a cooling rate of $10^{10}\,\mathrm{K\,s^{-1}}$. T_m and T_g annotations show the temperatures at which melting and glass transition temperatures are located, respectively.

Figure 3.17 shows the fraction of the six most populous Voronoi indices around Sm

atoms as a function of temperature. The most populous Sm-centered cells have coordination numbers in the range of 17-19. Almost all Sm-centered cells have higher coordination numbers than Al-centered cells. Also, similarly to Al-centered cells shown in Figure 3.16, distorted icosahedra cells of Sm-atoms show a substantial increase in the fraction in the vicinity of the undercooled region. Among the most frequent six cells, distorted icosahedral $\langle 0, 1, 10, 7\rangle$ cells are dominant in the glassy state with a fraction close to 16%. An interesting observation of Figure 3.17 is the lack of crystal-like or mixed cells. Any considerable amount of crystal-like or mixed cells were, in fact, absent in all simulations. Tanaka [153] suggested that local icosahedral order in metallic glass formers and their liquids prevents the formation of crystalline order and aids the formation of amorphous structure. Our observations can also be attributed to the critical role icosahedral order plays in inhibiting vitrification.

3.3.5.2 Voronoi Connectivity Analysis

Voronoi tessellation analysis only gives topological information about a single atom's nearest neighbor, hence in the SRO scale. However, MRO occurs on longer distances than achievable solely by Voronoi tessellation analysis. The connections of those Voronoi cells can be analyzed to extend the SRO on nearest neighbors to MRO that incorporates neighbors beyond the first neighbor shells [154, 155]. The connectivities of the most populous Al-centered Voronoi cells with each other are analyzed. Only linked cells were considered in this analysis and were defined as linked when cells were first neighbors. In Figures 3.18 and 3.20, the cells that share a common vertex, face, and edge labeled as *Vertex-Shared*, *Face-Shared*, and *Edge-Shared*, respectively. *Interpenetrating* connectivity mode is defined as the cells that have their center atoms bonded to each other. Depending on their connection types, these schemes give in-depth insight into the networks formed within metallic glasses on the MRO scale. Figures 3.18 and 3.19 show the evolution of the connection modes for the Al-centered perfect-ICO $\langle 0, 0, 12, 0\rangle$ cells with respect to temperature. In the liquid state above $1100\,\mathrm{K}$ most of the cells have interpenetrating connections. As the temperature decreases towards the room temperature, the fractions of both vertex- and face-shared cells increase in lieu of interpenetrating and edge-shared cells. As the fraction of loosely packed edge-shared Al-centered $\langle 0, 0, 12, 0\rangle$ cells reduces, the

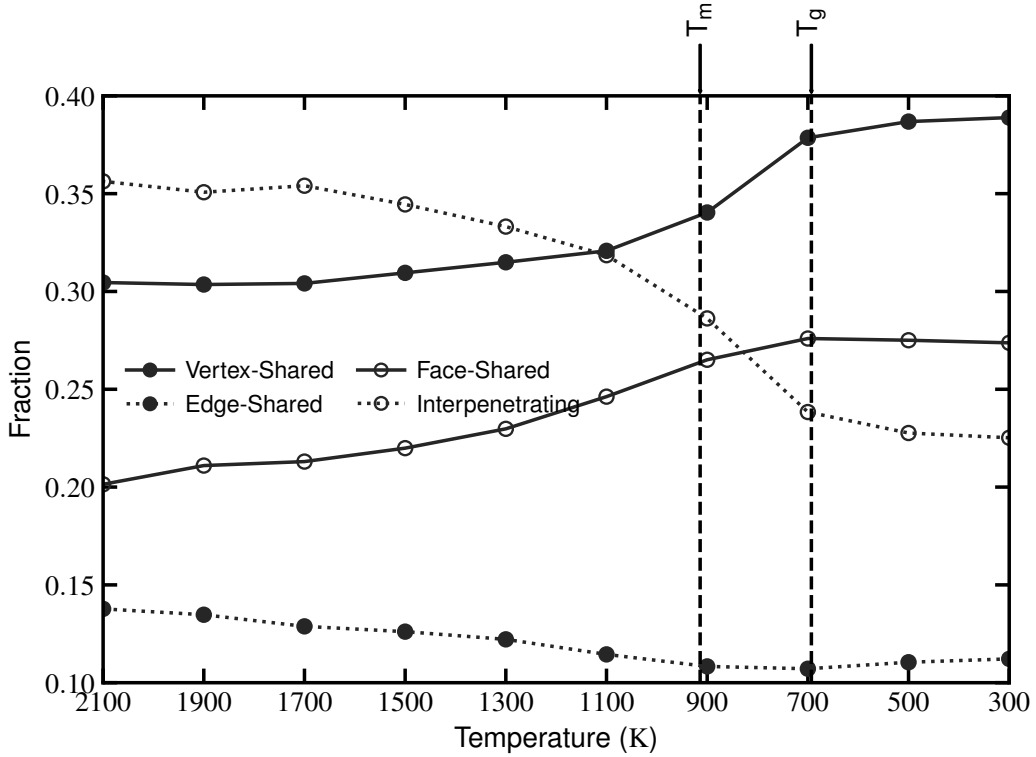

Figure 3.18: The fraction of connectivities of Al-centered $\langle 0, 0, 12, 0 \rangle$ polyhedrons as a function of temperature for the $Al_{90}Sm_{10}$ model quenched with a cooling rate of $10^{10}\,\mathrm{K\,s^{-1}}$. T_m and T_g annotations show the temperatures at which melting and glass transition temperatures are located, respectively.

fraction of stable face-shared Al-centered $\langle 0, 0, 12, 0 \rangle$ increases. This shift from edge-shared connection to face-shared one was previously reported by Ding et al. for Mg – Cu – Y [156] and Cu – Zr [157] systems. Our observation implies that perfect-ICO $\langle 0, 0, 12, 0 \rangle$ polyhedrons tend to distance themselves to create a network on the MRO scale.

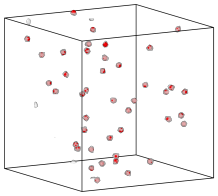

(a) 2100 K

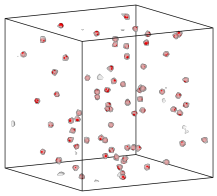

(b) 1900 K

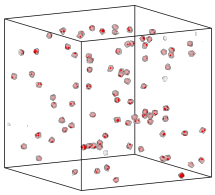

(c) 1700 K

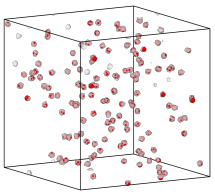

(d) 1500 K

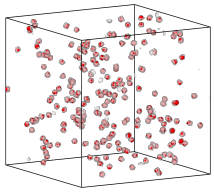

(e) 1300 K

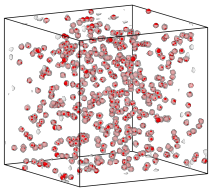

(f) 1100 K

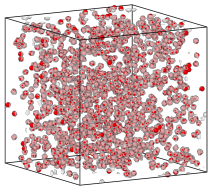

(g) 900 K

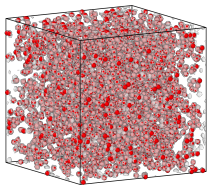

(h) 700 K

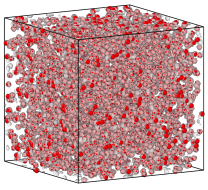

(i) 500 K

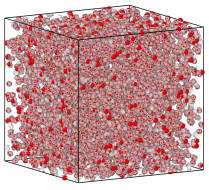

(j) 300 K

Figure 3.19: The evolution of Al-centered $\langle 0, 0, 12, 0 \rangle$ cells with temperature. Only Al-centered $\langle 0, 0, 12, 0 \rangle$ cells and the Voronoi polyhedrons around each were plotted for clarity.

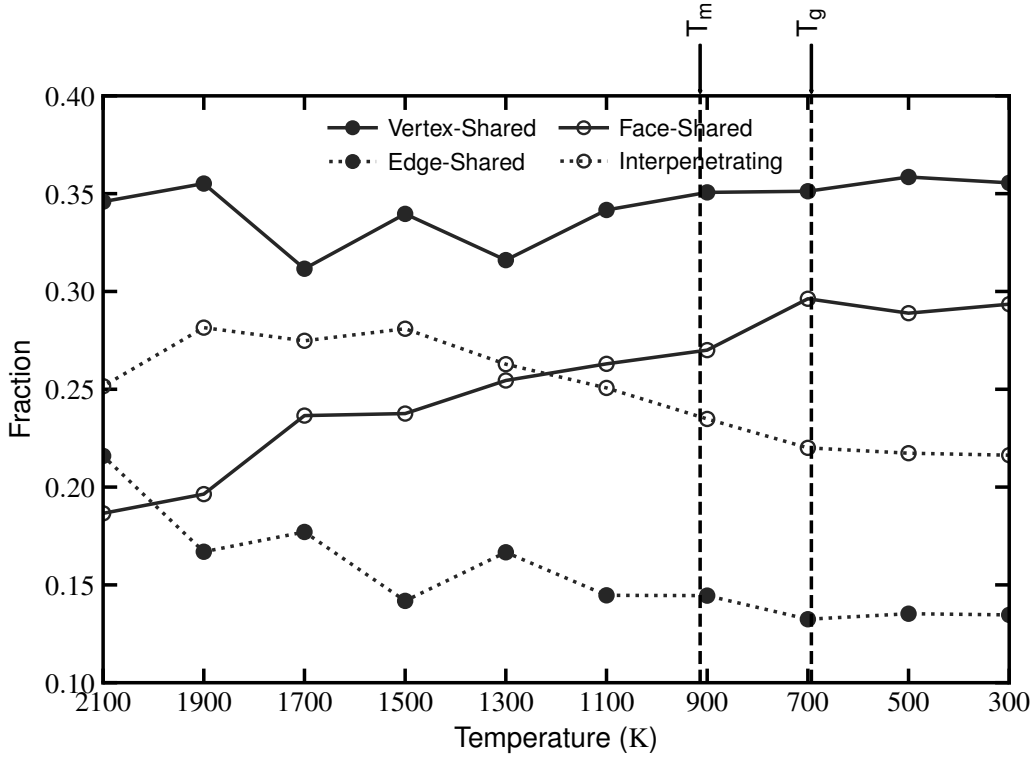

Figure 3.20: The fraction of connectivities of Al-centered $\langle 0, 1, 10, 2\rangle$ polyhedrons as a function of temperature for the $Al_{90}Sm_{10}$ model quenched with a cooling rate of $10^{10}\,\mathrm{K\,s^{-1}}$. T_m and T_g annotations show the temperatures at which melting and glass transition temperatures are located, respectively.

The evolution of the connection modes for the Al-centered distorted-ICO $\langle 0, 1, 10, 2\rangle$ cells with respect to temperature is shown in Figures 3.20 and 3.21. In contrast to perfect-ICO $\langle 0, 0, 12, 0\rangle$ cells, vertex-shared distorted-ICO $\langle 0, 1, 10, 2\rangle$ cells remain relatively stable and dominate the structure throughout the cooling process. Cells connected via their faces show a steady increase from around $20\,\%$ to $30\,\%$. Similar to the connection scheme of perfect-ICO $\langle 0, 0, 12, 0\rangle$ cells, the fraction of interpenetrating distorted-ICO $\langle 0, 1, 10, 2\rangle$ cells declines with the increase in face-shared cells.

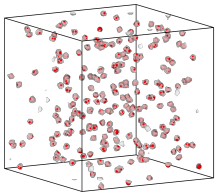

(a) 2100 K

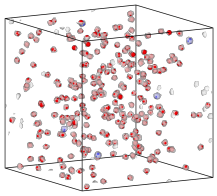

(b) 1900 K

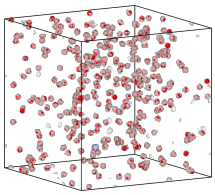

(c) 1700 K

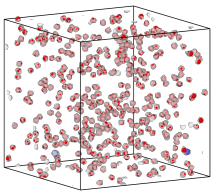

(d) 1500 K

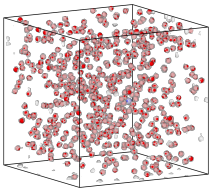

(e) 1300 K

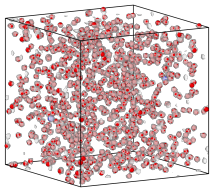

(f) 1100 K

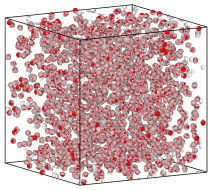

(g) 900 K

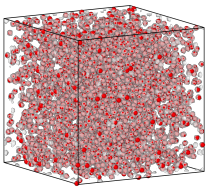

(h) 700 K

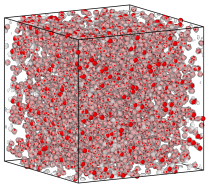

(i) 500 K

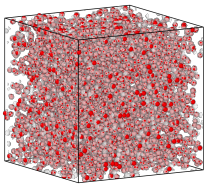

(j) 300 K

Figure 3.21: The evolution of Al-centered $\langle 0, 0, 12, 0 \rangle$ cells with temperature. Only Al-centered $\langle 0, 0, 12, 0 \rangle$ cells and the Voronoi polyhedrons around each were plotted for clarity.

3.3.6 Honeycutt-Andersen Analysis

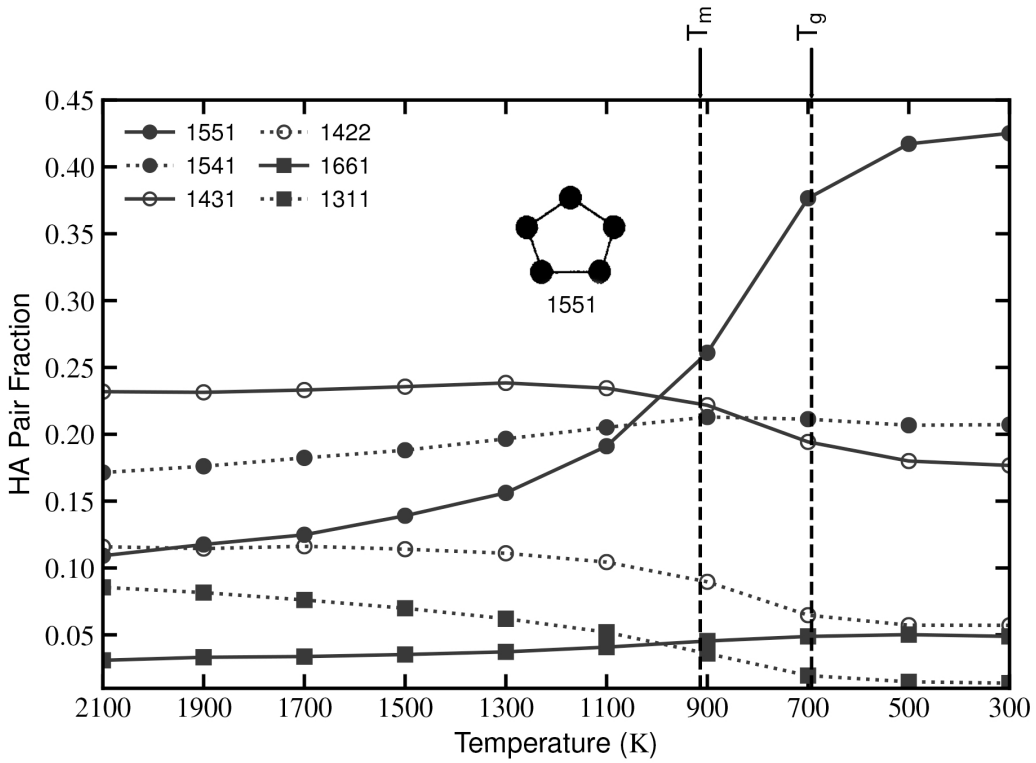

Figure 3.22: The fraction of H-A pair indices as a function of temperature for the $Al_{90}Sm_{10}$ model quenched with a cooling rate of $10^{10}\,\mathrm{K\,s^{-1}}$. T_m and T_g annotations show the temperatures at which melting and glass transition temperatures are located, respectively.

The Honeycutt-Andersen (H-A) method [106] is a widely used pair analysis technique to characterize short-range order through atomic pairs' local environment, especially for amorphous and liquid structures. In this method, four integers, *ijkl*, are used for defining the local environments of atomic pairs within the model. The first integer of the H-A index indicates whether the atomic pair in question are bonded or not; it will be one if the pair is bonded and 2 otherwise. Each atom is considered to be only bonded to its Voronoi neighbors in this study. The second and third indices denote the number of shared nearest neighbors and the number of shared bonds of the pair, respectively. The last index is used to distinguish non-identical pairs when the first three indices are the same. In this context, the H-A index of 1551 represents perfect-

ICO, while 1431 and 1541 represent distorted icosahedra. The *fcc* and *hcp* structures have the H-A indices of 1421 and 1422, respectively. Lastly, indices 1661 and 1441 represent *bcc* structures.

Figure 3.22 illustrates the fraction of the most abundant H-A pair indices, 1551, 1541, 1431, 1422, 1661, and 1311, as a function of temperature. In this figure, T_m and T_g are annotated as vertical dashed lines. The fraction of 1551 type perfect-icosahedron exponentially increases in the liquid state as the temperature decreases and shows a significant increase prior to the undercooled region, between the melting and glass transition temperature., before dominating the model. Distorted icosahedral 1541 and 1431 are the second and third most dominant indices at room temperature. This observation indicates that icosahedral SRO is dominant both in the undercooled liquid and in the glassy model. Having a dominance even in the liquid state supports the hypothesis that icosahedral SRO seen at the room temperature is inherited from the liquid state. Our Honeycutt-Andersen index analysis results are consistent with the Voronoi tessellation analysis discussed before.

3.3.7 Bond Angle Distribution Analysis

Bond angle distribution analysis is used to analyze the spatial arrangements of bonded atoms within the $Al_{90}Sm_{10}$ system from $2100\,\mathrm{K}$ to $300\,\mathrm{K}$ at $200\,\mathrm{K}$ intervals. The atoms are regarded as bonded if they share a common Voronoi face. The probability of Al – Al – Al, Al – Al – Sm, Sm – Al – Sm, Al – Sm – Al, Sm – Sm – Al, and Sm – Sm – Sm triplets forming an angle θ was measured an represented in Figure 3.23. The noisy results in Sm – Sm – Sm triplet is due to low concentration of Sm atoms in $32\,000$ atom $Al_{90}Sm_{10}$ model. Almost all triplets has peaks at $\sim 60°$ and $\sim 120°$ which are very close to the ideal icosahedral bond angles $63.5°$ and $116.5°$. As the temperature decreases, the sharpness of peaks at $\sim 60°$ and $\sim 120°$ increases, which indicates the formation of a more stable icosahedral order within the structure.

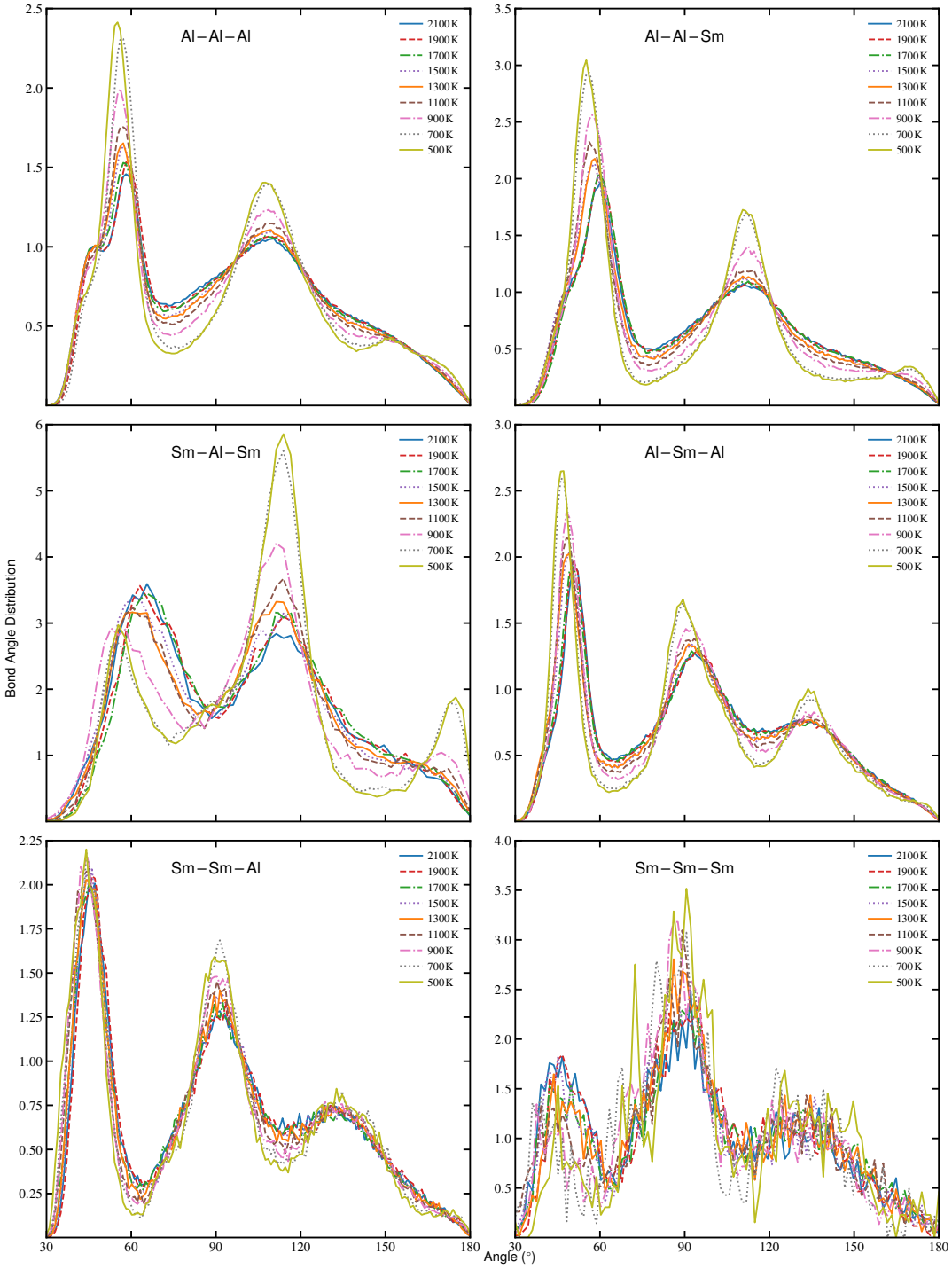

Figure 3.23: Bond angle distribution analysis of $Al_{90}Sm_{10}$ model quenched with a cooling rate of $10^{10}\,\mathrm{K\,s^{-1}}$. Data of each triplet shown from $2100\,\mathrm{K}$ to $300\,\mathrm{K}$ at $200\,\mathrm{K}$ intervals between $30°$ to $180°$.

CHAPTER 4

CONCLUSION AND FUTURE RECOMMENDATIONS

4.1 Conclusions

Having extraordinary structural and functional properties, Al-based MGs are of major interest both in the research community and industry. Combining metals with glasses leads to outstanding possibilities, and for tailoring such properties, atomic-level structure and structure-property relationship should be thoroughly inspected. Al – RE alloys have the unusual glass-forming ability, extremely high nucleation density upon crystallization, and improved structural and mechanical properties, unlike others. However, the origin of their structures that result in such properties is still not well understood. This study investigates the unknown structure of Al – RE alloys, particularly $Al_{90}Sm_{10}$. After obtaining a reliable and comparable model to the experimental observations, several structural analysis techniques are implemented.

The pair distribution function analysis between $2100\,\mathrm{K}$ to $300\,\mathrm{K}$ shows the second peak splitting below T_g. The Sm – Sm partial pair distribution function coincided with the second peak's shoulder, which resulted in the splitting. The observation validated as splitting enhanced with increased Sm – Sm interactions at the corresponding interatomic distance. The pre-peak observed at the low-Q regions in the total structure factors of Al – RE systems is mainly attributed to MRO present in the system. Our study found that the pre-peak of the $Al_{90}Sm_{10}$ system persists even at temperatures above the alloy's melting temperature. This observation supports the hypothesis of the persistent MRO in the melts of Al – RE alloys which hinder the crystallization. Voronoi tessellation analysis was used to identify local symmetry in the $Al_{90}Sm_{10}$ alloy. Upon cooling, the fractions of the perfect icosahedron and distorted icosa-

hedron cells showed a considerable increase in the undercooled region between the melting and the glass transition temperature. The connected clusters of Voronoi cells are in the scale of MRO. Thus, to further extend the knowledge of the local structure of the $Al_{90}Sm_{10}$ system on the MRO scale, the connectivities of the most populous Voronoi cells were analyzed. It is seen that as the temperature decreases, the cells with an interpenetrating connection scheme distance themselves to create a network on the MRO scale. The Honeycutt-Andersen (H-A) pair analysis technique was used to characterize short-range order through each atom's local environment. 1551, 1541, and 1431 type H-A pairs were found to dominate the short-range local structure of liquid and glassy $Al_{90}Sm_{10}$. The observation supports the statement of dominant icosahedral SRO in the liquid state that inherits the SRO in the glassy state. The spatial arrangement of the atoms can not be analyzed using Voronoi tessellation or Honeycutt-Andersen analysis. The bond angle distribution was used to characterize the atoms in triplets. It is shown that the spatial arrangements of the atoms also support the icosahedral SRO hypothesis at every temperature between $2100\,\mathrm{K}$ to $300\,\mathrm{K}$.

4.2 Future Recommendations

In addition to the degree of spatial and structural SRO, the chemical SRO is crucial to understanding structural inhomogeneity and the glass-forming ability. The Warren-Cowley parameter analysis should be done to investigate the local chemical SRO and possibly MRO by extending the Warren-Cowley parameter farther than only the nearest neighbors. Warren-Cowley parameter study conducted by Ovun et al. [109] have used inverse monte Carlo generated interatomic potentials that are inadequate to describe multi-body interactions. A better model should be developed to validate or improve the reported results.

Bond-order parameters can be used for nucleation studies to track down the initial nucleus through the devitrification of metallic glasses. The anomalous nucleation densities of $\mathrm{Al-RE}$ systems can be further analyzed computationally by identifying each nucleus and analyzing the corresponding nucleus sizes with respect to undercooling. The study will give tremendous insights into otherwise obscure events that occur during the devitrification.

As stated in Section 1.1.2, the kinetic slowdown of a melt is crucial in inhibiting crystallization for metallic glasses. The viscosity of melts is often used to describe the kinetic slowdown and the crystal nucleation rate. Experimental viscosity measurements are difficult for many reasons. It is possible to eliminate this difficulty with reliable simulation results. The trajectories obtained through the *ab-initio* MD and classical MD simulations can be used to calculate the melt viscosity by utilizing Green-Kubo (GK) formula or Einstein formulation.

There are few studies on ternary Al−RE−RE systems in the literature; however, Kalay's group has some very interesting experimental results. Apart from the precursors used to obtain metallic glasses, it is reported that the concentrations of the constituting rare-earth elements also alter the devitrification behaviors. The explanation of this exciting observation is still lacking. In-depth simulation studies should be focused on the ternary Al−RE−RE systems to reveal the mysteries in the local structures of those materials. So far, the literature has no interatomic potential that successfully describes these systems. Reliable potentials should be created through the necessary experimental and first-principles studies, and the created potentials should be used in local structure studies.

REFERENCES

[1] W. Klement, R. H. Willens, and P. Duwez, "Non-crystalline Structure in Solidified Gold-Silicon Alloys," *Nature*, vol. 187, no. 4740, pp. 869–870, 1960.

[2] H. L. Luo and P. Duwez, "Metastable amorphous phases in tellurium-base alloys," *Applied Physics Letters*, vol. 2, no. 1, pp. 21–21, 1963.

[3] P. Duwez, R. H. Willens, and R. C. Crewdson, "Amorphous phase in palladium—silicon alloys," *Journal of Applied Physics*, vol. 36, no. 7, pp. 2267–2269, 1965.

[4] H. Chen and D. Turnbull, "Formation, stability and structure of palladium-silicon based alloy glasses," *Acta Metallurgica*, vol. 17, no. 8, pp. 1021–1031, 1969.

[5] H. Chen, "Thermodynamic considerations on the formation and stability of metallic glasses," *Acta Metallurgica*, vol. 22, no. 12, pp. 1505–1511, 1974.

[6] R. Ruhl, B. Giessen, M. Cohen, and N. Grant, "New microcrystalline phases in the nb-ni and ta-ni systems," *Acta Metallurgica*, vol. 15, no. 11, pp. 1693–1702, 1967.

[7] H. S. Chen and D. Turnbull, "Evidence of a glass–liquid transition in a gold–germanium–silicon alloy," *The Journal of Chemical Physics*, vol. 48, no. 6, pp. 2560–2571, 1968.

[8] H. S. Chen and C. E. Miller, "A rapid quenching technique for the preparation of thin uniform films of amorphous solids," *Review of Scientific Instruments*, vol. 41, no. 8, pp. 1237–1238, 1970.

[9] H. Chen and C. Miller, "Centrifugal spinning of metallic glass filaments," *Materials Research Bulletin*, vol. 11, no. 1, pp. 49–54, 1976.

[10] H. Liebermann and C. Graham, "Production of amorphous alloy ribbons and effects of apparatus parameters on ribbon dimensions," *IEEE Transactions on Magnetics*, vol. 12, no. 6, pp. 921–923, 1976.

[11] M. C. Lee, J. M. Kendall, and W. L. Johnson, "Spheres of the metallic glass au55pb22.5sb22.5 and their surface characteristics," *Applied Physics Letters*, vol. 40, no. 5, pp. 382–384, 1982.

[12] A. Inoue, T. Zhang, and T. Masumoto, "Al-la-ni amorphous alloys with a wide supercooled liquid region," *Materials Transactions, JIM*, vol. 30, no. 12, pp. 965–972, 1989.

[13] A. Inoue, H. Yamaguchi, T. Zhang, and T. Masumoto, "Al-la-cu amorphous alloys with a wide supercooled liquid region," *Materials Transactions, JIM*, vol. 31, no. 2, pp. 104–109, 1990.

[14] S. G. Kim, A. Inoue, and T. Masumoto, "High mechanical strengths of mg-ni-y and mg-cu-y amorphous alloys with significant supercooled liquid region," *Materials Transactions, JIM*, vol. 31, no. 11, pp. 929–934, 1990.

[15] A. Inoue, A. Kato, T. Zhang, S. G. Kim, and T. Masumoto, "Mg-cu-y amorphous alloys with high mechanical strengths produced by a metallic mold casting method," *Materials Transactions, JIM*, vol. 32, no. 7, pp. 609–616, 1991.

[16] T. Zhang, A. Inoue, and T. Masumoto, "Amorphous zr-al-tm (tm=co, ni, cu) alloys with significant supercooled liquid region of over 100 k," *Materials Transactions, JIM*, vol. 32, no. 11, pp. 1005–1010, 1991.

[17] A. Peker and W. L. Johnson, "A highly processable metallic glass: $Zr_{41.2}Ti_{13.8}Cu_{12.5}Ni_{10.0}Be_{22.5}$," *Applied Physics Letters*, vol. 63, pp. 2342–2344, oct 1993.

[18] A. Inoue, "High Strength Bulk Amorphous Alloys with Low Critical Cooling Rates (Overview)," *Materials Transactions, JIM*, vol. 36, no. 7, pp. 866–875, 1995.

[19] A. Inoue, "Stabilization of Metallic Supercooled Liquid and Bulk Amorphous Alloys," *Acta Materialia*, vol. 48, no. 1, pp. 279–306, 2000.

[20] M. H. Cohen and D. Turnbull, "Composition requirements for glass formation in metallic and ionic systems," *Nature*, vol. 189, no. 4759, pp. 131–132, 1961.

[21] D. Turnbull, "Under What Conditions Can A Glass Be Formed?," *Contemporary Physics*, vol. 10, pp. 473–488, sep 1969.

[22] J. F. Löffler, "Bulk Metallic Glasses," *Intermetallics*, vol. 11, no. 6, pp. 529–540, 2003.

[23] R. Miller, "Physical properties of liquid metals," *Liquid Metals Handbook*, p. 38, 1952.

[24] C. A. Angell, "Formation of glasses from liquids and biopolymers," *Science*, vol. 267, pp. 1924–1935, mar 1995.

[25] W. T. Laughlin and D. R. Uhlmann, "Viscous flow in simple organic liquids," *The Journal of Physical Chemistry*, vol. 76, no. 16, pp. 2317–2325, 1972.

[26] H. W. Kui, A. L. Greer, and D. Turnbull, "Formation of bulk metallic glass by fluxing," *Applied Physics Letters*, vol. 45, no. 6, pp. 615–616, 1984.

[27] A. J. Drehman, A. L. Greer, and D. Turnbull, "Bulk formation of a metallic glass: Pd40ni40p20," *Applied Physics Letters*, vol. 41, no. 8, pp. 716–717, 1982.

[28] H. Chen, J. Krause, and E. Coleman, "Elastic constants, hardness and their implications to flow properties of metallic glasses," *Journal of Non-Crystalline Solids*, vol. 18, no. 2, pp. 157–171, 1975.

[29] A. Inoue, T. Zhang, N. Nishiyama, K. Ohba, and T. Masumoto, "Preparation of 16 mm diameter rod of amorphous zr65al7.5ni10cu17.5 alloy," *Materials Transactions, JIM*, vol. 34, no. 12, pp. 1234–1237, 1993.

[30] D. Xu, G. Duan, and W. L. Johnson, "Unusual glass-forming ability of bulk amorphous alloys based on ordinary metal copper," *Phys. Rev. Lett.*, vol. 92, p. 245504, Jun 2004.

[31] J. Shen, Q. Chen, J. Sun, H. Fan, and G. Wang, "Exceptionally high glass-forming ability of an fecocrmocby alloy," *Applied Physics Letters*, vol. 86, no. 15, p. 151907, 2005.

[32] H. Men, S. J. Pang, and T. Zhang, "Effect of er doping on glass-forming ability of co50cr15mo14c15b6 alloy," *Journal of Materials Research*, vol. 21, no. 4, pp. 958–961, 2006.

[33] A. Inoue, A. Kitamura, and T. Masumoto, "The Effect of Aluminium on Mechanical Properties and Thermal Stability of (Fe, Co, Ni)-Al-B Ternary Amorphous Alloys," *Journal of Materials Science*, vol. 16, no. 7, pp. 1895–1908, 1981.

[34] R. O. Suzuki, Y. Komatsu, K. F. Kobayashi, and P. H. Shingu, "Formation and crystallization of al-fe-si amorphous alloys," *Journal of Materials Science*, vol. 18, no. 4, pp. 1195–1201, 1983.

[35] Y. He, S. J. Poon, and G. J. Shiflet, "Synthesis and Properties of Metallic Glasses That Contain Aluminum," *Science*, vol. 241, pp. 1640 LP – 1642, sep 1988.

[36] A. Inoue, M. Yamamoto, H. M. Kimura, and T. Masumoto, "Ductile aluminium-base amorphous alloys with two separate phases," *Journal of Materials Science Letters*, vol. 6, no. 2, pp. 194–196, 1987.

[37] A. Inoue, K. Ohtera, A.-P. Tsai, and T. Masumoto, "Aluminum-based amorphous alloys with tensile strength above 980 MPa (100 kg/mm^2)," *Japanese Journal of Applied Physics*, vol. 27, pp. L479–L482, apr 1988.

[38] Y. He, G. Dougherty, G. Shiflet, and S. Poon, "Unique metallic glass formability and ultra-high tensile strength in al-ni-fe-gd alloys," *Acta Metallurgica et Materialia*, vol. 41, no. 2, pp. 337–343, 1993.

[39] A. Inoue, "Amorphous, Nanoquasicrystalline and Nanocrystalline Alloys in Al-Based Systems," *Progress in Materials Science*, vol. 43, no. 5, pp. 365–520, 1998.

[40] A. Inoue, K. Ohtera, and T. Masumoto, "New amorphous al-y, al-la and al-ce alloys prepared by melt spinning," *Japanese Journal of Applied Physics*, vol. 27, pp. L736–L739, may 1988.

[41] A. Inoue, K. Ohtera, Z. Tao, and T. Masumoto, "New amorphous al-ln (ln=pr, nd, sm or gd) alloys prepared by melt spinning," *Japanese Journal of Applied Physics*, vol. 27, pp. L1583–L1586, sep 1988.

[42] A. Inoue, T. Zhang, K. Kita, and T. Masumoto, "Mechanical strengths, thermal stability and electrical resistivity of aluminum-rare earth metal binary amorphous alloys," *Materials Transactions, JIM*, vol. 30, no. 11, pp. 870–877, 1989.

[43] L. Battezzati, M. Baricco, P. Schumacher, W. Shih, and A. Greer, "Crystallization behaviour of al-sm amorphous alloys," *Materials Science and Engineering: A*, vol. 179-180, pp. 600–604, 1994. Proceedings of the Eighth International Conference on Rapidly Quenched and Metastable Materials.

[44] P. Rizzi, C. Antonione, M. Baricco, L. Battezzati, L. Armelao, E. Tondello, M. Fabrizio, and S. Daolio, "Crystals and nanocrystals in rapidly solidified al-sm alloys," *Nanostructured Materials*, vol. 10, no. 5, pp. 767–776, 1998. Selected Papers from the Conference on Microstructure and its Effects on Amorphous, Nanophase and Nanocrystalline Materials TMS Annual Meeting and Exposition.

[45] R. Wu, G. Wilde, and J. H. Perepezko, "Glass formation and primary nanocrystallization in al-base metallic glasses," *Materials Science and Engineering: A*, vol. 301, no. 1, pp. 12–17, 2001.

[46] J. Perepezko, R. Hebert, R. Wu, and G. Wilde, "Primary crystallization in amorphous al-based alloys," *Journal of Non-Crystalline Solids*, vol. 317, no. 1, pp. 52–61, 2003. Advances in Metallic Glasses.

[47] F. Guo, S. Enouf, S. Poon, and G. Shiflet, "Formation of ductile al-based metallic glasses without rare-earth elements," *Philosophical Magazine Letters*, vol. 81, no. 3, pp. 203–211, 2001.

[48] R. L. McGreevy and L. Pusztai, "Reverse monte carlo simulation: A new technique for the determination of disordered structures," *Molecular Simulation*, vol. 1, no. 6, pp. 359–367, 1988.

[49] D. A. Keen and R. L. McGreevy, "Structural modelling of glasses using reverse monte carlo simulation," *Nature*, vol. 344, no. 6265, pp. 423–425, 1990.

[50] R. L. McGreevy, "Reverse monte carlo modelling," *Journal of Physics: Condensed Matter*, vol. 13, pp. R877–R913, nov 2001.

[51] O. Gereben, P. Jóvári, Temleitner, and L. L., Pusztai, "A new version of the rmc++ reverse monte carlo programme, aimed at investigating the structure of covalent glasses," *J. Optoelectron. Adv. Mater.*, vol. 9, no. 10, pp. 3021–3027, 2007.

[52] M. G. Tucker, D. A. Keen, M. T. Dove, A. L. Goodwin, and Q. Hui, "RMCProfile: reverse monte carlo for polycrystalline materials," *Journal of Physics: Condensed Matter*, vol. 19, p. 335218, jul 2007.

[53] B. Aoun, "Fullrmc, a rigid body reverse monte carlo modeling package enabled with machine learning and artificial intelligence," *Journal of Computational Chemistry*, vol. 37, no. 12, pp. 1102–1111, 2016.

[54] B. J. Alder and T. E. Wainwright, "Studies in molecular dynamics. i. general method," *The Journal of Chemical Physics*, vol. 31, no. 2, pp. 459–466, 1959.

[55] B. J. Alder and T. E. Wainwright, "Phase transition for a hard sphere system," *The Journal of Chemical Physics*, vol. 27, no. 5, pp. 1208–1209, 1957.

[56] J. E. Jones, "On the determination of molecular fields.—i. from the variation of the viscosity of a gas with temperature," *Proceedings of the Royal Society of London. Series A, Containing Papers of a Mathematical and Physical Character*, vol. 106, pp. 441–462, Oct. 1924.

[57] J. E. Jones, "On the determination of molecular fields. —II. from the equation of state of a gas," *Proceedings of the Royal Society of London. Series A, Containing Papers of a Mathematical and Physical Character*, vol. 106, pp. 463–477, Oct. 1924.

[58] J. E. Lennard-Jones, "Cohesion," *Proceedings of the Physical Society*, vol. 43, pp. 461–482, sep 1931.

[59] R. LeSar, *Introduction to computational materials science*. Cambridge, England: Cambridge University Press, Mar. 2013.

[60] M. S. Daw and M. I. Baskes, "Embedded-atom method: Derivation and application to impurities, surfaces, and other defects in metals," *Phys. Rev. B*, vol. 29, pp. 6443–6453, Jun 1984.

[61] M. S. Daw, S. M. Foiles, and M. I. Baskes, "The embedded-atom method: a review of theory and applications," *Materials Science Reports*, vol. 9, no. 7-8, pp. 251–310, 1993.

[62] G. Mie, "Zur kinetischen theorie der einatomigen körper," *Annalen der Physik*, vol. 316, no. 8, pp. 657–697, 1903.

[63] F. Fumi and M. Tosi, "Ionic sizes and born repulsive parameters in the nacl-type alkali halides—i: The huggins-mayer and pauling forms," *Journal of Physics and Chemistry of Solids*, vol. 25, no. 1, pp. 31–43, 1964.

[64] M. Tosi and F. Fumi, "Ionic sizes and born repulsive parameters in the nacl-type alkali halides—ii: The generalized huggins-mayer form," *Journal of Physics and Chemistry of Solids*, vol. 25, no. 1, pp. 45–52, 1964.

[65] R. A. Buckingham, "The classical equation of state of gaseous helium, neon and argon," *Proceedings of the Royal Society of London. Series A. Mathematical and Physical Sciences*, vol. 168, pp. 264–283, Oct. 1938.

[66] F. H. Stillinger and T. A. Weber, "Computer simulation of local order in condensed phases of silicon," *Phys. Rev. B*, vol. 31, pp. 5262–5271, Apr 1985.

[67] J. Tersoff, "New empirical approach for the structure and energy of covalent systems," *Phys. Rev. B*, vol. 37, pp. 6991–7000, Apr 1988.

[68] A. C. T. van Duin, S. Dasgupta, F. Lorant, and W. A. Goddard, "Reaxff: A reactive force field for hydrocarbons," *The Journal of Physical Chemistry A*, vol. 105, no. 41, pp. 9396–9409, 2001.

[69] D. W. Brenner, O. A. Shenderova, J. A. Harrison, S. J. Stuart, B. Ni, and S. B. Sinnott, "A second-generation reactive empirical bond order (REBO) potential energy expression for hydrocarbons," *Journal of Physics: Condensed Matter*, vol. 14, pp. 783–802, jan 2002.

[70] L. Verlet, “Computer "experiments" on classical fluids. i. thermodynamical properties of lennard-jones molecules,” *Phys. Rev.*, vol. 159, pp. 98–103, Jul 1967.

[71] E. T. Whittaker, *A treatise on the analytical dynamics of particles and rigid bodies*. CUP Archive, 1937.

[72] G. Dahlquist and etc., *Numerical Methods*. Prentice-Hall series in automatic computation, Harlow, England: Prentice Hall PTR, Dec. 1974.

[73] W. C. Swope, H. C. Andersen, P. H. Berens, and K. R. Wilson, “A computer simulation method for the calculation of equilibrium constants for the formation of physical clusters of molecules: Application to small water clusters,” *The Journal of Chemical Physics*, vol. 76, no. 1, pp. 637–649, 1982.

[74] L. Verlet, “Computer "experiments" on classical fluids. ii. equilibrium correlation functions,” *Phys. Rev.*, vol. 165, pp. 201–214, Jan 1968.

[75] R. Hockney and J. Eastwood, *Computer Simulation Using Particles*. CRC Press, Mar. 2021.

[76] D. Beeman, “Some multistep methods for use in molecular dynamics calculations,” *Journal of Computational Physics*, vol. 20, no. 2, pp. 130–139, 1976.

[77] A. Rahman, “Correlations in the motion of atoms in liquid argon,” *Phys. Rev.*, vol. 136, pp. A405–A411, Oct 1964.

[78] B. R. Brooks, C. L. Brooks III, A. D. Mackerell Jr, L. Nilsson, R. J. Petrella, B. Roux, Y. Won, G. Archontis, C. Bartels, S. Boresch, *et al.*, “Charmm: the biomolecular simulation program,” *Journal of computational chemistry*, vol. 30, no. 10, pp. 1545–1614, 2009.

[79] I. T. Todorov, W. Smith, K. Trachenko, and M. T. Dove, “Dl_poly_3: new dimensions in molecular dynamics simulations via massive parallelism,” *J. Mater. Chem.*, vol. 16, pp. 1911–1918, 2006.

[80] P. Bauer, B. Hess, and E. Lindahl, “Gromacs 2022.2 source code,” June 2022.

[81] J. A. Anderson, J. Glaser, and S. C. Glotzer, "Hoomd-blue: A python package for high-performance molecular dynamics and hard particle monte carlo simulations," *Computational Materials Science*, vol. 173, p. 109363, 2020.

[82] S. Plimpton, "Fast parallel algorithms for short-range molecular dynamics," *Journal of Computational Physics*, vol. 117, no. 1, pp. 1 – 19, 1995.

[83] A. P. Thompson, H. M. Aktulga, R. Berger, D. S. Bolintineanu, W. M. Brown, P. S. Crozier, P. J. in 't Veld, A. Kohlmeyer, S. G. Moore, T. D. Nguyen, R. Shan, M. J. Stevens, J. Tranchida, C. Trott, and S. J. Plimpton, "LAMMPS - a flexible simulation tool for particle-based materials modeling at the atomic, meso, and continuum scales," *Comp. Phys. Comm.*, vol. 271, p. 108171, 2022.

[84] A. H. Romero, D. C. Allan, B. Amadon, G. Antonius, T. Applencourt, L. Baguet, J. Bieder, F. Bottin, J. Bouchet, E. Bousquet, F. Bruneval, G. Brunin, D. Caliste, M. Côté, J. Denier, C. Dreyer, P. Ghosez, M. Giantomassi, Y. Gillet, O. Gingras, D. R. Hamann, G. Hautier, F. Jollet, G. Jomard, A. Martin, H. P. C. Miranda, F. Naccarato, G. Petretto, N. A. Pike, V. Planes, S. Prokhorenko, T. Rangel, F. Ricci, G.-M. Rignanese, M. Royo, M. Stengel, M. Torrent, M. J. van Setten, B. V. Troeye, M. J. Verstraete, J. Wiktor, J. W. Zwanziger, and X. Gonze, "Abinit: Overview, and focus on selected capabilities," *J. Chem. Phys.*, vol. 152, p. 124102, 2020.

[85] X. Gonze, B. Amadon, G. Antonius, F. Arnardi, L. Baguet, J.-M. Beuken, J. Bieder, F. Bottin, J. Bouchet, E. Bousquet, N. Brouwer, F. Bruneval, G. Brunin, T. Cavignac, J.-B. Charraud, W. Chen, M. Côté, S. Cottenier, J. Denier, G. Geneste, P. Ghosez, M. Giantomassi, Y. Gillet, O. Gingras, D. R. Hamann, G. Hautier, X. He, N. Helbig, N. Holzwarth, Y. Jia, F. Jollet, W. Lafargue-Dit-Hauret, K. Lejaeghere, M. A. L. Marques, A. Martin, C. Martins, H. P. C. Miranda, F. Naccarato, K. Persson, G. Petretto, V. Planes, Y. Pouillon, S. Prokhorenko, F. Ricci, G.-M. Rignanese, A. H. Romero, M. M. Schmitt, M. Torrent, M. J. van Setten, B. V. Troeye, M. J. Verstraete, G. Zérah, and J. W. Zwanziger, "The abinit project: Impact, environment and recent developments," *Comput. Phys. Commun.*, vol. 248, p. 107042, 2020.

[86] S. J. Clark, M. D. Segall, C. J. Pickard, P. J. Hasnip, M. I. J. Probert, K. Ref-

son, and M. C. Payne, "First principles methods using castep," *Zeitschrift für Kristallographie - Crystalline Materials*, vol. 220, no. 5-6, pp. 567–570, 2005.

[87] T. D. Kühne, M. Iannuzzi, M. Del Ben, V. V. Rybkin, P. Seewald, F. Stein, T. Laino, R. Z. Khaliullin, O. Schütt, F. Schiffmann, D. Golze, J. Wilhelm, S. Chulkov, M. H. Bani-Hashemian, V. Weber, U. Borštnik, M. Taillefumier, A. S. Jakobovits, A. Lazzaro, H. Pabst, T. Müller, R. Schade, M. Guidon, S. Andermatt, N. Holmberg, G. K. Schenter, A. Hehn, A. Bussy, F. Belleflamme, G. Tabacchi, A. Glöß, M. Lass, I. Bethune, C. J. Mundy, C. Plessl, M. Watkins, J. VandeVondele, M. Krack, and J. Hutter, "Cp2k: An electronic structure and molecular dynamics software package - quickstep: Efficient and accurate electronic structure calculations," *The Journal of Chemical Physics*, vol. 152, no. 19, p. 194103, 2020.

[88] J. M. Soler, E. Artacho, J. D. Gale, A. García, J. Junquera, P. Ordejón, and D. Sánchez-Portal, "The siesta method for ab initio order-n materials simulation," *Journal of Physics: Condensed Matter*, vol. 14, pp. 2745–2779, mar 2002.

[89] P. Giannozzi, O. Andreussi, T. Brumme, O. Bunau, M. B. Nardelli, M. Calandra, R. Car, C. Cavazzoni, D. Ceresoli, M. Cococcioni, N. Colonna, I. Carnimeo, A. D. Corso, S. de Gironcoli, P. Delugas, R. A. DiStasio, A. Ferretti, A. Floris, G. Fratesi, G. Fugallo, R. Gebauer, U. Gerstmann, F. Giustino, T. Gorni, J. Jia, M. Kawamura, H.-Y. Ko, A. Kokalj, E. Küçükbenli, M. Lazzeri, M. Marsili, N. Marzari, F. Mauri, N. L. Nguyen, H.-V. Nguyen, A. O. de-la Roza, L. Paulatto, S. Poncé, D. Rocca, R. Sabatini, B. Santra, M. Schlipf, A. P. Seitsonen, A. Smogunov, I. Timrov, T. Thonhauser, P. Umari, N. Vast, X. Wu, and S. Baroni, "Advanced capabilities for materials modelling with quantum ESPRESSO," *Journal of Physics: Condensed Matter*, vol. 29, p. 465901, oct 2017.

[90] P. Giannozzi, S. Baroni, N. Bonini, M. Calandra, R. Car, C. Cavazzoni, D. Ceresoli, G. L. Chiarotti, M. Cococcioni, I. Dabo, A. D. Corso, S. de Gironcoli, S. Fabris, G. Fratesi, R. Gebauer, U. Gerstmann, C. Gougoussis, A. Kokalj, M. Lazzeri, L. Martin-Samos, N. Marzari, F. Mauri, R. Mazzarello,

S. Paolini, A. Pasquarello, L. Paulatto, C. Sbraccia, S. Scandolo, G. Sclauzero, A. P. Seitsonen, A. Smogunov, P. Umari, and R. M. Wentzcovitch, "QUANTUM ESPRESSO: a modular and open-source software project for quantum simulations of materials," *Journal of Physics: Condensed Matter*, vol. 21, p. 395502, sep 2009.

[91] G. Kresse and J. Hafner, "Ab initio molecular dynamics for liquid metals," *Phys. Rev. B*, vol. 47, pp. 558–561, Jan 1993.

[92] G. Kresse and J. Furthmüller, "Efficiency of ab-initio total energy calculations for metals and semiconductors using a plane-wave basis set," *Computational Materials Science*, vol. 6, no. 1, pp. 15–50, 1996.

[93] G. Kresse and J. Furthmüller, "Efficient iterative schemes for ab initio total-energy calculations using a plane-wave basis set," *Phys. Rev. B*, vol. 54, pp. 11169–11186, Oct 1996.

[94] S. Le Roux and V. Petkov, "*ISAACS* – interactive structure analysis of amorphous and crystalline systems," *Journal of Applied Crystallography*, vol. 43, pp. 181–185, Feb 2010.

[95] T. E. Faber and J. M. Ziman, "A theory of the electrical properties of liquid metals," *The Philosophical Magazine: A Journal of Theoretical Experimental and Applied Physics*, vol. 11, no. 109, pp. 153–173, 1965.

[96] Y. Kalay, L. Chumbley, M. Kramer, and I. Anderson, "Local structure in marginal glass forming al–sm alloy," *Intermetallics*, vol. 18, no. 8, pp. 1676–1682, 2010.

[97] I. Kalay, M. J. Kramer, and R. E. Napolitano, "High-accuracy x-ray diffraction analysis of phase evolution sequence during devitrification of cu50zr50 metallic glass," *Metallurgical and Materials Transactions A*, vol. 42, no. 5, pp. 1144–1153, 2011.

[98] Y. Kalay, C. Yeager, L. Chumbley, M. Kramer, and I. Anderson, "Initial crystallization in a nanostructured al–sm rare earth alloy," *Journal of Non-Crystalline Solids*, vol. 356, no. 28, pp. 1416–1424, 2010.

[99] N. E. R. Zimmermann, M. K. Horton, A. Jain, and M. Haranczyk, "Assessing local structure motifs using order parameters for motif recognition, interstitial identification, and diffusion path characterization," *Frontiers in Materials*, vol. 4, 2017.

[100] G. Voronoi, "Nouvelles applications des paramètres continus à la théorie des formes quadratiques. deuxième mémoire. recherches sur les parallélloèdres primitifs.," *Journal für die reine und angewandte Mathematik*, vol. 1908, no. 134, pp. 198 – 287, 01 Jan. 1908.

[101] J. L. Finney, "Random packings and the structure of simple liquids. i. the geometry of random close packing," *Proceedings of the Royal Society of London. A. Mathematical and Physical Sciences*, vol. 319, pp. 479–493, Nov. 1970.

[102] W. Fischer and E. Koch, "Geometrical packing analysis of molecular compounds," *Zeitschrift für Kristallographie - Crystalline Materials*, vol. 150, no. 1-4, pp. 245–260, 1979.

[103] J. Park and Y. Shibutani, "Effects of atomic size for voronoi tessellation technique on binary and ternary systems of metallic glasses," *MATERIALS TRANSACTIONS*, vol. 47, no. 12, pp. 2904–2909, 2006.

[104] J. Hwang, Z. H. Melgarejo, Y. E. Kalay, I. Kalay, M. J. Kramer, D. S. Stone, and P. M. Voyles, "Nanoscale structure and structural relaxation in $\mathrm{zr}_{50}\mathrm{cu}_{45}\mathrm{al}_5$ bulk metallic glass," *Phys. Rev. Lett.*, vol. 108, p. 195505, May 2012.

[105] Q. Zhang, J. Li, X. Hu, S. Tang, Z. Wang, and J. Wang, "Connections between structural characteristics and crystal nucleation of al–sm glasses near glass transition temperature," *Journal of Non-Crystalline Solids*, vol. 588, p. 121637, 2022.

[106] J. D. Honeycutt and H. C. Andersen, "Molecular dynamics study of melting and freezing of small lennard-jones clusters," *The Journal of Physical Chemistry*, vol. 91, no. 19, pp. 4950–4963, 1987.

[107] B. Warren, *X-ray Diffraction*. Addison-Wesley series in metallurgy and materials engineering, Dover Publications, 1990.

[108] J. M. Cowley, "X-Ray Measurement of Order in Single Crystals of Cu_3Au," *Journal of Applied Physics*, vol. 21, no. 1, pp. 24–30, 1950.

[109] M. Ovun, M. Kramer, and Y. Kalay, "Structural modeling of liquid and amorphous al91tb9 by monte carlo simulations," *Journal of Non-Crystalline Solids*, vol. 405, pp. 27–32, 2014.

[110] Hafner, J., "Bond-angle distribution functions in metallic glasses," *J. Phys. Colloques*, vol. 46, pp. C9–69–C9–78, 1985.

[111] P. J. Steinhardt, D. R. Nelson, and M. Ronchetti, "Bond-orientational order in liquids and glasses," *Phys. Rev. B*, vol. 28, pp. 784–805, Jul 1983.

[112] P. J. Steinhardt, D. R. Nelson, and M. Ronchetti, "Icosahedral bond orientational order in supercooled liquids," *Phys. Rev. Lett.*, vol. 47, pp. 1297–1300, Nov 1981.

[113] W. Lechner and C. Dellago, "Accurate determination of crystal structures based on averaged local bond order parameters," *The Journal of Chemical Physics*, vol. 129, no. 11, p. 114707, 2008.

[114] P. Chaudhari and D. Turnbull, "Structure and Properties of Metallic Glasses," *Science*, vol. 199, no. 4324, pp. 11–21, 1978.

[115] H. S. Chen, "Glassy Metals," *Reports on Progress in Physics*, vol. 43, no. 4, pp. 353–432, 1980.

[116] A. L. Greer, "Metallic Glasses," *Science*, vol. 267, pp. 1947–1953, mar 1995.

[117] A. L. Greer and E. Ma, "Bulk Metallic Glasses: At the Cutting Edge of Metals Research," *MRS Bulletin*, vol. 32, no. 8, pp. 611–619, 2007.

[118] A. L. Greer, "Metallic Glasses...On The Threshold," *Materials Today*, vol. 12, no. 1-2, pp. 14–22, 2009.

[119] A. Inoue and A. Takeuchi, "Recent Progress in Bulk Glassy Alloys," *Materials Transactions*, vol. 43, no. 8, pp. 1892–1906, 2002.

[120] W. L. Johnson, "Bulk Glass-forming Metallic Alloys: Science and Technology," *MRS Bulletin*, vol. 24, no. 10, pp. 42–56, 1999.

[121] W. L. Johnson, "Bulk Amorphous Metal-An Emerging Engineering Material," *Jom*, vol. 54, no. 3, pp. 40–43, 2002.

[122] W. H. Wang, C. Dong, and C. H. Shek, "Bulk Metallic Glasses," *Materials Science and Engineering R: Reports*, vol. 44, no. 2-3, pp. 45–89, 2004.

[123] Y. Q. Cheng and E. Ma, "Atomic-Level Structure and Structure-Property Relationship in Metallic Glasses," *Progress in Materials Science*, vol. 56, no. 4, pp. 379–473, 2011.

[124] A. Inoue, K. Ohtera, A.-P. Tsai, and T. Masumoto, "New Amorphous Alloys with Good Ductility in Al-Y-M and Al-La-M (M = Fe, Co, Ni or Cu) Systems," *Japanese Journal of Applied Physics*, vol. 27, no. Part 2, No. 3, pp. L280–L282, 1988.

[125] T. Demirtaş and Y. Kalay, "Kinetics of fcc-al nanocrystallization in al90tb10 metallic glass," *Journal of Non-Crystalline Solids*, vol. 378, pp. 71–78, 2013.

[126] Y. Kalay, L. Chumbley, and I. Anderson, "Characterization of a marginal glass former alloy solidified in gas atomized powders," *Materials Science and Engineering: A*, vol. 490, no. 1, pp. 72–80, 2008.

[127] Y. Kalay, I. Kalay, J. Hwang, P. Voyles, and M. Kramer, "Local chemical and topological order in al–tb and its role in controlling nanocrystal formation," *Acta Materialia*, vol. 60, no. 3, pp. 994–1003, 2012.

[128] Y. Kalay, L. Chumbley, and I. Anderson, "Crystallization behavior in a highly driven marginal glass forming alloy," *Journal of Non-Crystalline Solids*, vol. 354, no. 26, pp. 3040–3048, 2008.

[129] N. Wang, Y. Kalay, and R. Trivedi, "Eutectic-to-metallic glass transition in the al–sm system," *Acta Materialia*, vol. 59, no. 17, pp. 6604–6619, 2011.

[130] C. Yildirim, M. Kutsal, R. Ott, M. Besser, M. Kramer, and Y. Kalay, "The role of amorphous precursor in phase selection hierarchy in marginal metallic glasses," *Materials & Design*, vol. 112, pp. 479–484, 2016.

[131] T. H. Ulucan, I. Kalay, and Y. E. Kalay, "The anomalous nucleation in al-tb

metallic glasses," *Metallurgical and Materials Transactions A*, vol. 52, no. 2, pp. 700–710, 2021.

[132] H. Y. Hsieh, T. Egami, Y. He, S. J. Poon, and G. J. Shiflet, "Short Range Ordering in Amorphous $Al_{90}Fe_xCe_{10-x}$," *Journal of Non-Crystalline Solids*, vol. 135, no. 2-3, pp. 248–254, 1991.

[133] E. Erdal, "The effects of chemical short-range order on crystallization pathway in ternary marginal glass forming alloys," Master's thesis, Middle East Technical University, 2021.

[134] A. P. Thompson, S. J. Plimpton, and W. Mattson, "General formulation of pressure and stress tensor for arbitrary many-body interaction potentials under periodic boundary conditions," *The Journal of Chemical Physics*, vol. 131, no. 15, p. 154107, 2009.

[135] M. I. Mendelev, F. Zhang, Z. Ye, Y. Sun, M. C. Nguyen, S. R. Wilson, C. Z. Wang, and K. M. Ho, "Development of interatomic potentials appropriate for simulation of devitrification of $Al_{90}Sm_{10}$ alloy," *Modelling and Simulation in Materials Science and Engineering*, vol. 23, p. 045013, apr 2015.

[136] J. R. de Laeter, J. K. Böhlke, P. D. Bièvre, H. Hidaka, H. S. Peiser, K. J. R. Rosman, and P. D. P. Taylor, "Atomic weights of the elements. review 2000 (iupac technical report)," *Pure and Applied Chemistry*, vol. 75, no. 6, pp. 683–800, 2003.

[137] S. Nosé, "A unified formulation of the constant temperature molecular dynamics methods," *The Journal of Chemical Physics*, vol. 81, no. 1, pp. 511–519, 1984.

[138] W. G. Hoover, "Canonical dynamics: Equilibrium phase-space distributions," *Phys. Rev. A*, vol. 31, pp. 1695–1697, Mar 1985.

[139] E. Prince, ed., *International Tables for Crystallography*. International Union of Crystallography, Oct. 2006.

[140] C. H. Rycroft, "Voro++: A three-dimensional voronoi cell library in c++," *Chaos: An Interdisciplinary Journal of Nonlinear Science*, vol. 19, no. 4, p. 041111, 2009.

[141] J. M. Haile, *Molecular dynamics simulation: elementary methods*. John Wiley & Sons, Inc., 1992.

[142] S. P. Pan, J. Y. Qin, W. M. Wang, and T. K. Gu, "Origin of splitting of the second peak in the pair-distribution function for metallic glasses," *Phys. Rev. B*, vol. 84, p. 092201, Sep 2011.

[143] K. Zhang, H. Li, L. Li, and X. F. Bian, "Why does the second peak of pair correlation functions split in quasi-two-dimensional disordered films?," *Applied Physics Letters*, vol. 102, no. 7, p. 071907, 2013.

[144] Y.-C. Liang, R.-S. Liu, Y.-F. Mo, H.-R. Liu, Z.-A. Tian, Q. yi Zhou, H.-T. Zhang, L.-L. Zhou, Z.-Y. Hou, and P. Peng, "Influence of icosahedral order on the second peak splitting of pair distribution function for mg70zn30 metallic glass," *Journal of Alloys and Compounds*, vol. 597, pp. 269–274, 2014.

[145] H. Tanaka, "Bond orientational order in liquids: Towards a unified description of water-like anomalies, liquid-liquid transition, glass transition, and crystallization," *The European Physical Journal E*, vol. 35, no. 10, p. 113, 2012.

[146] S. Y. Wang, C. Z. Wang, M. Z. Li, L. Huang, R. T. Ott, M. J. Kramer, D. J. Sordelet, and K. M. Ho, "Short- and medium-range order in a $zr_{73}pt_{27}$ glass: Experimental and simulation studies," *Phys. Rev. B*, vol. 78, p. 184204, Nov 2008.

[147] S. R. Elliott, "Medium-range structural order in covalent amorphous solids," *Nature*, vol. 354, no. 6353, pp. 445–452, 1991.

[148] Q. Jingyu, B. Xiufang, S. I. Sliusarenko, and W. Weimin, "Pre-peak in the structure factor of liquid al-fe alloy," *Journal of Physics: Condensed Matter*, vol. 10, pp. 1211–1218, feb 1998.

[149] M. Maret, T. Pomme, A. Pasturel, and P. Chieux, "Structure of liquid $\mathrm{al_{80}ni_{20}}$ alloy," *Phys. Rev. B*, vol. 42, pp. 1598–1604, Jul 1990.

[150] M. Sakata, N. Cowlam, and H. A. Davies, "Neutron diffraction measurement of the structure factor of a CuTi metallic glass," *Journal of Physics F: Metal Physics*, vol. 9, pp. L235–L240, dec 1979.

[151] G. Bokas, L. Zhao, J. Perepezko, and I. Szlufarska, "On the role of sm in solidification of al-sm metallic glasses," *Scripta Materialia*, vol. 124, pp. 99–102, 2016.

[152] S. Mishra and S. Pal, "Variation of glass transition temperature of al90sm10 metallic glass under pressurized cooling," *Journal of Non-Crystalline Solids*, vol. 500, pp. 249–259, 2018.

[153] H. Tanaka, "Roles of local icosahedral chemical ordering in glass and quasicrystal formation in metallic glass formers," *Journal of Physics: Condensed Matter*, vol. 15, pp. L491–L498, jul 2003.

[154] D. B. Miracle, "A structural model for metallic glasses," *Nature Materials*, vol. 3, no. 10, pp. 697–702, 2004.

[155] H. W. Sheng, W. K. Luo, F. M. Alamgir, J. M. Bai, and E. Ma, "Atomic packing and short-to-medium-range order in metallic glasses," *Nature*, vol. 439, no. 7075, pp. 419–425, 2006.

[156] J. Ding, Y. Cheng, and E. Ma, "Charge-transfer-enhanced prism-type local order in amorphous mg65cu25y10: Short-to-medium-range structural evolution underlying liquid fragility and heat capacity," *Acta Materialia*, vol. 61, no. 8, pp. 3130–3140, 2013.

[157] J. Ding, Y.-Q. Cheng, and E. Ma, "Full icosahedra dominate local order in cu64zr34 metallic glass and supercooled liquid," *Acta Materialia*, vol. 69, pp. 343–354, 2014.